

On the Possibilities and Constraints of Reduction of Methane and  
Formaldehyde Slip from the Exhaust of Lean-Burn Natural Gas  
Engines

zur Erlangung des akademischen Grades einer  
DOKTORIN DER INGENIEURWISSENSCHAFTEN (DR.-ING.)

Von der KIT-Fakultät für Chemieingenieurwesen und Verfahrenstechnik des  
Karlsruher Instituts für Technologie (KIT)

genehmigte

DISSERTATION

von

Dipl.-Ing. Bentolhoda Torkashvand

aus

Teheran, Iran

Tag der mündlichen Prüfung: 07.05.2019

Erstgutachter: Prof. Dr. Olaf Deutschmann

Zweitgutachter: Prof. Dr. Achim Dittler



## Abstract

Providing high thermal efficiency, a low CO<sub>2</sub> emission to power ratio, and a low emission level of pollutants such as NO<sub>x</sub> and particulate matter, lean-burn natural gas (NG) engines become a promising type of engine to meet stringent emission regulations. Despite these advantages, the exhaust gas emitted from natural gas engines contains a significant amount of unburnt methane, which is of particular environmental concerns, as methane is a more potent greenhouse gas than CO<sub>2</sub>. Furthermore, formaldehyde is formed as an intermediate species in the oxidation of methane and is thus present in the exhaust gas of lean-burn operating NG engines. Formaldehyde is known for its carcinogenic properties to the human body and has therefore been classified as hazardous air pollutant, which has led to increasingly strict regulations. As the utilization of lean-burn NG engines in the energy sector experiences increasing popularity, appropriate measures for the reduction of methane as well as formaldehyde emission from lean-burn NG engines need to be taken. The present thesis intends to picture constraints but also improvement possibilities to after-treatment system of lean-burn NG engines with focus on methane and formaldehyde emission.

Firstly, homogeneous oxidation reaction of hydrocarbons in the exhaust of lean-burn NG engines is studied by combining experiments and modeling under ambient pressure and pre-turbine conditions. The effect of pressure, temperature, net concentration of NO<sub>x</sub>, and NO/NO<sub>2</sub> ratio were studied experimentally with gas compositions, which are typical for lean-burn NG engines, representing either a high methane or a high NO<sub>x</sub> slip. The results obtained by the lab-bench experiments and modeling revealed that high pressure up to 5 bar and elevated temperatures (> 550 °C) are imperative to exploit gas phase reactions for exhaust gas after-treatment. The presence of the exhaust gas component NO<sub>x</sub> significantly promotes the homogeneous oxidation of light alkanes.

Then, the experimental results were interpreted in terms of two different detailed kinetic models. Comparison of simulated concentration profiles with the experimental measurements indicate that the homogeneous kinetics can be modeled with reasonable accuracy to find the most suitable exhaust conditions needed for minimized hydrocarbon emissions.

Moreover, it was found that typical catalyst poisons such as SO<sub>2</sub> do not affect the gas phase reaction. Hence, the results presented in this thesis demonstrate that an accurate choice of proper reaction conditions make oxidation catalysts partially redundant. This is of tremendous importance for stationary and large-bore NG engines typically operated under the conditions investigated.

The effect of increased pressure relevant to pre-turbine positioning of the catalytic converter on catalytic oxidation of methane is also investigated both experimentally and numerically. The activity tests are performed for a commercial Pd-Pt model catalyst under lean conditions. The possible gas phase reactions due to high temperature and pressure are tested with an inert monolith. Catalyst activity tests are conducted for both wet and dry gas mixtures and the effect of pressure is investigated at 1, 2 and 4 bar. Experiments were carried out to check the effect of added water in the concentration range of water produced by methane oxidation on the catalyst activity. It is shown that, aside from the water in the inlet stream, the water produced by oxidation of methane in dry feed inhibited the activity of the catalyst. Based on the experimental results, a global oxidation rate equation is proposed. The reaction rate expression is first order with respect to methane and -1.15 with respect to water. Although higher pressure leads to longer residence time, it also increases the water concentration on the catalyst surface. Thus, the beneficial effect of pressure is affected by the inhibitory effect of water on the catalyst activity, particularly at lower temperatures.

The kinetics and mass transfer of total oxidation of formaldehyde in a catalytically-coated metallic monolith converter with sinusoidal-shape channels applicable in after-treatment system of lean-burn NG engines is studied. Experimental and modeling studies are performed on a commercial Pt-based oxidation catalyst. The numerical model proposed in this work is based on a thermodynamically consistent detailed surface reaction mechanism consisting of thirty elementary-like-steps among six gas-phase and ten surface species. The surface mechanism is evaluated by comparison of the results of the numerical simulation with the experimental measurements. The experimental data are derived from isothermal end-of-pipe tests over a powdered Pt-TiO<sub>2</sub>-SiO<sub>2</sub> catalyst as well as spatially-resolved concentration measurements conducted with a catalytic monolith sample over a wide range of temperature. For the description of flow field and mass transport inside the channel as well as species diffusion and chemical reaction inside the porous washcoat, a three-dimensional approach is applied and the calculations are performed, using ANSYS-FLUENT. Three different computational models representing different washcoat distributions are compared. The effects of washcoat distribution and mass transfer on kinetics and catalyst activity are investigated in detail and the numerically obtained results are compared with experimental data.

In spite of a very high intrinsic reaction rate at operation temperature, the complete conversion of formaldehyde could not be achieved experimentally. All three models have shown to operate in mass transport limited regime, where the diffusion distance from bulk to catalyst surface as well as reactant concentration play a significant role. Thus, very low levels of formaldehyde emissions are technically hard to achieve and a long catalyst is required to overcome the low diffusion rate due to the small concentration gradient. The computational results also indicate that due to individual structure of each channel of metallic monolith in real applications, they can behave distinctly from each other and one

channel does not represent the entire monolith. It is also evident from simulated data that the lack of knowledge of washcoat properties and distribution may bring about misleading results, since apparent reaction rates can be highly sensitive to this parameter for particularly catalytic reactions under mass transfer controlled conditions.

# Kurzfassung

Magermotoren zeichnen sich durch geringe CO<sub>2</sub>-Emissionen und einen niedrigen Ausstoß weiterer Schadstoffe, wie beispielsweise NO<sub>x</sub> und Feinstaub, aus. Da bereits innermotorische Maßnahmen die Emissionen von Magermotoren stark reduzieren können, gewinnen sie zunehmend an Bedeutung.

Nachteilig erweist sich jedoch der hohe Ausstoß an unverbranntem Methan, das aufgrund eines höheren Treibhauspotenzials als CO<sub>2</sub> ökologisch höchst bedenklich ist. Des Weiteren wird als Zwischenprodukt bei der Oxidation von Methan auch Formaldehyd gebildet, welches krebserregende Eigenschaften aufweist. Folglich müssen die für die Emission von Formaldehyd geltenden strengen Grenzwerte eingehalten werden. Durch die zunehmende Popularität von Magerkonzeptgasmotoren im Energiesektor müssen angemessene Maßnahmen zur Reduktion der Methan- und Formaldehydemissionen unternommen werden. In der vorliegenden Arbeit werden die technischen Beschränkungen und Verbesserungspotenziale der Abgasnachbehandlung für Magerkonzeptgasmotoren mit den Schwerpunkten Methan- und Formaldehydreduktion betrachtet.

Zunächst wurde die homogene Oxidationsreaktion im Abgasstrang von Motoren untersucht. In einer Kombination aus experimenteller und numerischer Analyse wurde zwischen atmosphärischen Bedingungen und einer Hochdruckkonfiguration durch Positionierung der Abgasanlage vor dem Turbolader unterschieden. Der Einfluss von Druck, Temperatur, NO<sub>x</sub>-Konzentration und dem NO/NO<sub>2</sub>-Verhältnis wurden experimentell mit verschiedenen für Magerkonzeptgasmotoren typischen Gaszusammensetzungen untersucht. Die Resultate der Experimente und Modellierungen verdeutlichen, dass Temperaturen über 550 °C und Drücke bis zu 5 bar notwendig sind, um die gewünschten Abbaureaktionen zu erzielen. Die Anwesenheit von NO<sub>x</sub> in der Gasphase fördert die Oxidation von leichten Alkanen signifikant.

Die experimentellen Ergebnisse wurden mit zwei kinetischen Modellen aus der Literatur präzisiert. Vergleiche zwischen Simulation und Experiment zeigen, dass die untersuchten homogenen Reaktionen durch eine Simulation mittels eines geeigneten Modells gut beschrieben werden können. Dadurch wurde es möglich, die geeigneten Abgaskonditionen zur Reduktion von Kohlenwasserstoffen mit ausreichender Genauigkeit zu bestimmen.

Des Weiteren wurde gezeigt, dass typische Katalysatorgifte, wie z.B. SO<sub>2</sub>, die Gasphasenreaktion nicht beeinträchtigen. Die Resultate dieser Arbeit verdeutlichen, dass durch die Wahl geeigneter Reaktionsbedingungen die Größe der Oxidationskatalysatoren teilweise verringert werden kann. Dies ist insbesondere für stationäre Anlagen und Großmotoren bedeutend, da diese typischerweise unter stationäre Bedingungen betrieben werden.

Die Wirkung der erhöhten Druck, der bei der Positionierung des Katalysators vor der Turbine auftritt, wurde experimentell und numerisch umfassend untersucht. Die Tests wurden mit einem Pd-Pt-Modellkatalysator unter mageren Bedingungen durchgeführt. Mögliche Gasphasenreaktionen bei hohen Temperaturen und Drücken wurden dabei mit einem inerten Monolithen untersucht. Die Aktivitätstests der Katalysatoren wurden mit Feucht- und Trockengas-Zusammensetzungen bei variierenden Drücken von 1, 2 und 4 bar durchgeführt.

Der Einfluss von Wasser, welches als Produkt der Methanoxidation entsteht, wurde mittels gesonderten Experimenten unter Zugabe von Wasser untersucht. Es konnte gezeigt werden, dass die Katalysatoraktivität durch das entstehende Wasser bei der Oxidation von Methan vermindert wird. Basierend auf diesen experimentellen Resultaten wurde eine Gleichung zur globalen Oxidationsgeschwindigkeit entwickelt. Dabei handelt es sich um eine Reaktion 1. Ordnung bezüglich Methan und der Ordnung -1.15 bezüglich Wasser. Erhöhter Druck kann sowohl zu einer höheren Verweilzeit als auch zu erhöhter Wasserkonzentration auf der Katalysatoroberfläche führen. Besonders bei niedrigen Temperaturen negiert die Anwesenheit von Wasser die vorteilhafte Wirkung des erhöhten Druckes.

Die Reaktionskinetik und Stoffübertragung zur vollständigen Oxidation von Formaldehyd wurde in einem katalytisch beschichteten Metallmonolithen untersucht, der einen sinusförmigen Querschnitt der Kanäle besitzt. Sowohl die experimentellen Untersuchungen, als auch die Simulationen wurden mit einem kommerziellen Pt-beschichteten Oxidationskatalysator durchgeführt. Das numerische Modell basiert auf einem Reaktionsmechanismus, der aus 30 elementaren Reaktionsschritten besteht. Dieser Reaktionsmechanismus wurde auf thermodynamische Konsistenz überprüft, und setzt sich aus sechs Gasphasenspezies und zehn Oberflächenspezies zusammen.

Der Oberflächenmechanismus wurde durch Kombination der Ergebnisse aus den Experimenten und den numerischen Simulationen evaluiert. Die experimentellen Daten stammen dabei aus isothermen *End-of-pipe*-Messungen über einem Pt-TiO<sub>2</sub>-SiO<sub>2</sub>-Pulverkatalysator sowie aus ortsaufgelösten Konzentrationsmessungen mit einem beschichteten Wabenkörper. Die Messungen deckten dabei ein breites Spektrum an Temperaturen ab. Sowohl zur Beschreibung des Strömungsfeldes und des Stofftransports im Kanal als auch der Spezies-Diffusion und der chemischen Reaktionen innerhalb des porösen Washcoats wurde ein 3-D Modell angewendet, welches mit einem CFD-Code berechnet wurde. Drei unterschiedliche Rechenmodelle repräsentieren dabei den Effekt der Washcoatverteilungen. Die Wirkung der unterschiedlichen Washcoatverteilungen auf den Stofftransport und die Reaktionskinetik und somit auf die Katalysatoraktivität wurden im Detail untersucht. Die erhaltenen Daten aus Simulationen und Experimenten wurden anschließend miteinander verglichen.

Ungeachtet der sehr hohen intrinsischen Reaktionsgeschwindigkeit bei den Betriebstemperaturen konnte experimentell kein vollständiger Umsatz von Formaldehyd erreicht werden. Alle drei Modelle haben gezeigt, dass die Stofftransportlimitierung eine große Rolle beim Umsatz spielt. Sowohl die Diffusionsstrecke zwischen Gasphase und Katalysatoroberfläche als auch die Konzentration des Edukts spielen eine entscheidende Rolle. Um die durch die geringen Formaldehydkonzentrationen bedingten geringen Diffusionsflüsse auszugleichen, müssten sehr lange Katalysatoren eingesetzt werden, was technisch eine große Herausforderung darstellt.

Die numerischen Modelle zeigen darüber hinaus, dass durch die individuelle Struktur jedes Kanals nicht ein einziger Kanal den gesamten Monolithen in Real-Applikationen repräsentieren kann, da sich die Kanäle merklich voneinander unterscheiden. Zudem zeigen die Simulationen, dass fehlende Informationen zu den Eigenschaften des Washcoats irreführende Resultate liefern können, da bei stofftransportlimitierter Kinetik die scheinbare Reaktionsgeschwindigkeit hoch sensibel auf die oben genannten Parameter reagiert.



# Table of Contents

Abstract .....	i
Kurzfassung .....	iv
1 Introduction .....	1
1.1 Pollutant Emissions from Natural Gas Engines .....	2
1.2 Natural Gas Engines .....	4
1.3 Emission Control .....	6
1.3.1 Catalytic Converters for Total Oxidation of Methane and Formaldehyde .....	7
1.3.2 Numerical Modeling of Catalytic Converters .....	8
1.3.3 Pre-Turbo Positioning of the Catalytic Converters .....	11
1.3.4 Gas-Phase Reaction of Hydrocarbons in the Exhaust .....	12
1.4 Outline of the Thesis .....	13
2 Mathematical Descriptions .....	15
2.1 Chemical Reactions .....	15
2.1.1 Homogenous Reactions in Gas-Phase .....	15
2.1.2 Temperature Dependency of the Rate Coefficient .....	17
2.1.3 Pressure Dependency of the Rate Coefficient .....	19
2.1.4 Heterogeneous Catalyzed Reactions .....	21
2.2 Modeling of Chemically Reacting Flows .....	24
2.2.1 Coupling of the Flow Field with Heterogeneous Chemical Reactions .....	27
2.2.2 Calculation of Diffusion Coefficients .....	29
2.3 Numerical Solution of the Differential Equations .....	31
2.3.1 Discretization of the Transport Equations .....	31
2.3.2 Solution of algebraic systems of equations .....	34
2.4 Numerical Tools .....	34
2.4.1 DETCHEM Code .....	34
2.4.2 ANSYS-FLUENT .....	35
3 Homogenous Oxidation of Light Alkanes in the Exhaust of Lean-Burn NG Engines .....	36
3.1 Experimental Set-up and Conditions .....	36

3.2	Numerical Approach.....	37
3.2.1	Estimation of Temperature Profile .....	38
3.2.2	Reaction Mechanism .....	39
3.3	Ambient Pressure .....	40
3.4	Effect of Pressure.....	41
3.5	Evaluation of Reactor Model .....	48
3.6	Effect of NO <sub>x</sub> Concentration.....	53
3.7	Effect of SO <sub>2</sub> .....	55
3.8	Summary .....	56
4	Catalytic Oxidation of Methane under Pre-Turbo Conditions .....	57
4.1	Experinental.....	57
4.1.1	Catalyst.....	57
4.1.2	Flow Reactor Experiments .....	58
4.2	Modeling Approach .....	59
4.2.1	Reactor Model .....	59
4.2.2	Washcoat Model.....	60
4.3	Kinetic Model .....	60
4.4	Results and Discussion .....	61
4.4.1	Gas-Phase Reactions.....	61
4.4.2	Effect of Pressure.....	62
4.4.3	Effect of Water .....	67
4.5	Summary .....	68
5	Kinetics of Catalytic Oxidation of Formaldehyde .....	69
5.1	Experimental.....	69
5.1.1	Exhaust Relevant Conditions.....	69
5.1.2	Indoor Formaldehyde Abatement .....	70
5.2	Modeling Approach .....	71
5.2.1	1-D Packed-Bed Model .....	71
5.3	Surface Reaction Mechanism.....	73
5.4	Results and Discussions .....	77
5.4.1	Exhaust Relevant Conditions.....	77

5.4.2	Indoor Formaldehyde Abatement .....	80
5.5	Summary .....	82
6	Formaldehyde Oxidation in Catalytic Sinusoidal-Shaped Channels .....	83
6.1	Experimental .....	83
6.1.1	Monolith Sample.....	83
6.1.2	Experimental Setup.....	83
6.2	Modeling Approach .....	84
6.2.1	Computational Domain and Boundary Conditions .....	84
6.3	Results and Discussion.....	87
6.3.1	Experimental Investigation of the Metallic Monolith .....	87
6.3.2	Computational Investigation of Metallic Monolith.....	88
6.4	Summary .....	96
7	Summary and Outlook.....	97
	References .....	101
	List of Symbols.....	116
	List of Abbreviations .....	120
	Appendix .....	122
	Acknowledgments .....	125





# 1 Introduction

Natural gas (NG) is a mixture of gaseous hydrocarbons consisting primarily of methane (up to 97%). It commonly includes varying amounts of other light alkanes such as ethane, propane and butane as well as traces of carbon dioxide, oxygen, nitrogen and hydrogen sulfide [1,2]. The composition of natural gas can vary widely depending on the field. Figure 1 demonstrates a typical composition of raw NG before refinement.

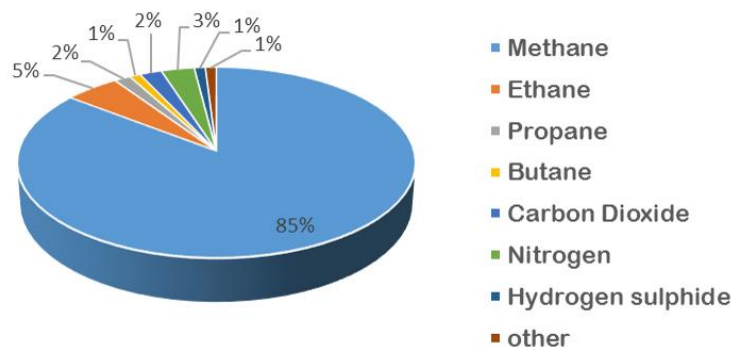


Figure 1: Typical composition of natural gas (adapted from [2]).

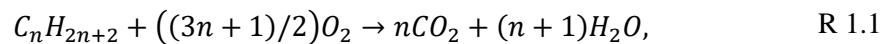
NG is a primary chemical feedstock to many chemical and petrochemical processes such as production of ammonia, methanol, ethane, syngas, hydrogen and carbon monoxide via steam and/or dry reforming. It is used in house furnaces, heaters, ovens, water boilers and cooking stoves. Besides, it can be stored and transported safely and easily burns cleaner and has lower environmental impact than other fossil fuels. The higher hydrogen-to-carbon ratio of natural gas compared to gasoline or diesel leads to less CO<sub>2</sub> emission per unit of produced power. Furthermore, due to the absence of aromatic compounds and also reduced impurities compared to diesel, NG engines produce much lower particulate matters [3]. Low cost, significantly larger reserves compared with crude oil and providing high thermal efficiency are some key factors making the natural gas an attractive fuel in various applications such as light- and heavy-duty vehicles, marine applications stationary power generation and decentralized co-generation of heat and electricity. Moreover, progresses in production of methane from biomass (biogas) and

renewable sources can make methane a sustainable fuel. However, NG engines emit some amounts of unburnt hydrocarbons (UHCs) due to incomplete combustion. Emission of unburnt and partially oxidized hydrocarbons are of environmental and health concern. These emissions consist mainly of methane, which is of particular environmental concerns, as methane is a more potent greenhouse gas than CO<sub>2</sub>, but also of formaldehyde. Formaldehyde is a flammable and colorless gas with suffocating odor which is an important raw material for many chemical compounds used in the chemical industry, e.g. phenol-, and melamine-formaldehyde resins [4]. Besides widespread industrial applications, formaldehyde contributes to photochemical smog and since June 2014 is classified as carcinogenic to humans [5].

The type and amount of harmful emissions depend strongly on the type of the engine, operation mode, air to fuel ratio and the fuel quality.

## 1.1 Pollutant Emissions from Natural Gas Engines

The ultimate chemical products of complete combustion of NG, consisting of different light alkanes are CO<sub>2</sub> and water:



However, during the actual combustion process, a number of harmful gases such as Nitrogen Oxides (NO<sub>x</sub>), Carbon Monoxide (CO), Particulate Matter/ Soot (PM) and unburnt Hydrocarbons (HCs) as well as the intermediates formed during partial oxidation of hydrocarbons like aldehydes, are released.

NO<sub>x</sub> is one of the regulated pollutants emitting from combustion engines. In the context of combustion, technically the gases nitrogen monoxide (NO) and nitrogen dioxide (NO<sub>2</sub>) are meant. The major NO<sub>x</sub> production occurs through thermal decomposition of N<sub>2</sub> and subsequent oxidation with O<sub>2</sub> at high temperatures during the combustion in the cylinder. Air-to-fuel ratio, combustion temperature and residence time affect the rate of NO<sub>x</sub> production. NO<sub>x</sub> can also be formed via the prompt formation mechanism, through early reactions of nitrogen molecules with the combustion air and hydrocarbon radicals. This mechanism is of importance only in fuel-rich conditions at low-temperatures and short residence times.

NO<sub>x</sub> reacts with water vapor, oxygen, and oxidants to form nitric acid, which comes down to the earth as acid rain. NO<sub>x</sub> causes ozone depletion, which protects the earth from the harmful UV rays [6]. It reacts with volatile organic compounds in the presence of sunlight to form Ozone, which damages the lungs especially in children, elderly and asthmatic patients [7]. NO is a colorless, odorless and tasteless

gas which affects lung functions. In the presence of oxygen, it reacts to form  $\text{NO}_2$ , which is a reddish-brown gas with a pungent odor.  $\text{NO}_2$  is also a poisonous gas, which irritates the respiratory system and blood tissues and can cause paralysis.

**CO** is formed due to incomplete oxidation of fuel mainly due to lack of oxygen or where residence time at high temperature is too short and the oxidation of hydrocarbons is not completely taking place. Carbon monoxide is a respiratory poison, which is dangerous to humans especially because of being an odorless, tasteless, colorless and non-irritating gas; therefore, it is hardly noticeable. CO has a much stronger relation to hemoglobin than oxygen, which prevents the transport of oxygen in blood and therefore can lead to acute respiratory problems, if CO passes through the lungs into the bloodstream. Even in small concentrations and short durations of exposure to CO can be lethal [8].

**PM** emission results from agglomeration of very small noncombustible traces in the fuel and lubricating oil as well as from incomplete combustion of the hydrocarbons. Particulate matter causes several health and environmental problems such as asthma, lung cancer, and other cardiovascular issues. It contributes to the pollution of air, water, and soil. It reduces the visibility and is a threat to agriculture productivity and global climate change [9,10].

**HCs** are either formed as partial oxidation products of higher hydrocarbons such as formaldehyde or remain unburnt during combustion process due to low combustion temperature, poor air-to-fuel mixing prior to, or during, combustion, incorrect air-to-fuel ratios in the cylinder during combustion and as a result of rapid cooling near the cylinder walls. The major unburnt hydrocarbon in NG-fueled engines is methane, as it constitutes up to 97% of NG. Methane emission results from low combustion temperature, leakage, and flame quenching in the combustion chamber and valve timing [11]. For instance, Figure 2 illustrates the hydrocarbon emission resulting from quenching effects inside the combustion chamber in different engine strokes [12]. Firstly, the quench layers are formed (Figure 2.a) as the flame vanishes at the cool walls and in the crevice volume. In next step (Figure 2.b) and due to the pressure drop in cylinder the quench layers are expanded. Finally (Figure 2.c), the hydrocarbon-rich cylinder wall boundary layer rolls up into a vortex as the piston moves up and the quench layer near the exhaust port exits the cylinder when the valve opens [12].

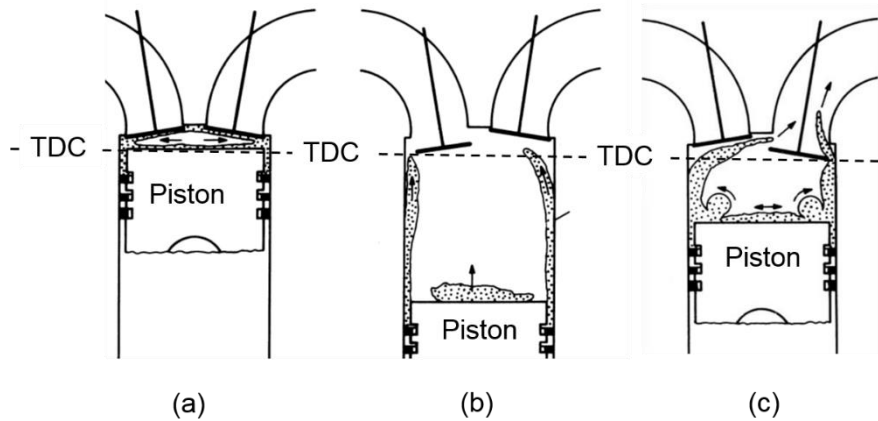


Figure 2: Schematic illustration of quench layer model for hydrocarbon emissions (adapted from [12]).

Methane is a greenhouse gas contributing in global warming more than 20 times (depending on the life time in the atmosphere) stronger than  $\text{CO}_2$  [13]. Furthermore, formaldehyde is formed as an intermediate species in the oxidation of methane and is thus present in the exhaust gas of NG engines [4]. Earlier studies show [14–17] that the formaldehyde emission is an indication of low-temperature combustion and tracing formaldehyde formation during combustion has been a method for better understanding and description of combustion reaction mechanisms [18,19]. Aside from formaldehyde formed during the flame propagation, which is apparently not responsible for the formaldehyde emission as this kind of produced formaldehyde is consumed during combustion in the presence of O and OH radicals [18], formaldehyde can be produced in the “cold region” such as near walls and in crevices and also by quenching effects. Furthermore, partial oxidation of unburnt hydrocarbons in the exhaust is reported to be another major source for formaldehyde emission [14,20,21]. Besides carcinogenic properties, a number of studies have pointed to formaldehyde as an irritant causing Asthma, eye, respiratory tract and sensory irritation [22–26].

## 1.2 Natural Gas Engines

Natural gas can be fed into different type of engines with different combustion concepts; spark ignited (SI) engines, known as gasoline engines, and compression ignited (CI) engines, known as diesel engines in dual-fueling with pilot injection, in which diesel is the pilot fuel causing the NG combustion. The SI engines utilizes an external source of ignition (spark plug), where the fuel and air are premixed with limited compression ratio. It can operate in both stoichiometric and fuel-lean concept. Increasing the compression ratio in SI engines can substantially increase the thermal efficiency. The SI engines operate on Otto-cycle. Figure 3 illustrates the working principle of four strokes SI engines. In the first stroke, a mixture of air-fuel enters the cylinder. The rising piston compressed the mixture after closing the intake

valve in compression stroke. In the third stroke, the sparking plug create the spark coincide with expansion of ignited air-fuel mixture. At the end of the cycle, the exhaust valve opens and the piston removes the combustion product from cylinder.

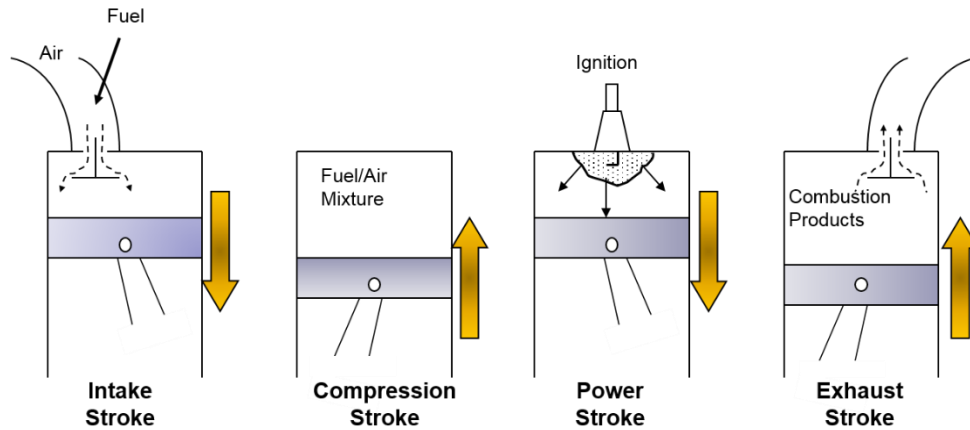


Figure 3: Schematic illustration of working principle of SI engine cycle.

The CI engines work on Diesel-cycle. This type of engines is characterized by higher compression ratio and a quality controlled torque. In conventional diesel engines, only air enters the cylinder during the intake stroke and the fuel is first injected into the cylinder after air compression (Figure 4). Due to high knock-resistance of NG, the fuel enters the combustion chamber as air-fuel mixture in CI engines. A small quantity of diesel, which acts as a pilot fuel, to initiate the NG combustion, is injected into the compressed air-fuel mixture.

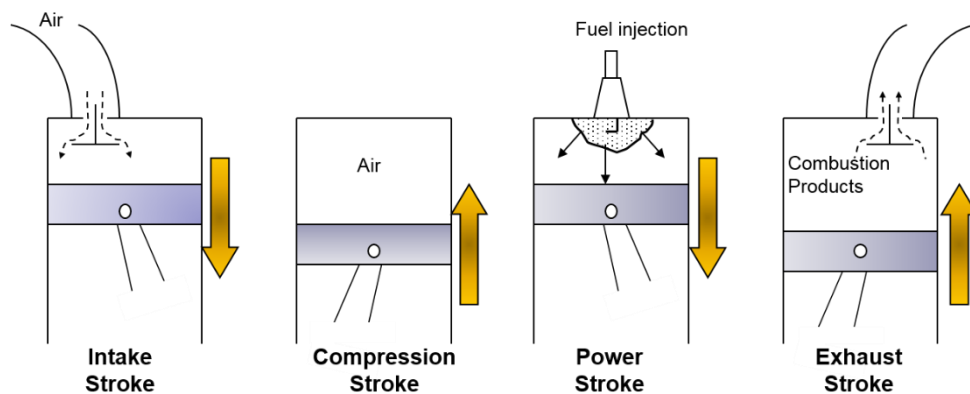


Figure 4: schematic illustration of working principle of CI engine cycle

Each type of the mentioned engines has its pros and cons from the emission control point of view. Emission of CO and non-methane hydrocarbons (NMHCs) are generally lower comparing to the other

fossil fuels. NG engines operating in stoichiometric mode emit less unburnt hydrocarbons owing to high combustion temperature. However, they produce lower thermal efficiencies compared to lean-burn engines because of the lower specific heat of the charge [11,27]. Therefore, the lean-burn engines are more attractive in view of cost and efficiency. The advanced spark timing<sup>1</sup> (compared to typical SI engines) and the high combustion temperature in NG- fueled SI engines result in high NO<sub>x</sub> emission at stoichiometric mode. At the high lambda values used in lean-burn operation, due to lower combustion temperature, the formation of NO<sub>x</sub> is much lower, hence the lean-burn NG engines are typically able to meet NO<sub>x</sub> emissions standards without or with simple after-treatment system. Besides, through higher compression ratio employed in lean-burn combustion, higher thermal efficiencies are achievable. Even though the lean-burn concept has its drawback on methane slip, they are still attractive due to lower investment and maintenance costs and have better reliability [28]. The application of a turbo charger contributes to a further improvement of the efficiency due to higher air to fuel ratio, but has its drawback on formaldehyde emission [29].

### 1.3 Emission Control

The growing global awareness towards harmful effects of hazardous pollutants emitting from combustion engines has led to impose the continually tightened regulations. Optimization of combustion process, improvements of engine hardware and controlling strategies, temperature and pressure regulation with aid of injection timing or exhaust gas recirculation are some measures taken to reduce the emissions from combustion engines. Meanwhile, the engine and combustion related strategies do not suffice to meet the requirements of new stringent regulations. Thus, after-treatment technologies and catalytic converters are nowadays an indispensable part of emission control systems.

Although the catalytic removal of NO<sub>x</sub>, CO and PM from exhaust gas are challenging tasks, there are several well-established catalytic technologies such as oxidation catalyst, three-way catalyst, NO<sub>x</sub> trap and selective reduction catalyst developed over decades for this purpose, as the first limiting regulation laws for these emissions had been imposed in 1970 [30].

---

<sup>1</sup> “After generation of spark in the cylinder, a definite time is required to start the burning of fuel. The effect of this lag time is that the maximum pressure is not reached at TDC (Top Dead Center) and it reaches late in the expansion stroke. In this case, the work area is less, and therefore, power developed per cycle and efficiency are lower. Thus, for getting maximum work output, a spark advance of 15° to 25° is required”. R. K. Rajput, Internal Combustion Engines, Laxmi publ. 1<sup>th</sup> ed. 2005

In recent years due to increased concentration of greenhouse gases, the emission of CO<sub>2</sub>, CH<sub>4</sub> and N<sub>2</sub>O, has been strictly regulated. Figure 5 demonstrates the annually decreasing CO<sub>2</sub> emission standard from 2012 projected until 2025, applicable to the trucks in the United States [31]. “The emission of CH<sub>4</sub> and N<sub>2</sub>O are regulated by defining the CO<sub>2</sub>-equivalent standard, where the N<sub>2</sub>O and CH<sub>4</sub> emissions are added to the CO<sub>2</sub> emissions using a CO<sub>2</sub> equivalence factor of 298 for N<sub>2</sub>O and of 25 for CH<sub>4</sub>” [31].

With the continuous increasing popularity of NG as fuel, it is then necessary to design an efficient after-treatment system for reduction of methane but also other harmful hydrocarbons emission from NG engines.

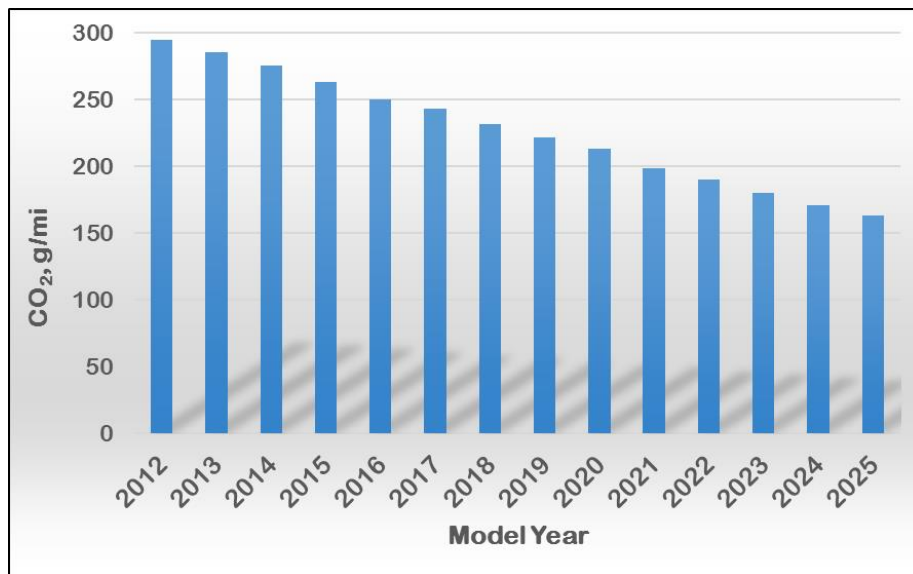


Figure 5: CO<sub>2</sub> emission standard for trucks in the US, adapted from [31].

### 1.3.1 Catalytic Converters for Total Oxidation of Methane and Formaldehyde

As mentioned above, the lean-burn type of gas-fueled engines suffers from high methane slip. Moreover, due to the occurrence of oxidation of unburnt methane and other hydrocarbons within the exhaust system, an after-treatment system is needed to achieve a formaldehyde-free exhaust gas.

Catalytic converters have commonly monolithic structures made of either ceramic or metal, consisting of hundreds of parallel channels coated with washcoat, and contain dispersed catalytic materials to increase the catalytic surface area. The catalytically active components are mostly precious noble metal particles.

Methane is chemically the most stable alkane with low reactivity thus the catalytic oxidation of methane requires a highly active catalytic material. Among all possible candidates for the catalytic material related to the total oxidation of methane, Pd-based catalysts exhibit the highest activity and are the most discussed ones in literature [32–35]. Addition of small amount of platinum to palladium catalyst has positive bearing on catalyst activity and stability [34–36]. However, several studies show a strong inhibition caused by water and catalyst poisoning by sulfide/sulfate compounds, particularly at lower temperatures during oxidation of methane over Pd-based catalysts [34,37–40]. Thus, in order to avoid sulfur poisoning and drastic catalyst deactivation by water, the required gas temperature for complete oxidation of methane to water and carbon dioxide under typical exhaust gas conditions is above 450 °C [41].

The formaldehyde emission level allocates 1-2% of total unburnt hydrocarbons, which is typically less than 100 ppm [14,19]. Owing to its toxicity, formaldehyde should be removed as much as possible from the exhaust gas of internal combustion engines. In contrast to methane, the oxidation of formaldehyde occurs at low temperatures simply achievable in the exhaust. Pt-based catalysts demonstrate generally good oxidation activity and have shown superior catalytic performance for total oxidation of formaldehyde [42–45] particularly under lean-burn conditions [46–48].

For the system efficiency, the choice of both appropriate catalytic materials and reactor structure with low pressure-drop at operation conditions, such as high gas volume flow for large engines is crucial. The ceramic monoliths can be designed with different channel shapes, commercially more widespread are the circular and square ones. The size of the channels and the thickness of the walls determine the cell density with most commonly 200-600 cells per square inch (cpsi), which corresponds to 30-95 cell per square centimeter (cpscm). Owing to porosity of the ceramic, the washcoating process of ceramic monoliths is easier than the metallic one. The metallic monoliths provide higher thermal conductivity and heat transfer compared to the ceramic substrate. Hence, metallic monolith provides lower temperature gradient along the monolith for both exothermic and endothermic reactions and higher thermal stress resistance. Furthermore, thinner channel walls contribute to less pressure-drop over metallic converters. Thus, they are attractive for various industrial applications [49–51] as well as exhaust gas after-treatment systems [52]. The metallic monoliths are made of corrugated substrate, which have asymmetric-shaped channels.

### **1.3.2 Numerical Modeling of Catalytic Converters**

Experimental studies are common methods for investigation of physical and chemical processes relevant to improvement of emission control technologies under real operation conditions. However, the execution of such experiments is often an expensive and time-consuming process.

With the progress in computer science and technologies over the last decades and development of numerical methods, the numerical simulation became a reliable tool in fluid mechanics, known as computational fluid dynamics (CFD). CFD is a cost-effective alternative to expensive experiments, through which physical and chemical processes in various geometries of different complexity can be modeled. Numerical simulations based on CFD methods serve as a powerful tool for a better understanding of the processes, estimation of the influence of different parameters and investigation of optimization possibilities in after-treatment system.

The numerical fluid dynamics models are mathematical description of the flow field based on the solution of governing equations for mass, momentum and energy giving the time-dependent values of velocity, density, pressure, temperature and species mass fraction at each point of the calculation domain. These equations represent a coupled equation system of second order non-linear partial differential equations. According to complexity of the flow field, one-, two- or three-dimensional model can be applied [53]. In this thesis, CFD calculations are performed to model the chemical reactors as well as symmetric and asymmetric channels of catalytic converters.

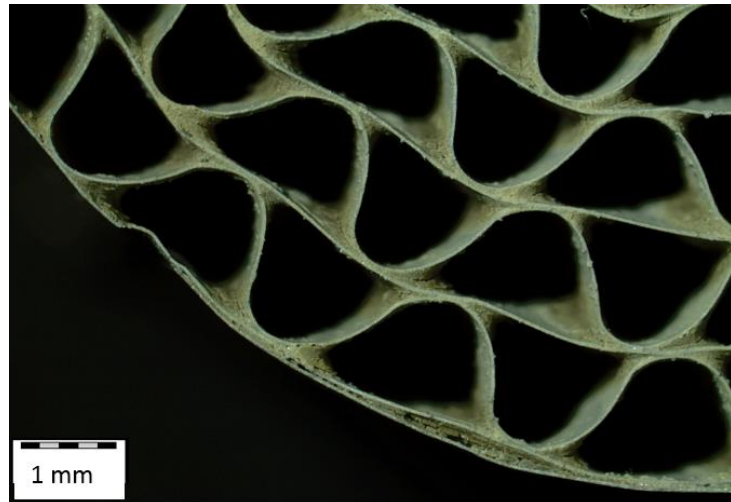


Figure 6: Cross-section of a 200 cpsi metallic honeycomb coated with the washcoat materials. The foil thickness is 0.05 mm.

As mentioned above the channels of metallic-core monoliths have usually a sinusoidal cross-section. They are coated with the washcoat materials, which is not uniformly distributed, as the washcoat materials tends to accumulate on the corners (Figure 6). Hence, some precious catalytic materials lying deep in the washcoat may be left unused. Thereby, detailed numerical simulation can shed a light on various issues concerning optimization of a catalytic system. In this regard, the evaluation of external as well as internal mass transfer limitations inside monolith reactors has been discussed by many authors

[54–60]. Summarizing the definitions and criteria stated in the literature, a reaction is called to be externally mass transfer controlled if the reaction rate is so high that the concentration of reactant in the bulk is considerably larger than the concentration at the catalytic surface. Hays and Kolaczkowski [61] define 0.03 as a threshold value for the ratio of reactant concentration at the catalyst surface and bulk concentration. If this ratio is below 0.03, the external mass transport is the rate-limiting step. As the flow inside monolith channel in exhaust after-treatment application is laminar, the mass transport from bulk to the channel surface depends merely on molecular diffusion. However, the molecular diffusion has a poor temperature dependency so that raise of temperature has no pronounced effect on transport rate as it does on reaction rate, owing to the exponential temperature dependency. The long diffusion distance between channel center and catalyst surface or low diffusion coefficient intensify the external transport limitation. Depending on washcoat parameters such as washcoat thickness, porosity, tortuosity, pore size etc., catalytic reactions can also be inhibited by diffusion limitation within washcoat layer.

Apart from the occurrence of chemical reaction, mass and heat transport considerations, the uneven washcoat and irregular asymmetric shape of the channel are the challenges for modeling of sinusoidal channels. Heat transfer and pressure-drop without consideration of chemical reactions and washcoat diffusion-reaction for sinusoidal channels have been debated in the literature using 3-D models [62,63]. Due to computational costs and efforts, many researchers tried to use simplified 1-D and 2-D models, describing physical and chemical processes within a channel of a monolith, most commonly with axisymmetric cross-sections [51,64–68]. Hayes et al. [59,69] introduced 1-D slice model based on Papadias method [70] for calculation of Sherwood number and effectiveness factor applicable for any kind of cross-section geometry but with limitation of use for sinusoidal channel. Hereby, the extreme variation in washcoat thickness results in large concentration variation around perimeter of the channel and on the surface leads to uncertainty of calculated Sherwood number. Accordingly, the effect of thickness of washcoat on the catalyst activity has been subject of many experimental as well as numerical studies since the importance of internal mass transport within the washcoat and its role of lowering the catalyst activity at high intrinsic reaction rates are widely acknowledged [55–57,71,72]. Thus, considerable efforts have been directed towards obtaining optimum washcoat thickness for different applications of monolithic reactors.

The accuracy of the aforementioned simplified models for simulation of sinusoidal channels is difficult to judge and there is a lack of 3-D models of corrugated channel containing washcoat diffusion in the literature. Thus, a detailed 3-D simulation for calculation of flow field, chemical reaction, heat and mass transport including intraporous diffusion in the washcoat can support a better understanding and interpretation of challenges and limitations for designing an optimized metallic catalyst.

Moreover, investigation of catalytic systems in a profound manner requires the knowledge of kinetics. Thereby detailed reaction mechanisms on elementary steps, which are applicable for any catalyst configurations and operation conditions, are highly demanded. Based on the data of reactions mechanism and thermodynamic properties, the formation and consumption rate of chemical species can be obtained. A reliable kinetic model can be coupled with mass and heat transport models in order to provide insight into the behavior of catalytic converters.

### **1.3.3 Pre-Turbo Positioning of the Catalytic Converters<sup>1</sup>**

The use of catalytic converters, especially in mobile applications, has its drawbacks in terms of additional weight and occupied space of the catalytic converter. Evaluation of the optimal temperature range for the efficient function of the catalytic converter is another critical issue in this context, as this temperature window is dependent on the type of the catalyst [74]. Since the exhaust gas temperature is directly related to the operation point of the engine, it is not easy to ensure the required temperature range. Especially at low engine load the temperature of the exhaust gas is often too low for the catalytic converter to work efficiently. Also, it may take a considerable amount of time to heat up the catalytic converter above its minimum working temperature. Probable solution to this problem can be the placement of the catalytic converter close to the engine manifold to rapidly heat up the catalyst by making use of the heat from the engine. In modern engines, this is limited by the exhaust gas turbine. Recent industrial work has shown that the placement of the exhaust catalysts upstream of the turbine might be possible and even favorable to the placement downstream of the turbine [75–77].

A pre-turbine placement will result in an elevated pressure up to 5 bar depending on engine design and operation point. Therefore, with resulting increase in gas density and gas temperature, a more efficient catalytic conversion can be achieved and thus less catalyst volume and mass would be sufficient compared to a post-turbine placement of the catalytic converter. Also, due to the higher gas temperature close to the engine, the catalytic converter could achieve higher conversion level [75–79]. However, the possible gained performance of the catalytic converter will always be a trade-off between sufficient exhaust after-treatment and acceptable fuel consumption due to higher back-pressure and the thermal heat capacity of the catalytic converter lowering the efficiency of the exhaust gas turbo charger. Furthermore, increasing pressure reduces the diffusion rate leading to potential mass-transport limitations of the reaction rate.

---

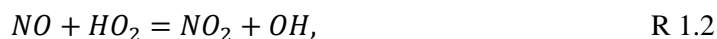
<sup>1</sup> This paragraph is taken from [73].

### 1.3.4 Gas-Phase Reaction of Hydrocarbons in the Exhaust

Due to the low exhaust gas temperature and the required (higher) temperatures for catalytic reactions highlighted above, the exhaust gas after-treatment devices are moving closer to the engine, sometimes even upstream the turbocharger, and thus operate at higher temperature and even pressure, which leads to increased possibility of homogenous oxidation reactions to take place. Several studies have reported on the possibility of oxidation of unburnt hydrocarbons such as methane and ethane mainly in the exhaust port and to some minor extent in the exhaust manifold and the tailpipe of the lean-burn NG engines [21,80–82]. The oxidation reactions in the gas-phase directly correlates with the concentration of  $\text{NO}_x$  in the gas mixture [19,21,80]. This can be attributed to decreasing the initiation temperature of hydrocarbon oxidation in the presence of the  $\text{NO}_x$  acting as a homogenous catalyst [83]. Low  $\text{NO}_x$  concentration on the order of few ppm in the exhaust reduces the initiation temperature of methane oxidation. Extensive studies are available on the promoting effect of  $\text{NO}_x$  on the gas-phase oxidation of light alkanes [83–90]. The product of hydrocarbon oxidation inside the exhaust port are mainly CO and aldehydes [19,21,91–93]. In the absence of  $\text{NO}_x$ , oxidation of methane occurs through H-abstraction with OH radicals, which proceeds by chain-propagation interaction of  $\text{CH}_3$  with  $\text{O}_2$  and formation of formaldehyde succeeded by series of oxidation reactions to carbon oxides.

The suggested  $\text{NO}_x$ -promoted oxidation mechanism from literature [21,87,88,94] involves two important cycle transformations of NO and  $\text{NO}_2$ .

Formation of OH radicals is needed for H-abstraction from  $\text{CH}_4$  through interaction of  $\text{NO}_x$  and O/H, which is described by:



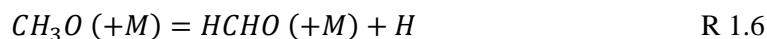
and

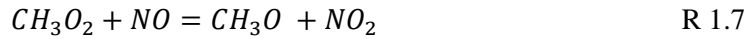


and have a lower energy barrier than the chain-branching reaction

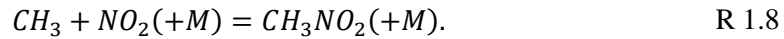


Furthermore, consumption of  $\text{CH}_3$  and formation of HCHO are also catalyzed by  $\text{NO}_x$  conversion through interaction with hydrocarbon radicals at short residence time according to:





where,  $M$  stands for third body species. Additional interactions between hydrocarbon radicals and  $NO_x$ , describing the production and consumption of nitrated hydrocarbons, e.g., nitromethane, is also considered in some mechanisms [80,86,87,95,96]



The studies of *Kristensen et al.* [21] and *Bendtsen et al.* [80] on exhaust oxidation of UHCs illustrate the feasibility of elimination of the oxidation catalyst with the aid of an extended exhaust pipe to gain longer residence time. However, the study of the effect of higher pressure on homogenous reactions and consequently longer residence time, as it is relevant to pre-turbine positioning, is scarce in the literature.

## 1.4 Outline of the Thesis

In order to utilize the benefits of gas-fueled-engines, an appropriate emission control system for the reduction of methane and formaldehyde emission is essential. This thesis deals in particular with some current shortcomings and constraints for reduction of methane and formaldehyde slip with aid of after-treatment system. Additionally, it is intended to introduce some optimization possibilities for improvement of after-treatment system of lean-burn NG engines mainly by means of numerical simulations.

In essence, this thesis addresses the following research sub-topics:

- 1) Numerical and experimental investigation of the effect of elevated pressure on *homogenous gas-phase reactions* and particularly on the formation of intermediates in the exhaust of lean-burn NG engines. The importance of gas-phase reactions and their impact on the exhaust gas composition under varying pressures and temperatures are the objective of Chapter 3. The methods and results of this study are published in:
 

B. Torkashvand, P. Lott, D. Zengel, L. Maier, M. Hettel, J.-D. Grunwaldt, O. Deutschmann, "Homogeneous Oxidation of Light Alkanes in the Exhaust of Turbocharged Lean-Burn NG engines", *Chemical Engineering Journal*, 2018. <https://doi.org/10.1016/j.cej.2018.08.186>
- 2) Numerical and experimental investigation of the effect of *Pre-Turbine* placement of oxidation catalyst i.e. increased temperature and pressure, on removal of methane slip from exhaust gas of lean-burn NG engines. Chapter 4 of this thesis is dedicated to understanding of the effect of

elevated pressure on catalytic oxidation of methane under lean conditions. The materials of this study are already published in:

B. Torkashvand, A. Gremminger, S. Valchera, M. Casapu, J.-D. Grunwaldt, O. Deutschmann, “The Impact of Pre-Turbine Catalyst Placement on Methane Oxidation in Lean-Burn Gas Engines: An Experimental and Numerical study”, *SAE Technical paper* 2017-01-1019

- 3) Development of a thermodynamically consistent multi-step detailed *surface reaction mechanism* for the catalytic oxidation of formaldehyde on platinum-based catalysts. The proposed mechanism is evaluated based on experimental data in Chapter 5 and is published in:

B. Torkashvand, L. Maier, P. Lott, T. Schedlbauer, J.-D. Grunwaldt, O. Deutschmann, “Formaldehyde Oxidation over Platinum: On the Kinetics Relevant to Exhaust Conditions of Lean-Burn Natural Gas engines”, *Topics in Catalysis* (2019) 62: 206-213.

- 4) Evaluation of the role of the external and internal *mass transport* in a metallic substrate monolith by means of 3-D simulation for catalytic oxidation of formaldehyde.
- 5) Numerical Investigation of the technical feasibility of *ultra-low emission limits* in the current monolith-like after-treatment technology. The results and discussions of last two topics are subject of Chapter 6 of this thesis. The impact of mass transport limitation and the role of washcoat distribution on overall performance of the monolithic converters are discussed in:

B. Torkashvand, L. Maier, M. Hettel, T. Schedlbauer, J.-D. Grunwaldt, O. Deutschmann,” On the Challenges and Constraints of Ultra-Low Emission Limits: Formaldehyde Oxidation in Catalytic Sinusoidal-Shaped Channels”, *Chemical Engineering Science* (2019) 195: 841-850, 2019

After discussion and evaluation of the results and methods, the thesis is concluded in Chapter 7. In this chapter, the achievements of the thesis are summarized and an outline for future works is given.

## 2 Mathematical Descriptions

### 2.1 Chemical Reactions

A chemical reaction is a process, in which chemical species are converted into others through collisions at the molecular level. The transformation of the species is a result of exchange and/ or rearrangement of the atoms. Chemical reactions occur either homogeneously or heterogeneously. In homogeneous reactions, reactant and products are in the same phase and mass transport and interaction between reactants happen in parallel steps. Heterogeneous reactions involve species in a different phase i.e. gaseous reactants and surface species (catalytic reactions) or reaction of gaseous reactants with solid material (e.g. coal combustion). Thereby, mass transfer and reaction take place throughout steps in series [97].

The reaction mechanism can be described either as a global reaction or by elementary steps. An *elementary reaction* is a chemical reaction on molecular level where reactants form products in a single step with a single transition state. The characteristic of an elementary reaction is that the stoichiometric coefficients are equal to the reaction orders. Global reactions have complex rate laws where the reaction orders in general are not integers and depend on reaction conditions. On the contrary, the reaction orders of elementary reactions always are integers and are valid for all experimental conditions. Those reaction orders can easily be derived because they equal the molecularity of the elementary reaction. The molecularity of an elementary reaction is defined as the number of reacting particles involved in the reaction to form products. Hence an elementary reaction can be *unimolecular* such as dissociation reactions or *bimolecular* [98,99].

#### 2.1.1 Homogeneous Reactions in Gas-Phase

The elementary reactions in the gas phase are generally described by:



$\chi_i$  is the  $i$ -th species,  $v'_i$ ,  $v''_i$  are the stoichiometric coefficient of reactants and products respectively.  $N_g$  is the total number of participating gas species. Parallel to Eq. 2.1 a corresponding backward reaction takes place.



The rate of formation or consumption of a species in a chemical reaction is called reaction rate and is described by the rate law. The reaction rate depends on the concentration of the participating species and temperature representing the probability of the collisions and the energy of the collisions respectively. This dependency is taken into account for a forward elementary reaction by the following expression:

$$\frac{dc_i}{dt} = (v'_{ik} - v''_{ik})k_{fk} \prod_i c_i^{a'_{ik}} \quad 2.3$$

Here  $k_{fk}$  is the rate coefficient of forward reaction and  $a'_{ik}$  is the reaction order of the reactants. In analogy, it can be written for the backward reaction:

$$\frac{dc_i}{dt} = (v''_{ik} - v'_{ik})k_{rk} \prod_{j=1}^{N_g} c_j^{a''_{ik}} \quad 2.4$$

where  $k_{rk}$  is the rate coefficient of reverse reaction and  $a''_{ik}$  is the reaction order of the products.

At chemical equilibrium the rate of forward and reverse reactions are equal in microscopic scale so that in macro scales the concentration of species does not change with time:

$$(v'_{ik} - v''_{ik})k_{fk} \prod_{j=1}^{N_g} c_j^{a'_{ik}} = (v''_{ik} - v'_{ik})k_{rk} \prod_{j=1}^{N_g} c_j^{a''_{ik}}. \quad 2.5$$

In case of an ideal gas, the ratio of reaction rate coefficients of forward and backward reactions,  $K_c$ , can be calculated from the change of the free enthalpy ( $\Delta G = -RT \ln K = \Delta H - T\Delta S$ ) at pressure of  $p^0 = 101325$  Pa according to:

$$K_c = \frac{k_{fk}}{k_{rk}} = \exp\left(-\frac{\Delta_R \overline{G}^0}{RT}\right) \left(\frac{p^0}{RT}\right)^{\sum_{i=1}^{N_g} (v'_i - v''_i)} \quad 2.6$$

With Eq 2.6 it is possible to calculate the equilibrium constant ( $K_c$ ) from thermodynamic data.

Finally, the formation rate of gas phase species  $i$  is given by sum of all reaction rates, in which the species  $i$  is participating.

$$\dot{\omega}_i = \frac{dc_i}{dt} = \sum_{k=1}^{K_g} (v'_i - v''_i)k_k \prod_{j=1}^{N_g} c_j^{a'_{ik}}. \quad 2.7$$

Here  $K_g$  is the total number of reactions in the gas-phase.

### 2.1.2 Temperature Dependency of the Rate Coefficient

The temperature dependency of the rate law can be determined either empirically known as Arrhenius approach or theoretically applying different theories such as collision theory and transition state theory.

**Arrhenius approach:** according to Arrhenius equation a chemical reaction can only take place if the kinetic energy of the colliding particles is sufficient to overcome the energy barrier known as activation energy,  $E_{ak}$ . The reaction rate coefficient of a chemical reaction can be expressed using modified Arrhenius model:

$$k_k = A_k T^{\beta_k} \exp\left(\frac{-E_{ak}}{RT}\right) \quad 2.8$$

where,  $A_k$  is the pre-exponential factor. This is also known as *frequency factor*, and represents the frequency of collisions between reactant molecules.  $\beta_k$  is the temperature exponent and describes the temperature dependency of the pre-exponential factor.  $E_{ak}$  is the activation energy and  $R$  is the universal gas constant ( $8.314 \text{ J mol}^{-1} \text{ K}^{-1}$ ). At very high temperatures or very low activation energies, the exponential term in Eq. 2.8 approaches unity. In those cases, the reaction rate is only a function of  $A_k T^{\beta}$ .

The pre-exponential factor has different meanings in uni- and bimolecular reactions. The reciprocal value of  $A_k$  corresponds to the mean lifetime of molecule for unimolecular reactions. In case of bimolecular reactions, this factor corresponds to the number of collisions and the probability of reaction [99].

The rate coefficient  $k_k$  can be determined both experimentally and theoretically. The pre-exponential factor obtained experimentally is a constant value, while the factor calculated by the aid of the mentioned theories is a function of temperature and other physical parameters.

**The collision theory** states that successful collisions are needed in order for a reaction to take place. The molecules, which lead to the successful collision must possess certain minimum amount of energy (activation energy) and collide in right orientation. The rate coefficient of a bimolecular reaction

( $A + B \rightarrow C$ ), according to the collision theory, can be expressed as:

$$k_k = Z \cdot \rho = \sigma_{AB} \sqrt{\frac{8k_B T}{\pi \mu}} \rho \quad 2.9$$

The term  $\sqrt{\frac{8k_B T}{\pi \mu}}$  represents the average velocity of colliding particles. From the kinetic theory, it is known that the average velocity of two different moving bodies can be treated as one, which has the

reduced mass of both and moves with the velocity of the center of the mass. In the above equation  $\mu$  is the reduced mass,  $k_B$  is the Boltzmann constant ( $1.381 \times 10^{-23} \text{ J K}^{-1}$ ),  $\sigma_{AB}$  is the collisional cross section and  $\rho$  is the steric factor. As not all collisions occur in correct orientation, some do not result in the corresponding reaction. The steric factor accounts for disagreement in  $A$  values between theory and experiment.

According to the collisions theory the pre-exponential factor is a weak function of temperature compared with strong temperature dependency of the reaction rate owing to the exponential term.

**The transition state theory** is based on formation of an activated complex ( $AB^*$ ) from reactants.



The probability of the reaction is then a function of the concentration of the activated complex, the consumption rate of it and the way in which the complex decomposes; returns to the reactants or rearranges the chemical bonds and forms the products. The fundamental assumption of the transition state theory is that the activated complex is in equilibrium with the reactants and products. So that the equilibrium constant can be expressed as:

$$K^* = \frac{[AB^*]}{[A][B]} \quad 2.10$$

The reaction rate is a function of the activated complex concentration and the frequency of the vibration  $\nu$  necessary for crossing the activation barrier in order to converting the activated complex to the product.

$$\frac{dP}{dt} = \nu [AB^*] = \nu K^* [A][B] \quad 2.11$$

So the reaction rate coefficient reads:

$$k = \nu K^* \quad 2.12$$

The frequency of vibrations is given by:

$$\nu = \frac{k_B T}{h} \quad 2.13$$

In which  $h$  is Planck's constant ( $6.626 \times 10^{-34} \text{ J s}$ ). Finally, the equilibrium constant depends on the thermodynamic properties of activated complex and reactants:

$$\Delta_R G^{0*} = G^0(\text{transition state}) - G^0(\text{reactants}) \quad 2.14$$

$$\Delta_R G^* = -RT \ln K^* = \Delta_R H^* - T \Delta_R S^* \quad 2.15$$

where,  $\Delta G^*$  is the Gibbs energy of the activation,  $\Delta_R H^*$  is the enthalpy of the activation and  $\Delta_R S^*$  is the entropy of the activation. Substituting Eq. 2.13 and 2.15 into Eq. 2.12, the rate constant according to transition state theory can be written as:

$$k = \frac{k_B T}{h} e^{-\frac{\Delta_R H^*}{RT}} + e^{\frac{\Delta_R S^*}{R}} \quad 2.16$$

### 2.1.3 Pressure Dependency of the Rate Coefficient

Pressure-dependency of a reaction indicate that the reaction is not a single step elementary reaction. Recombination or dissociation reactions are typical pressure-dependent reactions and are based on complex reaction sequences [99]. Decomposition is only possible if a molecule  $A$  has sufficient energy to break its bonds. The energy needed to split the bond is provided by a collision with another molecule  $M$  (third-body). The excited molecule  $A^*$  can be either deactivated through another collision and lose its energy or it decomposes via a unimolecular step into the product  $P$ . Thus, the rate of these reactions depends on the number of collisions and accordingly on pressure.



At very low pressures, the number of collisions is limited and therefore the reaction rate is proportional to the concentration of the both third-body ( $M$ ) and molecule  $A$  (Eq. 2.17). At high pressure, the reaction rate is first order with respect to the concentration of molecule  $A$  and zero order with respect to the concentration of  $M$  (Eq. 2.18). The rate constant corresponding to these two pressure limits can be modeled by Arrhenius equation.

$$r = k_0 C_A C_M, \quad k_0 = A_0 T^{\beta_0} \exp\left(\frac{-E_{a0}}{RT}\right) \quad 2.17$$

$$r = k_\infty C_A, \quad k_\infty = A_\infty T^{\beta_\infty} \exp\left(\frac{-E_{a\infty}}{RT}\right) \quad 2.18$$

At intermediate pressure, the so-called *pressure fall-off region*, the reaction rate is neither second-order nor first-order. There are several methods for the description of the reaction rate in the *fall-off region*.

In this work, the Troe method [100], which is a modified expression of Lindemann theory [101,102], is applied and therefore will be briefly presented.

According to the Lindemann theory the apparent pressure-dependent rate constant can be written as:

$$k = k_{\infty} \left( \frac{p_r}{1 + p_r} \right) F, \quad 2.19$$

where  $p_r$  is the reduced pressure:

$$p_r = \frac{k_0[M]}{k_{\infty}} \quad 2.20$$

The effective concentration of third-body  $[M]$  corresponds to concentration of all participating molecules multiplied by their collision efficiencies  $m_{yi}$ :

$$[M] = \sum_i m_{yi} [C_i]. \quad 2.21$$

$F$  is the broadening factor in the *fall-off region* and is equal to 1 for the Lindemann model. According to Troe model [103],  $F$  is a more complex function and is given by the description of the center of the *fall-off range*,  $F_{cent}$ ,

$$\log F = \left[ 1 + \left( \frac{\log p_r + c}{n - d(\log p_r + c)} \right)^2 \right]^{-1} \log F_{cent}. \quad 2.22$$

With

$$\begin{aligned} c &= -0.4 - 0.67 \log F_{cent}, \\ n &= -0.75 - 1.27 \log F_{cent}, \\ d &= -0.14 \end{aligned} \quad 2.23$$

and

$$F_{cent} = \alpha \cdot \exp\left(-\frac{T}{T^*}\right) + \exp\left(-\frac{T}{T^{**}}\right) + (1 - \alpha) \cdot \exp\left(-\frac{T}{T^{***}}\right). \quad 2.24$$

There are ten parameters required for the calculation of the broadening factor  $F$ . The formalism of Troe can be used to determine the rate constant at each temperature and pressure.

Figure 7 illustrates the pressure dependency of rate constant at low, high and intermediate pressure range and the comparison between Lindemann and Troe model.

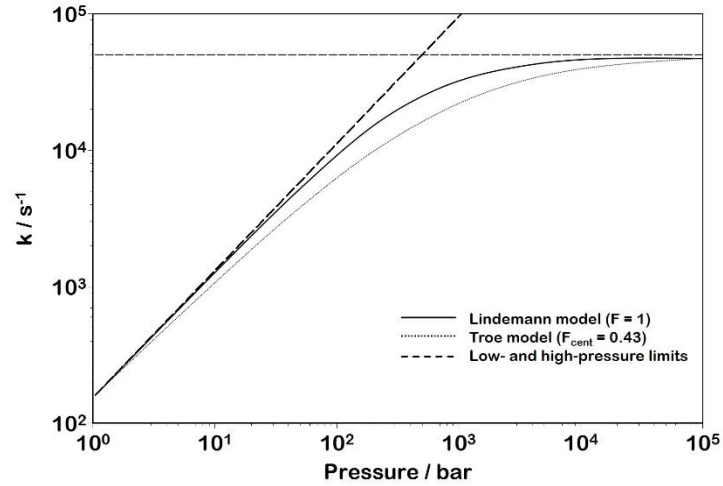


Figure 7: Rate constant as function of pressure at low pressure ( $k_0$ ), at high pressure ( $k_\infty$ ) and in fall-off region applying Lindemann and Troe model for reaction  $\text{H}_2\text{O}_2 \leftrightarrow 2\text{OH}$  [98].

#### 2.1.4 Heterogeneous Catalyzed Reactions

Unlike homogeneous systems, in heterogeneous catalysis, the reactants and the catalyst are in different phases. Hence, mass transfer plays a fundamental role. In particular the sequential steps, which occur during a catalytic reaction, are [104]:

1. External or interphase diffusion of reactants: diffusion from the bulk fluid to the catalytic surface through the boundary layer
2. Internal or intraphase diffusion of reactants: diffusion through the pores of the washcoat
3. Adsorption of the reactants on the active sites of the catalyst surface
4. Reaction on the catalyst sites
5. Desorption of products from the catalyst sites
6. Internal or intraphase diffusion of products: diffusion through the pores of the washcoat
7. External or interphase diffusion of products: diffusion from the catalytic surface to the bulk fluid

Alike gas-phase reactions, the micro reaction kinetics (steps 3-5) on the catalytic surface can be expressed using the reaction rate coefficient [53,105].

$$\dot{s}_i = \frac{dc_i}{dt} = \sum_{k=1}^{K_s} (v'_i - v''_i) k_k \prod_{j=1}^{N_g+N_s} c_j^{v'_{jk}} \quad 2.25$$

In the above equation  $K_s$  is the number of surface reactions including adsorption and desorption reactions.

The various adsorbates occupy different number of vacancies on the catalyst surface. It is therefore more practical using coverage degrees  $\theta_i$  instead of concentration of adsorbed species  $c_{i,s}$  for the description of surface reactions. The coverage of species  $i$  is defined by:

$$\theta_i = \frac{c_{i,s}\sigma_i}{\Gamma_{cat}} \quad 2.26$$

where,  $\Gamma_{cat}$  represent the surface site density and  $\sigma_i$  the number of sites occupied by one particle of the species  $i$  respectively. The sum of all coverages and available vacancies should fulfill:

$$\sum_{i=1}^{N_s} \theta_i = 1. \quad 2.27$$

### Mean-field approximation

The proposed detailed catalytic reaction mechanism in this work is developed using the mean-field approximation. Thereby, the adsorbates are assumed to be randomly distributed on the surface, and their temperature and coverage depend only on the macroscopic position on the catalyst surface [106,107]. It is also assumed that there is no interaction between adjacent adsorbates and surface vacancies are treated equally using averaged parameters for various crystallographic planes.

The increasing coverages of adsorbed species alter the adsorption probability on the surface. A modified Arrhenius expression, which accounts for coverage dependency of the heat of formation of surface intermediate  $i$  resulting in additional coverage-dependent contributions  $\varepsilon_i$  to the activation barrier  $E_{ak}$ , is used to describe the rate constant of surface reactions.

$$k_k = A_k \cdot T^{\beta_k} \cdot \exp\left[-\frac{E_{ak}}{RT}\right] \cdot \prod_{i=1}^{N_s} \exp\left[\frac{\varepsilon_i \theta_i}{RT}\right]. \quad 2.28$$

Hereby  $\varepsilon_i$  is the coverage-dependent part of the activation energy ( $\varepsilon_i > 0$  represent repulsive self-interactions of species  $i$  on the surface).

Rate constants for adsorption reactions are modeled through sticking coefficients. Considering the initial sticking coefficient  $s_i^0$  of the gas-phase species  $i$  with respect to the catalyst surface at zero coverage, the pre-exponential factor of an adsorption reaction  $k$  involving gas-phase species  $i$  is given as:

$$A_k^{\text{ads}} = \frac{1}{\Gamma_{cat}^{n_k-1}} s_i^0 \sqrt{\frac{RT}{2\pi M_i}}. \quad 2.29$$

Here,  $n_k$  is the molecularity of the adsorption step  $k$  with  $n_k = 2$  for molecular adsorption,  $n_k = 3$  for dissociative adsorption.

## Thermodynamic Consistency

One of the requirements of a microkinetic model is that in the limit of infinite time the thermodynamic equilibrium is properly predicted. A reliable reaction mechanism should ensure enthalpic and entropic consistency.

In this section, derivations of the equations are written as they are given in [108].

The equilibrium of a chemical reaction for an arbitrary reaction only depends on the thermodynamic properties of the species involved.

$$\sum_{i=1}^{N_g+N_s} v'_{ik} \chi_i \xrightleftharpoons[k_r]{k_f} \sum_{i=1}^{N_g+N_s} v''_{ik} \chi_i . \quad 2.30$$

The equilibrium constant,  $K_{pk}$ , which describes the equilibrium composition in terms of equilibrium activities,  $a_i^{eq}$ , and their stoichiometric coefficients,  $v_{ik} = v''_{ik} - v'_{ik}$ , is a function of temperature  $T$

$$K_{pk}(T) = \prod_i (a_i^{eq})^{v_{ik}} = \exp\left(-\frac{\Delta_k G^0}{RT}\right). \quad 2.31$$

$R$  is the gas constant. The change of free enthalpy  $\Delta_R G^0$  at normal pressure  $P^0$  can be written as

$$\Delta_R G^0 = \sum_i v_{ik} G_i^0(T). \quad 2.32$$

Here, the  $G_i^0(T)$  is the standard free enthalpy of the species  $i$ , i.e., the chemical potential at normal pressure.

In equilibrium, the rate coefficients of forward and reverse reactions obey the equation

$$\frac{K_{fk}}{K_{rk}} = K_{pk} \cdot \prod_i (c_i^0)^{v_{ik}}. \quad 2.33$$

The  $c_i^0$  are reference concentrations at normal pressure, i.e.,  $c_i^0 = p^0/RT$  for gas-phase species and  $c_i^0 = \Gamma/\sigma_i$  for surface species, in which  $\Gamma$  is the surface site density and  $\sigma_i$  is the number of the surface sites occupied by the species  $i$ . The rate coefficients of each reaction have to fulfill the Eq. 2.33. However, some of the  $G_i^0$  involved on the right hand side of the equation are unknown. Usually, there are more reversible reactions than unknown chemical potentials. Thus, we have an over-determined system of equations with respect to the unknown  $G_i^0$ .

In logarithmic form, we can write Eq. 2.33 as

$$\ln K_{fk} - \ln K_{rk} = -\frac{1}{RT} \sum_i v_{ik} G_i^0(T) + \ln \left( \prod_i (c_i^0)^{v_{ik}} \right). \quad 2.34$$

For a fixed temperature, this is a linear equation system in terms of the chemical potentials  $G_i^0$  and the logarithms of the rate coefficients. After removal of the unknown  $G_i^0$  by Gaussian elimination, an under-determined system of linear equations for  $\ln K_{fk}$  and  $\ln K_{rk}$  are left. Allowing a change of rate coefficients of selected reactions, the minimal changes required to satisfy the linear equation system at a fixed temperature can be calculated using a weighted least-square fit. This procedure is repeated for several temperatures and new Arrhenius parameters are fitted to the new temperature dependency of the rate coefficients. Details of this method can be found in [108,109].

## 2.2 Modeling of Chemically Reacting Flows

Modeling chemical reactors is distinctly challenging owing to complex physical and chemical processes simultaneously taking place inside a reactor. The numerical model of the reactive flows should be capable of predicting the individual processes and their interactions. A reliable model accounts for accurate description of flow field, chemical reaction on the surface as well as in the gas-phase coupled with heat and mass transfer phenomena. Depending on reactor type and boundary conditions, different assumptions can be made to simplify the models required for simulation of reactive flows. This section introduces briefly the principle of modeling of reactive flows. More details to fluid dynamics, transport phenomena and chemical processes can be found in a number of textbooks [105,110–114].

As long as a fluid can be treated as continuum, the most sophisticated description of flow field of multicomponent mixture is given by the transient three-dimensional Navier-Stokes equations together with the energy and species governing equations. These equations couple the macroscopic intensive properties, which are independent from the amount of matter viz. density, velocity and temperature within a certain spatial region called the *control volume*, building a coupled equation system of second order non-linear partial differential equations [53,112,115].

The principle of mass conservation leads to the *mass continuity equation*. The rate of change of total mass (density,  $\rho$ ) for every point within the *control volume* in differential form is given by:

$$\frac{\partial \rho}{\partial t} + \frac{\partial(\rho v_i)}{\partial x_i} = S_m \quad 2.35$$

In Eq. 2.35,  $\rho$  is density and  $v_i$  is the velocity component and  $x_i$  ( $i=1,2,3$ ) are the Cartesian coordinates. The source term  $S_m$  disappears unless mass is either deposited on or ablated from the solid surfaces.

The first term on the right side corresponds to the local variation of  $\rho$  over time and the second term is the convective derivative. In case of steady state conditions, the first term on the right side of Eq. 2.35 vanishes. Here, the Einstein notation is applied. According to this, when an index variable appears twice in a single term and is not otherwise defined, it implies summation of that term over all the values of the index, except if the index refers to a chemical species.

The change of momentum in *control volume* is defined by the sum of the net momentum flow rate from the control surface, body and surface forces. The body forces act on the volumetric mass of the fluid such as gravitational or magnetic forces and surface forces act on the surface of fluid element, consisting of shear and normal stress. The differential form of the conservation of the momentum is given by:

$$\frac{\partial(\rho v_i)}{\partial t} + \frac{\partial(\rho v_i v_j)}{\partial x_j} + \frac{\partial p}{\partial x_i} + \frac{\partial \tau_{ij}}{\partial x_j} = \rho g_i, \quad 2.36$$

Where  $p$  is the static pressure,  $\tau_{ij}$  is the stress tensor, and  $\rho g_i$  represents the components of the gravitational acceleration  $\vec{g}$  in the direction of Cartesian coordinates  $x_j$ . The only body force considered here, gravity, is often neglected when modeling chemical reactors. The stress tensor is expressed as:

$$\tau_{ij} = -\mu \left( \frac{\partial v_i}{\partial x_j} + \frac{\partial v_j}{\partial x_i} \right) - \frac{2}{3} \mu \frac{\partial v_k}{\partial x_k} \delta_{ij}. \quad 2.37$$

In Eq. 2.37,  $\mu$  is the mixture viscosity and  $\delta_{ij}$  is the Kronecker delta, which is unity for  $i = j$ , else zero. For a multicomponent system, in which species transport and chemical reactions are of importance, additional conservation equations for description of species mass fractions are mandatory. Through chemical reactions, the species are converted into each other. Thereby, the mass fraction  $Y_i$  describes the exact fraction of species  $i$  in the gas mixture. The mass  $m_i$  of each species  $i$  obeys the conservation law, which leads to following set of governing equations:

$$\frac{\partial(\rho Y_i)}{\partial t} + \frac{\partial(\rho v_j Y_i)}{\partial x_j} = \frac{\partial(j_{i,j})}{\partial x_j} + R_i^{hom}, \quad (i = 1, \dots, N_g) \quad 2.38$$

In the above equation,  $Y_i$  is the mass fraction of species  $i$  in the mixture,  $R_i^{hom}$  is the net rate of production due to homogenous chemical reactions and  $j_{i,j}$  is the diffusion mass flux:

$$j_{i,j} = -\rho \frac{Y_i}{X_j} D_{i,M} \frac{\partial X_i}{\partial x_j} - \frac{D_{i,T}}{T} \frac{\partial T}{\partial x_j} \quad 2.39$$

The first term of the Eq. 2.39 on the right hand side represents the diffusion caused by concentration gradient and the second term corresponds to the diffusion caused by the temperature gradient between

different layers of fluid.  $D_{i,M}$  is the effective diffusion coefficient of species  $i$  in the mixture and  $D_{i,T}$  is the thermal diffusion coefficient. The molar fraction  $X_i$  is related to the mass fraction  $Y_i$  by:

$$Y_i = \frac{M_i}{\bar{M}} X_i \quad 2.40$$

$M_i$  is the molar mass of species  $i$  in the gas mixture and  $\bar{M}$  is the molar mass of the mixture:

$$\bar{M} = \frac{1}{\sum_{i=1}^{N_g} \frac{Y_i}{M_i}} \quad 2.41$$

The temperature of the flow is defined by the energy conservation equation. This equation describes the rate of change of internal energy in *control volume*. There are several reasons causing the change of internal energy:

- 1) Heat flux from and into the *control volume*
- 2) Thermal conduction
- 3) Mass diffusion
- 4) Chemical reactions
- 5) External sources of energy
- 6) Work done on the element due to body and surface forces

The energy governing equation is commonly expressed in terms of the specific enthalpy  $h$ :

$$\frac{\partial(\rho h)}{\partial t} + \frac{\partial(\rho v_j h)}{\partial x_j} + \frac{\partial(j_{q,j})}{\partial x_j} = \frac{\partial p}{\partial t} + v_j \frac{\partial p}{\partial x_j} - \tau_{jk} \frac{\partial v_j}{\partial x_k} + S_h, \quad 2.42$$

With  $S_h$  being the heat source. In multicomponent mixtures, the diffusive heat transport is divided to conductive heat transport and diffusion of mass:

$$j_{q,j} = -\lambda \frac{\partial T}{\partial x_j} + \sum_{i=1}^{N_g} h_i j_{i,j}. \quad 2.43$$

with  $\lambda$  as thermal conductivity of the mixture and  $h_i$  the specific enthalpy of species  $i$ . Following the first law of thermodynamics, the specific species enthalpy is expressed by:

$$h_i(T) = h_i(T_{ref}) + \int_{T_{ref}}^T c_{p,i}(T') dT', \quad 2.44$$

where  $c_{p,i}$  is the specific heat capacity at constant pressure.

The relation between the thermodynamic variables, density, pressure and temperature is given by the equation of state. The simplest model of this relation for gaseous flows is the ideal gas equation:

$$p = \rho \frac{R}{M} T \quad 2.45$$

In order to obtain unique solutions of governing equations, determination of boundary conditions with respect to the geometrical domain of fluid flow is required. Finally, the solution of this system results in time-dependent velocity component in x-, y-, and z-direction, pressure, temperature and density for each point of the flow field.

## 2.2.1 Coupling of the Flow Field with Heterogeneous Chemical Reactions

### Instantaneous diffusion

In this model, it is assumed that an infinite thin catalyst layer is distributed on the gas-solid interface so that mass transport within the washcoat is infinitely fast. The effect of washcoat parameters such as thickness, porosity or pore diameters of the inner pores is neglected. This means that the mass flux of each gas species due to diffusion and convection to/from the surface is balanced with its rate of consumption/production on the reacting surface. In this case, the species continuity equations at the gas-surface interface and under steady-state conditions is given by:

$$j_i = -R_i^{het}. \quad 2.46$$

$j_i$  is the diffusion flux of species  $i$  and  $R_i^{het}$  is the heterogeneous surface reaction rate:

$$R_i^{het} = \dot{s}_i M_i F_{cat/geo}. \quad 2.47$$

The term  $F_{cat/geo}$  is the ratio of the active catalytic surface area  $A_{cat}$  and the geometric surface area  $A_{geo}$

$$F_{cat/geo} = \frac{A_{cat}}{A_{geo}} \quad 2.48$$

The first boundary condition states that all velocity components vanish on the surface.

### Effectiveness factor approach

The simplest model to include the effect of internal mass transfer resistance within the washcoat layer is the effectiveness factor based on Thiele modulus. This model assumes that overall reactivity can be determined by one target species [53,116]. The effectiveness factor  $\eta$  of species  $i$  is given by:

$$\eta_i = \frac{\dot{s}_{i,eff}}{\dot{s}_i}, \quad 2.49$$

with  $\dot{s}_{i,eff}$  the effective surface reaction rate inside the washcoat. In case of a first-order reaction in homogenous porous washcoat and under steady-state conditions, the effectiveness factor can be calculated analytically:

$$\eta_i = \frac{\tanh(\varphi_i)}{\varphi_i}, \quad 2.50$$

where  $\varphi_i$  is the Thiele module that for a rate law of first order is defined by:

$$\varphi_i = L \sqrt{\frac{\dot{s}_i \gamma}{D_{i,eff} c_{i,0}}}. \quad 2.51$$

in which  $L$  is the thickness of the washcoat layer,  $\gamma$  is the ratio of the catalytic surface area to geometrical washcoat volume,  $D_{i,eff}$  is the effective diffusion coefficient of species  $i$ , and  $c_{i,0}$  is the concentration of species  $i$  at the gas-solid interface. This approach can only be applied under conditions that the reaction rate of one target species represents the overall activity. Consequently, application of this models means that the diffusion coefficient of all present species is the same [53].

### One-dimensional reaction-diffusion-model in the washcoat

The reaction-diffusion model serves a more precise description of mass transport within the washcoat as it calculates essentially the reaction-diffusion equations for all participating species. It assumes that the species transport within the washcoat is only due to the diffusion caused by concentration gradients in normal direction to the gas-solid boundary inside the washcoat. In transient form, this equation can be written as:

$$\frac{\partial c_{i,w}}{\partial t} = -D_{i,eff} \frac{\partial c_{i,w}}{\partial z} + \gamma \dot{s}_{i,w} \quad 2.52$$

With  $c_{i,w}$  as the molar concentration of specie  $i$  inside the washcoat and  $\dot{s}_{i,w}$  as the surface reaction rate of specie  $i$  in the washcoat.

### Porous washcoat layer

The 3-D models with higher complexity than zero and 1-D models are the most sophisticated approach for description of mass transport coupled with catalytic reactions within the washcoat. Porous medium model applicable for homogenous porous media provides a good description of washcoat with low calculation efforts. In this approach, the entire system of conservation equations is considered in both fluid and porous medium domain. In the porous medium domain, the momentum equations are extended

by an additional source term, consisting of viscous and inertial loss terms that cause a pressure-drop in the porous medium, which is proportional to the respective velocity components in flow directions Eq 2.53. The first term on the right side of the Eq 2.53 represents the viscous loss term (Darcy law) and the second one the inertial momentum loss relevant at high flow velocity. Here,  $\mu$  is the dynamic viscosity,  $\alpha$  the permeability, and  $C$  the inertial resistance factor [117]. However, the high viscous resistance caused by very low permeability of the porous washcoat in the honeycomb catalytic converters with pore size as small as 12-25 nm leads to negligible convective species flux inside the washcoat [72].

$$\vec{S} = - \left( \frac{\mu}{\alpha} + \frac{\rho C |\vec{v}|}{2} \right) \vec{v}. \quad 2.53$$

The chemical reactions in the porous washcoat are added as a source term to the species conservation:

$$\frac{\partial}{\partial t} (\rho Y_i) + \nabla \cdot (\rho \vec{v} Y_i) = -\nabla \cdot \vec{J}_i + R_i^{het} + S_i. \quad 2.54$$

Here  $S_i$  represents an arbitrary source or sink. The diffusive mass flux  $\vec{J}_i$  is then given by Eq. 2.39. The diffusion coefficient  $D_{i,M}$  should be replaced by  $D_{i,eff}$  inside the porous medium domain. The calculation method of  $D_{i,eff}$  is briefly described in the following section.

## 2.2.2 Calculation of Diffusion Coefficients

### Gas-phase

Diffusion refers to a mass transport process due to concentration or temperature gradient in a mixture, resulting in a uniform distribution of the individual components in a multicomponent system. For the calculation of diffusive flux in a multicomponent system (made of species  $i$  and  $j$ ), the averaged diffusion coefficient  $D_{i,M}$  is introduced as:

$$D_{i,M} = \frac{1 - Y_i}{\sum_{j \neq i} \frac{X_j}{D_{ij}}} \quad 2.55$$

where  $D_{ij}$  is the binary diffusion coefficient, which is calculated from the kinetic theory of diluted gases by Chapman-Enskog correlation [105]:

$$D_{ij} = \frac{3}{16} \frac{\sqrt{2\pi k_B^3 T^3 / m_{ij}}}{p \theta_{ij}^2 \Omega_{ij}^{(1,1)*}(T_{ij}^*)} \quad 2.56$$

in which  $m_{ij}$ ,  $\theta_{ij}$ ,  $T_{ij}^*$  and  $\Omega_{ij}^{(1,1)*}$  are the reduced mass, length-scale in the interaction between two molecules, reduced temperature and the temperature dependence of the collision integral according to Lennard-Jones potential, respectively.

## Washcoat

For the modeling of the diffusion step inside the washcoat, the effective diffusion coefficient  $D_{i,\text{eff}}$  is needed, which is a function of molecular  $D_{i,\text{M}}$  and Knudsen  $D_{i,\text{Knud}}$  diffusion coefficients. The diffusive mass transport inside porous media is determined based on molecule-molecule collisions and molecule-pore collisions. The diffusion process in porous media is strongly influenced by the pore size distribution. If the mean free path of the gaseous species is smaller than the mean pore diameter, the transport in the washcoat occurs mainly due to intermolecular collisions. Therefore, the effective diffusion coefficients are calculated from the averaged molecular diffusion coefficients [118–120]:

$$D_{i,\text{eff}} = \frac{\varepsilon}{\tau} (D_{i,\text{M}}), \quad 2.57$$

where  $\varepsilon$  is the washcoat porosity and  $\tau$  is the tortuosity of the pores. Porosity is defined as the ratio of void volume and geometrical volume of the washcoat. Tortuosity is a factor, which account for deviation of pore structure from ideal-cylinder.

If the pore diameter is sufficiently small and the mean free path of the gaseous species is larger than the pore diameter, the molecule-pore collisions occur more often than molecule-molecule collisions. This regime of mass transport in the washcoat is called ‘Knudsen diffusion’. The Knudsen diffusion coefficient of species  $i$  in a porous domain is calculated based on kinetic theory of the gases and the ideal gas law [56,105]:

$$D_{i,\text{Knud}} = \frac{d_p}{3} \sqrt{\frac{8RT}{\pi M_i}}, \quad 2.58$$

in which  $d_p$  is the mean pore diameter. The effective diffusion coefficient in this case is then expressed by:

$$D_{i,\text{eff}} = \frac{\varepsilon}{\tau} D_{i,\text{Knud}} \quad 2.59$$

In porous medium with pore diameters in the range of the mean free path of gaseous molecules, the diffusive mass transport is a function of both molecule-molecule collisions and molecule-pore collisions:

$$\frac{1}{D_{i,\text{eff}}} = \frac{\tau}{\varepsilon} \left( \frac{1}{D_{i,\text{M}}} + \frac{1}{D_{i,\text{Knud}}} \right) \quad 2.60$$

This condition is common in after-treatment catalytic converters.

## 2.3 Numerical Solution of the Differential Equations

As shown in section 2.2, the mathematical model for description of the flow field is a system of coupled non-linear partial differential equations. Indeed, there is no analytic solution for such systems and therefore the numerical methods should be applied. The first step in numerical solution is the transportation of differential equations into algebraic equations through a discretization process. The general transport equation for a flow variable  $\phi$  is given by:

$$\frac{\partial(\rho\phi)}{\partial t} + \frac{\partial(\rho u_i \phi)}{\partial x_i} = \frac{\partial}{\partial x_i} \left( \Gamma_\phi \frac{\partial \phi}{\partial x_i} \right) + S_\phi \quad 2.61$$

The first term on the right hand side is the time-dependent change of variable  $\phi$  and the second term is the convective term. On the left hand side of the Eq. 2.61 the first term represents the diffusive transport with  $\Gamma$  as diffusivity and the second term is an arbitrary source term, respectively. Under steady-state conditions, the time-dependent term is eliminated.

### 2.3.1 Discretization of the Transport Equations

The solution of the governing differential equations is approximated by discretization process. Discretization is referred to a process in which the continuous distribution of dependent variable  $\phi$  is represented by  $\phi$  -values at discrete positions so that the analytic solution of the differential equations can be replaced by numerical solution; so-called discretization equations [110]. The discretized domain is called grid. A discretization equation is an algebraic relation connecting the values of  $\phi$  for a group of grid points. The solution of discretization equations for a large number of grid points is expected to approach the exact solution of the differential equations [111]. This property is denoted as *convergence*.

There are different discretization methods. Three of the most commonly used methods are the finite-difference method (FDM), the finite-element method (FEM) and the finite-volume method (FVM). In this work, the finite-volume method (ANSYS-FLUENT) and finite-difference method (DETCHEM) are applied.

The FDM for discretization of a differential equation is based on approximating the derivatives in the differential equation by truncated Taylor series [111]. It is a straightforward method, in which the computational domain is divided into volume elements and the variable values will be obtained at each nodal point of the grid.

In FVM, the calculation domain is divided into non-overlapping volume elements (*control volumes*) so that the variable of interest is located at the centroid of the control volume. The differential equation is

then integrated over each volume element. The variation of the variable between the cell centroids is given by interpolated variable profiles. The discretization equation obtained in this manner expresses the conservation principle for variable  $\phi$ , which is satisfied for each volume element as well as any group of control volumes and for any number of elements [111].

Finite volume method uses the integral form of the equations and is based on the cell-averaged values. The integration of Eq. 2.61 over an arbitrary *control volume* with application of Gauss's theorem results in:

$$\int_V \frac{\partial(\rho\phi)}{\partial t} dV + \int_A (\rho u_i \phi) n_i dA = \int_A \left( \Gamma_\phi \frac{\partial \phi}{\partial x_i} \right) n_i dA + \int_V S_\phi dV \quad 2.62$$

Here,  $A$  denotes the surface of the control volume and  $n_i$  the unit normal vector to the surface.

### 2.3.1.1 Discretization of the Convective Term

The convective term in Eq. 2.62 corresponds to the flows over control volume edges:

$$\int_A (\rho u_i \phi) n_i dA = \sum_c \int_A (\rho u_i \phi) n_{ci} dA_c . \quad 2.63$$

Applying the cell-centered approach, the surface integral is approximated by

$$\sum_c \int_A (\rho u_i \phi) n_{ci} dA_c = \sum_c (\rho u_i \bar{n}_{ci} \delta A_c) \phi . \quad 2.64$$

Where  $\rho$  and  $u_i$  are assumed to be constant at control volume edges. For the further approximation of the convective fluxes, it is necessary to approximate  $\phi_c$  by variable values in the *control volume* centers. In general, this involves using neighboring nodal values [113]. In the present study, the second order Upwind scheme is used for discretization of the convective term. In this scheme, the unknown variable  $\phi$  is approximated by a step function, taking the flow direction into account.

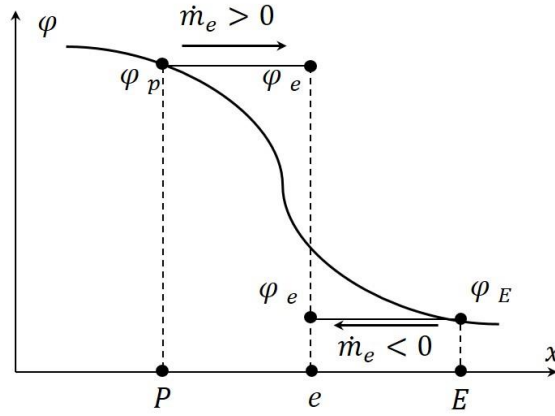


Figure 8: Flux dependent approximation of  $\phi_e$  using Upwind scheme. Adapted from [113].

As shown in Figure 8: the value  $\phi_e$  is assumed to be equal to the value at the upstream node.

$$\begin{aligned}\phi_e &= \phi_P, & \text{if } \dot{m}_e > 0, \\ \phi_e &= \phi_E, & \text{if } \dot{m}_e < 0.\end{aligned}$$

The upwind scheme gives a good approximation if the convective flow is perpendicular to the control volume faces. Otherwise, the approximation can be quite inaccurate. Additionally, for large mass fluxes very fine grids are essential to obtain an accurate solution. Increasing the number of points for the approximation increases also the accuracy. In the second-order Upwind scheme, two upstream points are considered.

### 2.3.1.2 Discretization of the Diffusion Term

In analogy to the convective flux and with application of cell-centered approach, the diffusion term in Eq. 2.62 is determined by:

$$\int_A \left( \Gamma_\phi \frac{\partial \phi}{\partial x_i} \right) n_i dA = \sum_c \Gamma_\phi n_{ci} \delta A_c \left( \frac{\partial \phi}{\partial x_i} \right)_c. \quad 2.65$$

For the determination of diffusive fluxes, the normal derivative of the variable  $\phi$  at the surfaces of the control volume is needed. The simplest approximation of diffusive flux is obtained considering that  $\phi$  is a linear function between the point P and E (Figure 5):

$$\left( \frac{\partial \phi}{\partial x} \right)_e \approx \frac{\phi_E - \phi_P}{x_E - x_P} \quad 2.66$$

### 2.3.1.3 Discretization of the Source Term

The source term can be divided into a constant term  $S_{\phi,c}$  and a linear variable dependent term  $S_{\phi,L}$ :

$$(S_\phi)_p = (S_{\phi,c} + S_{\phi,L} \cdot \varphi)_p \quad 2.67$$

Here, the indices  $p$  means that the value of the variable  $\phi$  in the center of the control volume represents the values over the entire control volume. The volume integral of the source term can also be approximated using the cell-centered approach:

$$\int_V S_\phi dV = (S_\phi)_p \delta V \quad 2.68$$

### 2.3.2 Solution of algebraic systems of equations

The discretization process results in a system of linear algebraic equations:

$$A\varphi = b \quad 2.69$$

The solution method for this equation system is an important part of each numerical simulation. The complexity and dimension of this system depends on dimension of the problem, cell number of the grid and discretization method. The solution of the linear algebraic equation system can be obtained by either direct methods (Gauss elimination method, Cholesky method, etc.) or iterative methods (Jacobi method, Gauss-Seidel method, etc.). Direct methods demand a large amount of computer memory [112,121]. Iterative methods are based on the multiple application of a relatively simple algorithm. Conventional iterative algorithm converge slower with increasing number of grid nodes [113]. In many commercial CFD program multigrid approach is applied to reduce the number of iterations and the CPU-time required to reach a converged solution [117]. Details to the principle of the mentioned methods are beyond the scope of this work and can be found in number of textbooks [112,113,115,122] .

## 2.4 Numerical Tools

### 2.4.1 DETCHEM Code

The DETCHEM (DETAILED CHEMistry) software package is a numerical tool used for a detailed description of physical and chemical processes of a reactive system by coupling transport and chemistry. It has been designed for a better understanding of the interactions between transport and chemistry and can assist in reactor and process development and optimization. The DETCHEM software package is written in FORTRAN. Reaction rates and transport coefficients, i.e., binary diffusion coefficients, thermal conductivity, viscosity for each species and bulk phase, are calculated using library routines. Detailed gas-phase and surface reaction mechanisms are considered. In this study, zero-dimension DETCHEM<sup>BATCH</sup> and DETCHEM<sup>CSTR</sup> models are used for the investigation of gas-phase chemistry.

One-dimensional DETCHEM<sup>PACKEDBED</sup> and two-dimensional DETCHEM<sup>CHANNEL</sup> models are used for the evaluation of the proposed reaction mechanisms. Details of each model will be explained in the corresponding chapters, where the models are applied.

#### **2.4.2 ANSYS-FLUENT**

ANSYS FLUENT is a computer program for modeling fluid flow, heat transfer, and chemical reactions in simple to complex geometries. This CFD tool is written in the C computer language and it can be improved by the definition of user defined functions or scalars for any arbitrary numerical problem to enhance the standard features. It supports different types of meshing in 2- and 3-D. In this study, ANSYS-FLUENT is used for the modeling of a metallic honeycomb with sinusoidal-channel and irregular washcoat deposition. It is also used for the estimation of the residence time distribution of the flow inside the cross-flow reactor utilized for investigation of homogenous gas-phase reactions.

### 3 Homogenous Oxidation of Light Alkanes in the Exhaust of Lean-Burn NG Engines<sup>1</sup>

The main objective of this chapter is to investigate the effect of elevated pressure on homogenous reactions and particularly on the formation of intermediates in the exhaust of lean-burn NG engines. The study also attempts to determine the proper exhaust conditions of engines equipped with a turbo charger at which complete oxidation of unburnt hydrocarbons can be reached. For this purpose, the impact of exhaust gas composition at different pressures and temperatures is investigated experimentally. The experimental data are interpreted further with the data obtained numerically using detailed chemical reaction mechanisms.

#### 3.1 Experimental Set-up and Conditions<sup>2</sup>

Kinetic measurements were performed in a counter-flow stainless steel reactor (Figure 9), which is dedicated for experiments at elevated pressure [40,76]. As some experiments were conducted in the presence of SO<sub>2</sub>, all setup parts including the reactor were coated with a sulfur-inert layer (SilcoNert® 2000, SilcoTek). This silicon coating prevents direct contact between the gas species and the stainless steel, hereby averting not only corrosion of the setup parts but also undesired reactions, which might be catalyzed by stainless steel. The used apparatus is designed for catalytic tests over a wide range of temperatures up to 750 °C. As shown in Figure 9, the reactor is made of a coated outer and an inner stainless steel tube with 40 and 25 mm in diameter, respectively. The large reactor diameters prevent the interface of wall and gas-phase chemistry. The inlet gas enters the outer pipe at 180 °C and is consecutively heated up to the adjusted temperature prior to the catalyst position. However, the gas-phase experiments were performed with the empty inner tube. Thus, the reactor involves both tubes with essentially an inconstant temperature profile, as inlet temperature of the gas mixture was kept low to prevent any reaction prior to the reactor inlet. The heating is realized by an electrical heating wire surrounding the outer tube. The gas temperature profile, required for the modeling study of the gas phase reactions, was measured inside the inner tube and back-calculated for the outer one, based on the reactor balance equations. A total gas flow of 20 l.min<sup>-1</sup> was used at pressures of 1, 3, and 5 bar and a temperature range of 450 - 650 °C. Continuous gas analysis was carried out using a MKS Multigas 2030

---

<sup>1</sup> The procedure and results presented in this chapter are taken from [123].

<sup>2</sup> The experimental work presented here were conducted by D. Zengel and P. Lott.

FT-IR spectrometer. The tested gas mixture matrix consisted of various gas compositions, which are typical for lean-burn NG engines, representing either a high methane or a high NO<sub>x</sub> slip (Table 1).

Table 1: Composition of tested gas mixtures (GM), balance in N<sub>2</sub>.

	CH <sub>4</sub> /ppm	C <sub>2</sub> H <sub>6</sub> /ppm	C <sub>3</sub> H <sub>6</sub> /ppm	CO /ppm	NO /ppm	NO <sub>2</sub> /ppm	O <sub>2</sub> /vol. %	H <sub>2</sub> O /vol. %
GM 1	3200	150	25	500	120	30	10	12
GM 2	1000	150	25	700	800	200	10	12

Additional gas mixtures with variation in NO<sub>x</sub> and SO<sub>2</sub> concentrations were also tested. The conversion was determined starting at 650 °C and cooling down stepwise by 50 °C to 450 °C. Note that the adjusted temperature can be reached only close to the controlling thermocouple inside the inner pipe prior to the catalyst position shown in Figure 9.

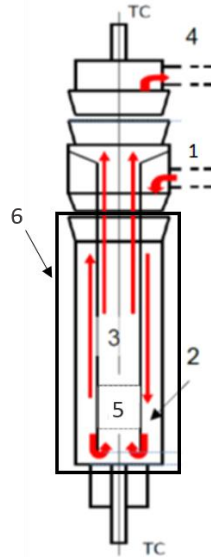


Figure 9: Scheme of the reactor used for gas-phase experiments. 1) Reactor inlet (reactor zone 1), 2) Outer reactor pipe (reactor zone 2), 3) Inner reactor pipe (reactor zone 3), 4) Reactor outlet (reactor zone 4), 5) Position of catalyst in case of activity tests (position of adjusting thermocouple), 6) Heating elements.

### 3.2 Numerical Approach

The effect of pressure on the gas phase reaction was studied numerically using the DETCHEM<sup>BATCH</sup> code [120], which simulates homogeneous gas-phase as well as surface reactions in a batch reactor.

The reaction time corresponds to the mean residence time of stream in the reactor. The residence time is proportional to the pressure according to:

$$\frac{d\tau}{dz} = \frac{1}{u} \quad 3.1$$

$$u = u_s \frac{T}{T_s} \cdot \frac{P_s}{P} \quad 3.2$$

$$\tau = z \frac{1}{u_s} \cdot \frac{P \cdot T_s}{P_s \cdot T} \quad 3.3$$

Where,  $\tau$ ,  $z$  and  $u$  represent residence time, length in axial direction and axial velocity respectively.  $T_s$  and  $P_s$  are temperature and pressure at standard conditions. The time dependent profiles obtained from batch model can be used for a better understanding of the effects of temperature and residence time on the progress of gas-phase reactions. The governing equations for description of a batch reactor are as follows:

Mass conservation for gas-phase species:

$$\frac{dn_i}{dt} = VR_i + A\hat{s}_i, \quad 3.4$$

and the equation of state:

$$P \cdot V = n \cdot R \cdot T. \quad 3.5$$

In the above equations  $R_i$ ,  $\hat{s}_i$ ,  $A$ ,  $V$ ,  $\alpha$  represent the gas phase reaction rate, surface reaction rate, catalytic surface area, reactor volume, and surface relaxation factor, respectively. The amount of species  $i$ ,  $n_i$ , are expressed in terms of mole numbers.

The batch model is further evaluated with a DETCHEM<sup>CSTR</sup> code based on the continuously stirred tank reactor model. A cascade of 12 CSTRs is used for the numerical model of the reactor used in this study. The inlet conditions of the  $n$ th CSRT within the cascade are given by the outlet conditions of  $(n-1)$ th CSTR:

$$\frac{dn_i}{dt} = R_i + \dot{n}_{i,n-1} - \dot{n}_{i,n}, \quad 3.6$$

### 3.2.1 Estimation of Temperature Profile

The gas temperature profile was measured experimentally for an inert gas mixture consisting of 10 vol. % O<sub>2</sub>, 12 vol. % H<sub>2</sub>O in N<sub>2</sub>, inside the inner pipe of the reactor and calculated for the inlet gas over outer tube. Since the reaction progress in the gas-phase at ambient pressure relies on temperature and residence time, the obtained temperature profile over reactor length was transferred to the profile over residence time (Figure 10). According to the extreme lean gas compositions investigated in this

study, the increase in temperature caused by exothermal oxidation reactions can be neglected. The maximum gas temperature is reached at the location of the controlling thermocouple at around 0.25 m length of the inner tube in stream direction. For the numerical calculations, the residence-time-dependent temperature profile was fed to DETCHEM<sup>BATCH</sup> code. Temperature profile used for simulation at 3 and 5 bar are presented in the appendix.

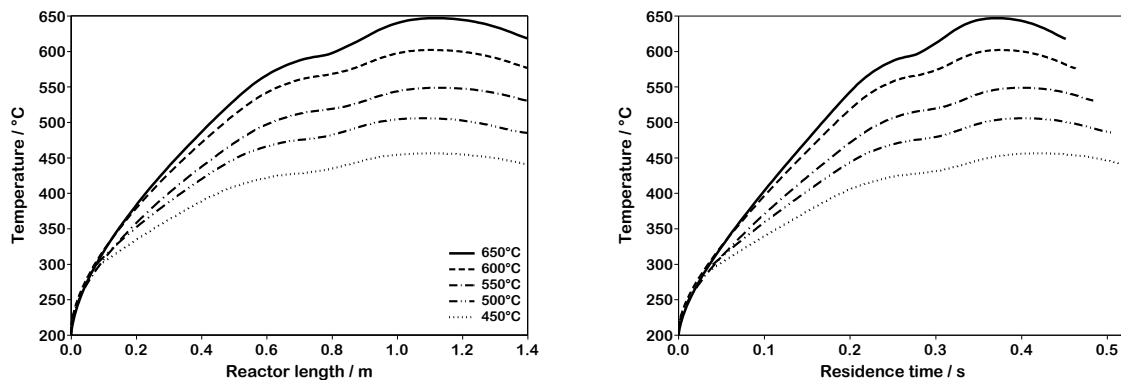


Figure 10: Temperature profile left: vs. reactor length, right: vs. residence time for the adjusted reactor temperature at 1 bar.

### 3.2.2 Reaction Mechanism

For the evaluation and interpretation of experimental results, a reliable reaction mechanism is mandatory. In this study, the detailed gas-phase reaction mechanisms released by *Konnov* (Release 5.0) [124] and *Rasmussen et al.* [86] were used and compared for the applied conditions. The mechanism of *Konnov* describes pyrolysis, ignition, oxidation and detonation of many small hydrocarbons ( $C_{1-4}$ ) as well as nitrogen-containing fuels reacting with different oxidizers over a wide range of conditions typical for combustion processes. The mechanism consists of 1207 reactions among 127 species. The reaction mechanism of *Rasmussen et al.* contains subsets of combustion mechanisms of  $C_{1-2}$  hydrocarbons, NO/NO<sub>2</sub> reactions and interactions between NO<sub>x</sub> and  $C_{1-2}$  hydrocarbons proposed for the temperatures ranging from 500 to 1100 K and pressures from atmospheric to 100 bar. The mechanism consists of 415 reactions among 62 species. Both mechanisms and the applied thermodynamic properties of species have been tested for various applications [19,86,88,93,124–127]. Detailed descriptions and discussions of individual elementary reactions are available in the publication of the authors of the mechanisms.

The main difference between the employed mechanisms lies on the subset of nitro hydrocarbons such as nitromethane ( $CH_3NO_2$ ) and nitroethane ( $C_2H_5NO_2$ ), considered by *Rasmussen et al.*, which conceivably gains importance at high pressure. It is noteworthy to mention that the original version of mechanisms were applied and no adjustment has been made.

### 3.3 Ambient Pressure

The effect of the exhaust temperature on the gas composition was investigated for gas mixture 1 and 2 at ambient pressure and temperature ranging from 450 to 650 °C. The outlet concentration of hydrocarbons as well as the products of partial oxidation reactions, namely CO and to a lesser extent formaldehyde and ethylene, are present (Figure 11). The predicted concentrations present the result of numerical calculations applying the mechanisms of *Konnov* [124] and *Rasmussen et al.* [86] at 1 bar.

The consumption of  $C_3H_6$  and  $C_2H_6$  starts already at 550 °C, where a small amount of formaldehyde has been measured. At 650 °C, the consumption of  $C_3H_6$  is completed and almost 80 % of  $C_2H_6$  is oxidized in both gas mixtures and a considerable amount of formaldehyde and ethylene are produced. Due to a higher methane concentration in gas mixture 1, the outlet concentration of formaldehyde is higher than that of gas mixture 2. The onset of methane oxidation is rather high and a considerable reduction in the initial concentration occurs first at 650 °C. The formation of CO as well as formaldehyde and ethylene are favored with elevated temperature. Further increase in temperature leads conceivably to a reduction of the formaldehyde concentration, as maximum formaldehyde concentrations are reported to peak around 675 °C [19,80], followed by a decline in concentration at higher temperatures. It is also evident from the results that homogenous reactions taking place outside of engines, such as in the exhaust port and manifold as well as in the exhaust pipe, are of particular importance for the design of emission control systems.

The simulation results indicate that both mechanisms are appropriate for modeling of the exhaust under typical lean-burn NG engine conditions. The calculated curves based on the mechanism of *Konnov* show very good agreement with the experimental results for both gas mixtures 1 and 2. At temperatures below 650 °C, the predicted intermediate yields and reactant conversions are rather under-predicted with the mechanism of *Rasmussen et al.* in case of gas mixture 1. The calculated concentrations at 650 °C are accurate for gas mixture 1 and well-predicted for gas mixture 2. It should be mentioned that  $C_3$  hydrocarbons are not involved in the mechanism of *Rasmussen et al.*, which may cause a slight discrepancy predicting the formaldehyde and ethylene concentration since the inlet concentration of  $C_3H_6$  was 25 ppm.

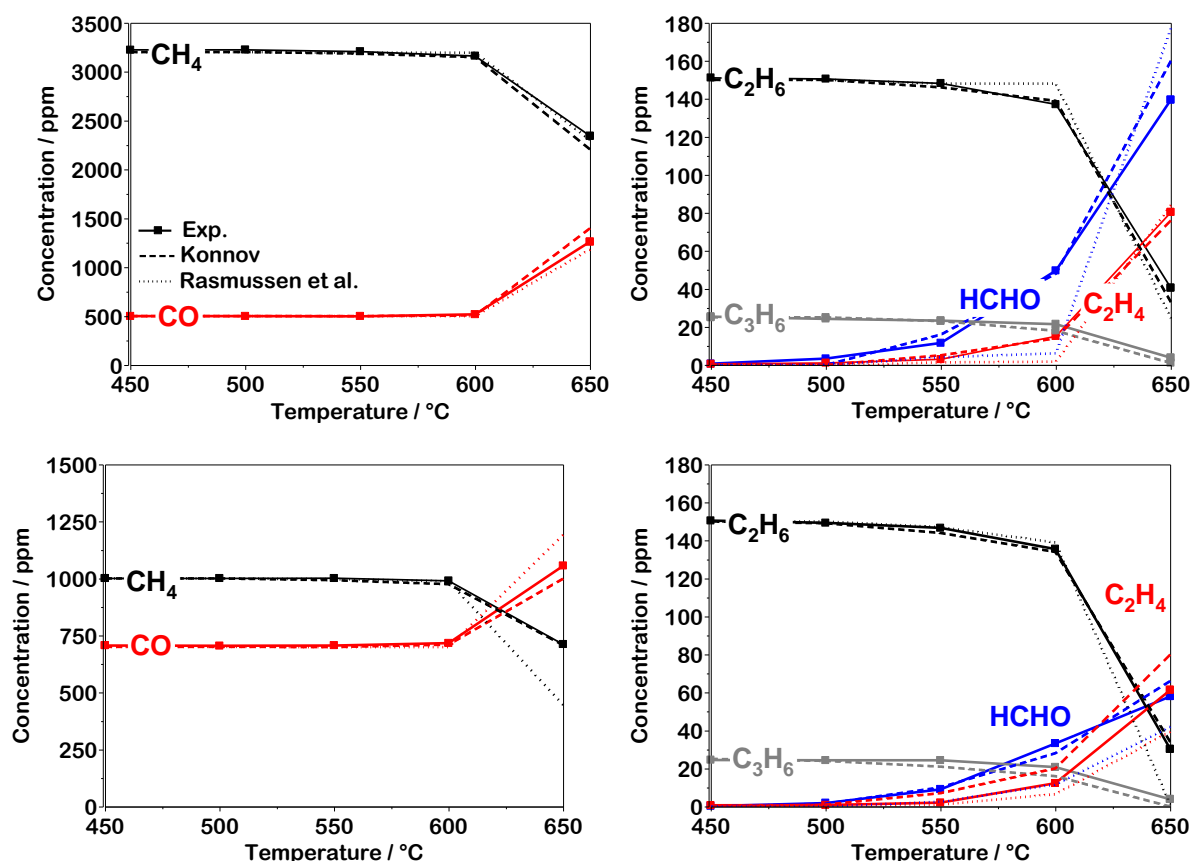


Figure 11: Simulated (dashed lines: with the mechanism of Konnov, dotted lines: with the mechanism of Rasmussen) and measured concentration (solid lines with squares) profiles vs. temperature. *Top*: GM1: 3200 ppm  $\text{CH}_4$ , 500 ppm  $\text{CO}$ , 150 ppm  $\text{C}_2\text{H}_6$ , 25 ppm  $\text{C}_3\text{H}_6$ , 120 ppm  $\text{NO}$ , 30 ppm  $\text{NO}_2$ , 10 vol. %  $\text{O}_2$  and 12 vol. %  $\text{H}_2\text{O}$ . *Bottom*: GM2: 1000 ppm  $\text{CH}_4$ , 700 ppm  $\text{CO}$ , 150 ppm  $\text{C}_2\text{H}_6$ , 25 ppm  $\text{C}_3\text{H}_6$ , 800 ppm  $\text{NO}$ , 200 ppm  $\text{NO}_2$ , 10 vol. %  $\text{O}_2$  and 12 vol. %  $\text{H}_2\text{O}$ , at 1 bar and volume flow of 20 slpm.

### 3.4 Effect of Pressure

The effect of pressure on the conversion of hydrocarbons was examined at 3 and 5 bar for gas mixture 1. Pressure can affect the gas-phase reaction in different ways. In a plug flow reactor with constant mass flow, an increase of pressure causes a longer residence time for the reactants in the reactor. Additionally, the rate of pressure-dependent reactions alter with variation of pressure. Figure 12 demonstrates the experimental results, associated with the respective simulation results by applying the kinetic model of *Konnov*.

Increasing the pressure significantly decreases the initiation temperature and remarkably enhances the methane conversion. Thus, almost complete conversion of methane is achieved at 650 °C and 5 bar, which is a feasible condition upstream of the turbo charger. A similar and more prominent trend is observed for the other hydrocarbons present.

The amount of  $C_3H_6$  and  $C_2H_6$  decreases with an increase in pressure level. The concentrations of  $C_3H_6$  and  $C_2H_6$  start to reduce at 500 °C and 3 bar. 20% of  $C_3H_6$  is oxidized already at 450 °C and 5 bar. The consumption of  $C_3H_6$  and  $C_2H_6$  is completed at 600 and 650 °C, respectively. Figure 12 also shows the oxidation of methane at temperatures as low as 550 °C with a pressure of 5 bar. Consequently, formaldehyde and ethylene formation start at a lower temperature and reach a maximum at 600 °C. The maximum concentration of these species are lower at higher pressures. From 600 °C on, the concentration of both formaldehyde and ethylene decreases with temperature. Formation of CO is also inherently enhanced with pressure at lower temperature. The simulated outlet concentrations represent a good prediction of the experimental results under all tested conditions. There are some discrepancies in predicting the maximum concentration of formaldehyde and ethylene, which are more pronounced at higher pressure. However, both experiments and simulation confirm the enhancing effect of pressure on methane oxidation and the possibility of lowering the maximum formaldehyde concentration.

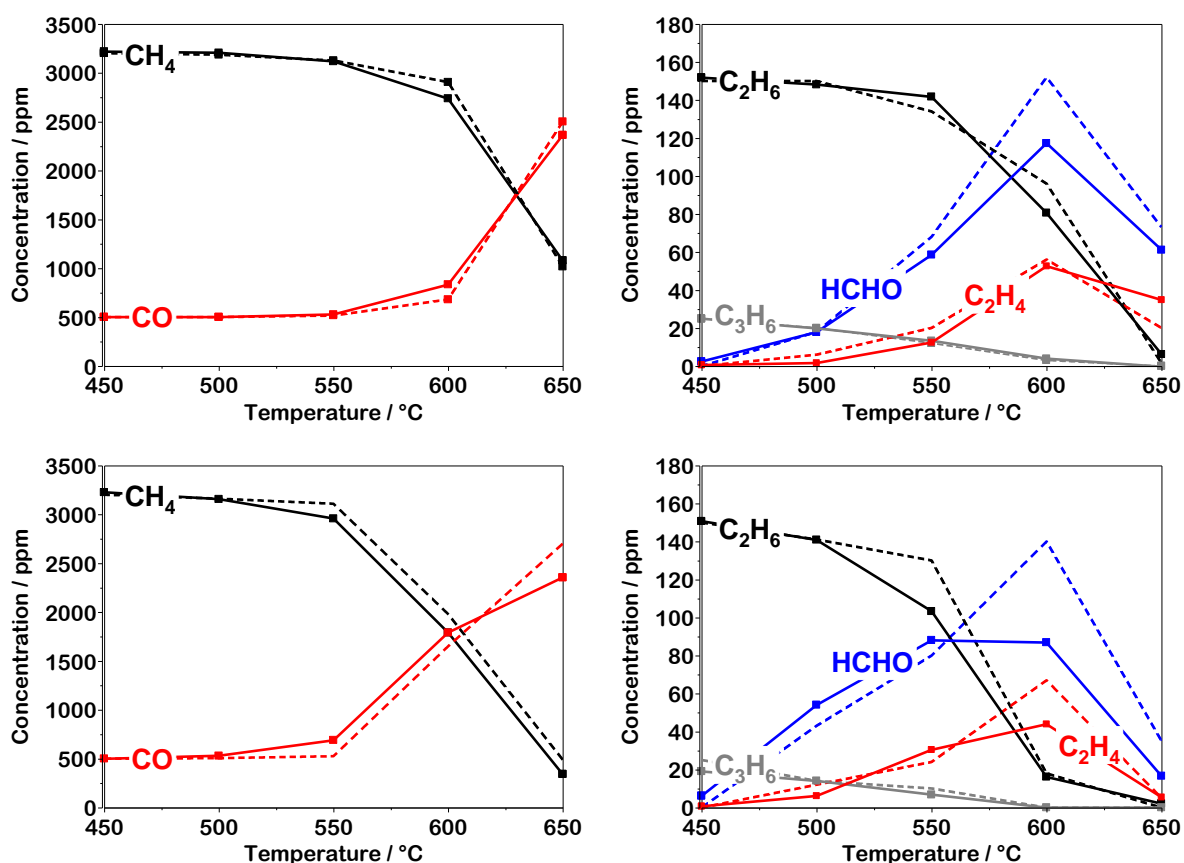


Figure 12: Simulated (dashed lines) and measured (solid lines with squares) concentration profile of hydrocarbons and CO vs. temperature at *top*: 3 bar and *bottom*: 5 bar. Inlet gas composition GM1: 3200 ppm  $CH_4$ , 500 ppm CO, 150 ppm  $C_2H_6$ , 25 ppm  $C_3H_6$ , 120 ppm NO, 30 ppm  $NO_2$ , 10 vol. %  $O_2$  and 12 vol. %  $H_2O$  in  $N_2$ . Mechanism of Konnov was used for calculation of concentration profiles.

To shed a light on the effect of pressure on the progress of oxidation reactions, the modeled concentration profiles along the reactor at 1 and 5 bar are compared. The calculations were performed using both reaction mechanisms for an adjusted reactor temperature of 650 °C and the results are shown in Figure 13. For the sake of clarity, the measured and calculated values at the reactor outlet are summarized in Table 2.

Table 2: Concentration of gas species at reactor outlet determined numerically and experimentally at 1 and 5 bar for adjusted reactor temperature of 650 °C. Inlet gas mixture GM1: 3200 ppm CH<sub>4</sub>, 500 ppm CO, 150 ppm C<sub>2</sub>H<sub>6</sub>, 25 ppm C<sub>3</sub>H<sub>6</sub>, 120 ppm NO, 30 ppm NO<sub>2</sub>, 10 vol. % O<sub>2</sub> and 12 vol. % H<sub>2</sub>O.

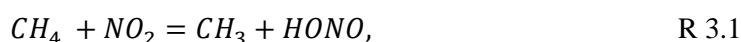
	CH <sub>4</sub>	C <sub>2</sub> H <sub>6</sub>	C <sub>3</sub> H <sub>6</sub>	CO	HCHO	C <sub>2</sub> H <sub>4</sub>	NO	NO <sub>2</sub>
	<i>ppm</i>	<i>ppm</i>	<i>ppm</i>	<i>ppm</i>	<i>ppm</i>	<i>ppm</i>	<i>ppm</i>	<i>ppm</i>
<b>1 bar</b>								
<i>Experiment</i>	2362	41	2	1260	139	80	14	126
<i>Konnov</i>	2205	33	1	1400	160	76	58	83
<i>Rasmussen et al.</i>	2300	24	-	1191	177	83	58	63
<b>5 bar</b>								
<i>Experiment</i>	345	2	0	2353	17	6	5	141
<i>Konnov</i>	490	0	0	2700	35	5	40	108
<i>Rasmussen et al.</i>	1260	5	-	2069	99	41	5	138

Reactant conversions to partial oxidation products generally begin 60 cm after the reactor inlet at 1 bar, where the gas mixture reaches a temperature of 590 °C (Figure 13). Destruction of both formaldehyde and ethylene occurs close to the reactor outlet at around 650 °C.

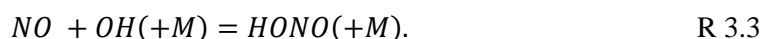
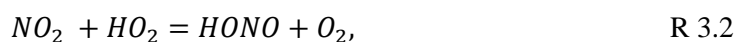
The prediction of formaldehyde and ethylene formation is slightly shifted to farther reactor positions for the mechanism of *Rasmussen et al.*, as propylene oxidation is not considered in the mechanism. However, the concentration profile of ethane and bell-shaped profile of produced hydrocarbons are very well-comparable.

The model prediction of the concentrations of nitrogen-containing species is different considering both mechanisms, as the nitrated hydrocarbons are not included in *Konnov's* mechanism. The experimentally measured NO<sub>x</sub> concentration at the reactor outlet deviates about 10 ppm from the inlet value. The origin of this deviation could not be explained experimentally. The effluent gas mixture modeled by the mechanism of *Rasmussen et al.* contains 25 ppm nitromethane, which, however, does not fit perfectly

to the nitrogen balance. Nitromethane can be formed as a product of the interaction between methoxy radicals and NO<sub>2</sub>. Nitromethane formation is a pressure-dependent reaction (R 1.8), which is favored with increasing pressure at the expense of reduction in concentration of NO<sub>x</sub> [86]. The formation of CH<sub>3</sub>NO<sub>2</sub> is even more pronounced in fuel-rich conditions. However, depending on gas composition and pressure level, the temperature range adequate for the destruction of nitromethane is reported to be lower than 600 °C [86,128]. Therefore, the 7 ppm nitrous acid predicted by the *Konnov* model might be a better explanation for the 10 ppm loss of NO<sub>x</sub> at the reactor outlet. Formation of HONO and its isomers in presence of NO<sub>x</sub> has been widely discussed in literature [86,90,129,130]. HONO can be formed either through interaction of NO<sub>2</sub> and methane via



or as a product of chain-terminating reactions:



HONO is a stable species and decomposes slowly [86,88,89]. When either HONO or CH<sub>3</sub>NO<sub>2</sub> are formed in the mixture they acts as a sink for NO<sub>x</sub> and make the promoting effect of NO<sub>x</sub> less effective. After reaching an equilibrium concentration, they are decomposed by backward reactions (Figure 13).

As seen previously at higher pressures, the initiation temperature is lower, thus the reduction in hydrocarbon concentrations starts at around 500 °C at 40 cm of reactor length. Reduction in methane concentration is more gradual considering the mechanism of *Rasmussen et al.*, and the outlet concentration of methane and byproducts are higher. As expected, decomposition of HCHO and C<sub>2</sub>H<sub>4</sub> occurs earlier at a lower temperature of around 600 °C, predicted with both mechanisms. At the reactor outlet, the nitrogen oxides consist mostly of NO<sub>2</sub>, with more pronounced promoting effect at higher temperatures in comparison with NO [80,89]. According to the prediction of *Rasmussen et al.*, nitromethane is formed as the NO<sub>2</sub> concentration increases, reaching a maximum of 22 ppm and decomposing later on reaching 6 ppm prior to the reactor outlet.

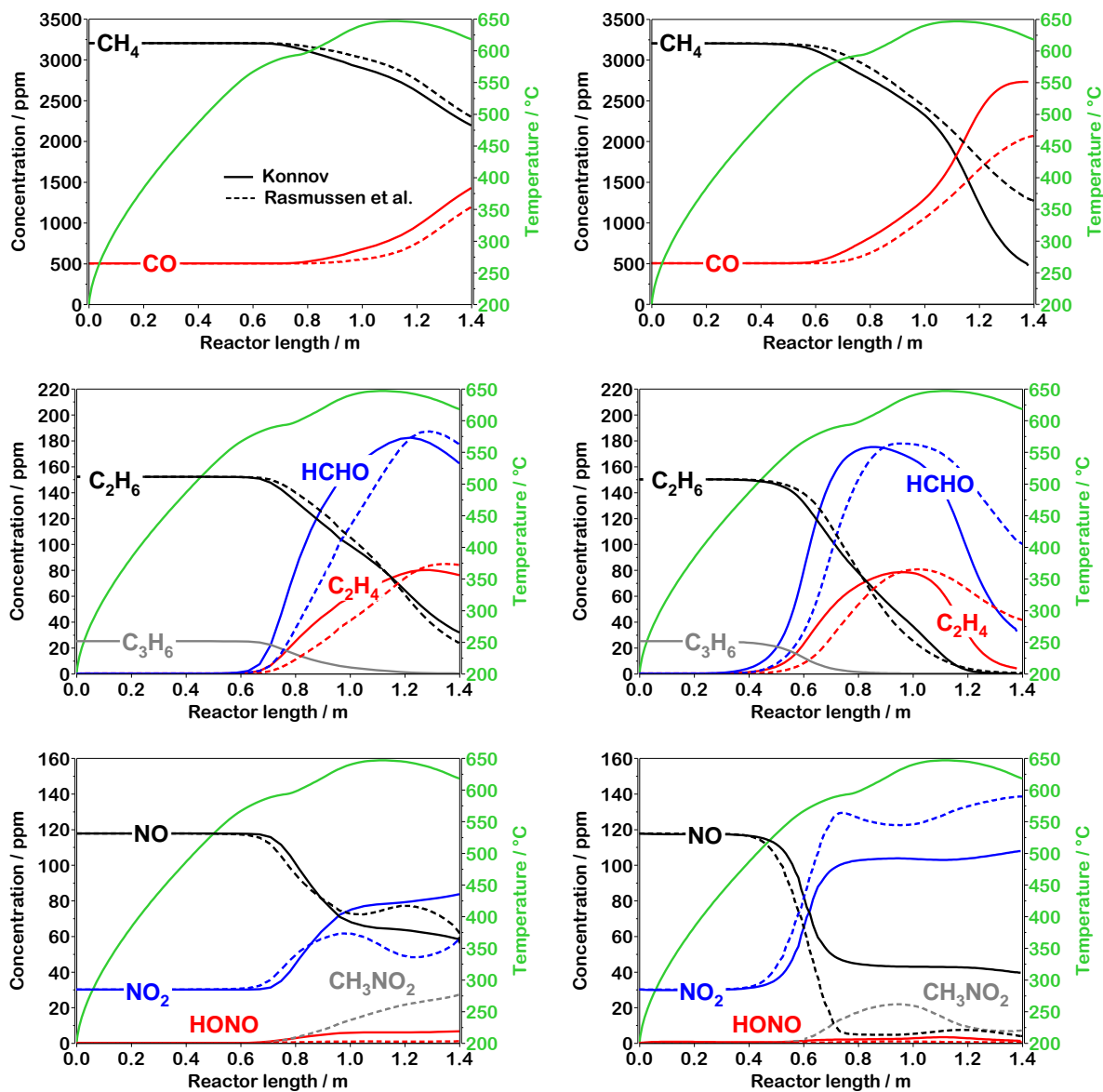


Figure 13: Concentration profile of gas components vs. reactor length simulated with mechanism of *Konnov* (solid lines) and mechanism of *Rasmussen et al.* (dashed lines). Left: 1 bar. Right: 5 bar. Inlet gas composition GM1: 3200 ppm CH<sub>4</sub>, 500 ppm CO, 150 ppm C<sub>2</sub>H<sub>6</sub>, 25 ppm C<sub>3</sub>H<sub>6</sub>, 120 ppm NO, 30 ppm NO<sub>2</sub>, 10 vol. % O<sub>2</sub> and 12 vol. % H<sub>2</sub>O in N<sub>2</sub>.

Since the reaction time in the exhaust is rather short and of milliseconds order, the description of the reaction in its initial stages plays an important role for a reliable modeling study. Figure 14 and Figure 15 illustrate the main pathway of methane consumption after 10 and 200 ms at 5 bar and constant temperature of 650 °C, modeled with the mechanism of *Rasmussen et al.* and *Konnov*, respectively. The flow analysis of reactions at 1 bar (not shown) illustrate similar pathways to 5 bar for both mechanisms. The thickness of arrows represents the percentages of consumption of each species. The reactions with contribution of 1 % or less are not shown. As can be seen in Figure 14 and Figure 15, H-abstraction from methane occurs via interaction with chain-initiating OH radicals in presence of NO<sub>x</sub>. According to

the *Rasmussen* mechanism, consumption of methyl involves four pathways. The formation of formaldehyde precursors, methylperoxyl together with methoxy radicals, through interaction with either  $O_2$  or  $NO_2$  are shown to be the major pathways. The main consumption reaction of formaldehyde does not involve direct interaction with  $NO_x$ , but it is mostly consumed by OH radicals in presence of  $NO_x$ , which has a lower energy barrier than the reaction with  $O_2$  [95]. Almost 6 % of the methyl radicals contribute to the formation of nitromethane over short reaction time. Consumption of  $CH_3NO_2$  happens after reaching the equilibrium concentration [86]. According to Figure 14, destruction of  $CH_2NO_2$  to NO and formaldehyde facilitates  $NO_x$  recycling from nitromethane at short reaction time. But indeed, the backward reaction producing  $CH_3$  and  $NO_2$  dominates the decomposition of  $CH_3NO_2$  at longer reaction times [86,86].

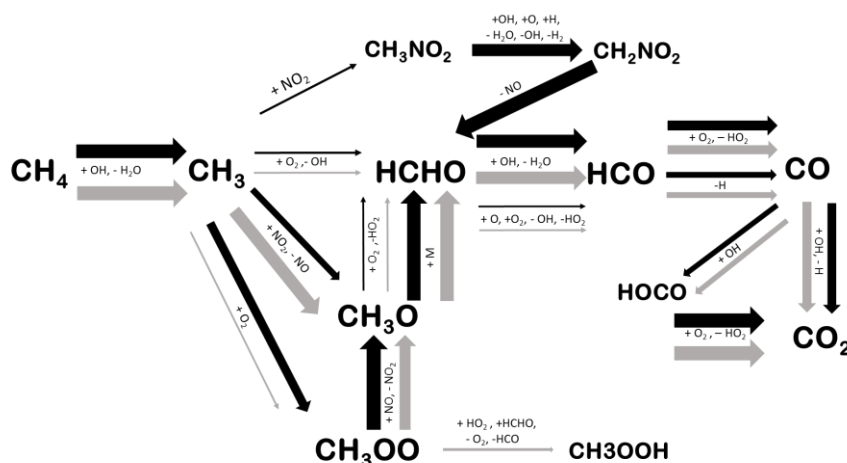


Figure 14: Main reaction pathway of methane oxidation according to the mechanism of Rasmussen et al. Black arrows represent the pathway at 10 ms and gray arrows at 200 ms at constant temperature of 650°C and 5 bar. Inlet gas mixture GM1: 3200 ppm CH<sub>4</sub>, 500 ppm CO, 150 ppm C<sub>2</sub>H<sub>6</sub>, 25 ppm C<sub>3</sub>H<sub>6</sub>, 120 ppm NO, 30 ppm NO<sub>2</sub>, 10 vol. % O<sub>2</sub> and 12 vol. % H<sub>2</sub>O in N<sub>2</sub>.

The oxidation of methane analyzed by the mechanism of *Konnov* appears to have a simpler pathway. Conversion of the methyl radical is here limited to two previously-mentioned main reactions with comparable reaction rates at 10 ms. Beside nitromethane, the formation of methylperoxyl radicals appears to play no substantial role in reaction flow calculated with the *Konnov*'s mechanism.

Increasing the reaction time to 200 ms, the pathways obtained from both mechanisms become more similar. The reaction steps responsible for nitromethane and methylperoxyl radical production almost disappear and methyl radicals are largely consumed by  $NO_2$  to form methoxy radicals.

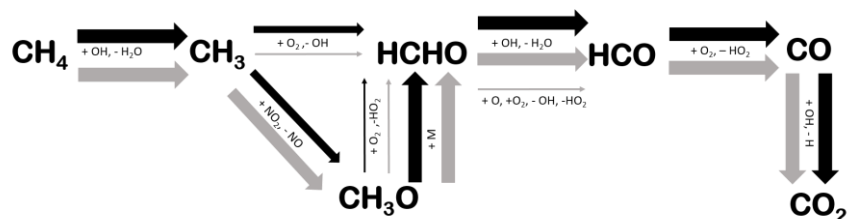


Figure 15: Main reaction pathway of methane oxidation according to the mechanism of Konnov. Black arrows represent the pathway at 10 ms and gray arrows at 200 ms at constant temperature of 650°C and 5 bar. Inlet gas mixture GM1: 3200 ppm CH<sub>4</sub>, 500 ppm CO, 150 ppm C<sub>2</sub>H<sub>6</sub>, 25 ppm C<sub>3</sub>H<sub>6</sub>, 120 ppm NO, 30 ppm NO<sub>2</sub>, 10 vol. % O<sub>2</sub> and 12 vol. % H<sub>2</sub>O in N<sub>2</sub>.

The nitrogen compounds cycle shown in Figure 16 reveals that the concentration of released OH radicals as a product of the disproportionation reaction of NO and NO<sub>2</sub> in the first step is limited by a side reaction between nitrogen oxides and CH<sub>3</sub>O<sub>2</sub>/CH<sub>3</sub>O radicals, according to *Rasmussen et al.* However, this reaction is considered to play an important role in oxidation of NO to NO<sub>2</sub> at initial stages [96]. Hence, the absence of this reaction may cause an incorrect prediction of NO<sub>x</sub> composition at very short reaction times. As seen previously, this reaction is of minor importance at longer residence time, when NO<sub>2</sub> is the dominating nitrogen oxide. On the other hand, the formation of HONO is enhanced at longer residence time considering the mechanism of *Konnov*. Reaction of HONO with OH radicals contributes to NO formation. The cycle of nitrogen-containing species clearly shows that nitrogen oxides play the role of a homogenous catalyst and can be recycled through various reactions.

The aforementioned differences in mechanisms lead to a prediction of different nitrogen-containing species at the reactor outlet and slightly different concentration profiles along the reactor. Nevertheless, the comparison of modeling results reveals that despite differences in the description of the reaction mechanisms, mechanisms extracted from literature are able to give good prediction of oxidation reactions under the condition studied here.



For nonideal reactors, the distinction of an appropriate model requires a comprehensive knowledge of residence time distribution (RTD) as characteristic of nonideal reactors. RTD can be either measured experimentally or calculated numerically by recording the response of a pulse or step signal at the reactor outlet. For the reactor used in this study a CFD simulation is performed for determination of RTD function. Firstly, the developed axial-velocity profile (Figure 17) in both reactor pipes is shown to be laminar for all conditions with a Reynolds number ranging between 250 and 1500.

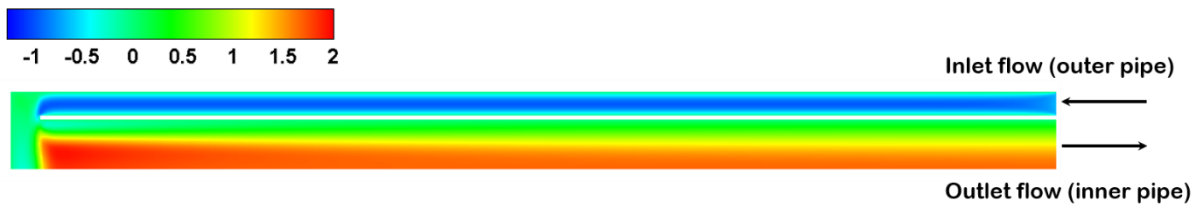


Figure 17: Axial-velocity ( $\text{m s}^{-1}$ ) profile inside the reactor for a volume flow of  $20 \text{ l min}^{-1}$  at standard conditions. Due to symmetrical geometry in axial direction only one half of the entire reactor is modeled.

Secondly, transient calculations of flow field were performed, which involved a pulse injection of a tracer into the reactor inlet (Figure 18). The tracer concentration is recorded afterwards at the reactor outlet as function of time.



Figure 18: Concentration of tracer injected to outer reactor pipe. Due to symmetrical geometry in axial direction only one half of the entire reactor is modeled.

Figure 19 shows the normalized RTD as function of dimensionless residence time which was calculated based on the *Levenspiel* method [104]. The asymmetric shape of the RTD indicates that the flow inside reactor deviates from an ideal plug flow. The early peak is an indication of stagnant flow as can be expected from the axial velocity profile shown in Figure 17 for the flow prior to the inner pipe inlet.

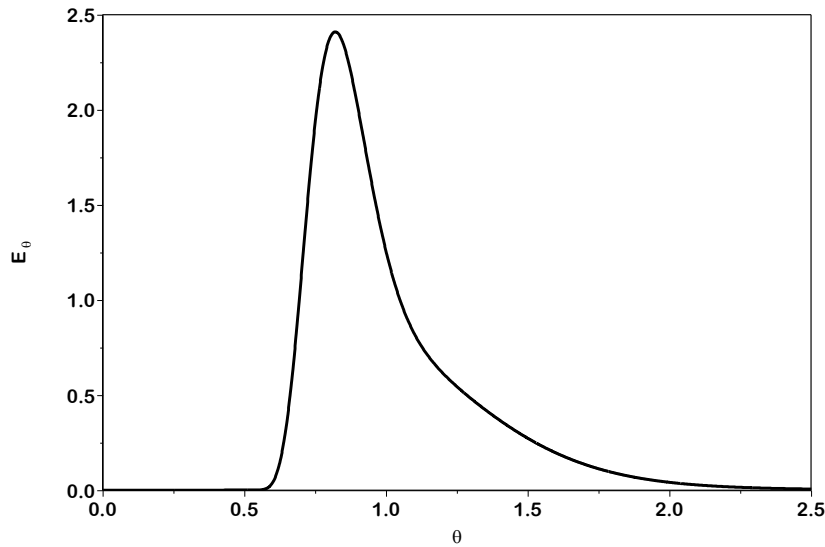


Figure 19: Normalized RTD of tracer.  $\theta = \frac{t}{\tau}$ ,  $t$  = residence time,  $\tau$  = mean residence time

One approach, which can help to find a model, fits the best to the RTD function is a series of continuous stirred tank reactors (CSTR-cascade). The number of tanks can be determined by calculating the dimensionless variance,  $\sigma_\theta$ , for the tracer response curve according to Eq.3.7-3.9.

$$\sigma^2 = \frac{\int_0^\infty t^2 C dt}{\int_0^\infty C dt} - \tau^2 \quad 3.7$$

$$\sigma_\theta^2 = \frac{\sigma^2}{\tau^2} \quad 3.8$$

$$n = \frac{1}{\sigma_\theta^2} \quad 3.9$$

In the above equations  $t$  represents time,  $C$  is the tracer concentration,  $\tau$  is the mean residence time, and  $\sigma$  is the variance of the spread of injected tracer curve. The number of tanks ( $n$ ) necessary to model the reactor, used for this study was estimated to be 12. It should be noted that for these calculations isothermal conditions were implied since CSTR-cascade model is only applicable for identically sized tanks with identical residence time.

Figure 20 demonstrates the concentration profiles calculated with batch and CSTR-cascade models at the highest experimental temperature of 650 °C and at 550 °C. Depending on the pressure and gas mixture, these temperatures were observed to initiate methane oxidation during the experiments at 1 bar. At 650 °C the concentration profile of the most gas components are very well comparable. Only the

consumption rates of CH<sub>4</sub>, CO and HCHO are shown to be higher to some extent when applying the batch model. At 550 °C this deviation is disappearing for CH<sub>4</sub> and CO. The concentration profiles of other species are also in good agreement. It should be mentioned that results of pressure of 5 bar (Figure 2 in the appendix) illustrate the same trend for different species at each temperature.

It is evident from the results presented here that the application of a batch model shows some discrepancies compared to CSTR-cascade model. However, the qualitative interpretation of the simulation results does not change and it still allows to infer the impact of temperature and pressure on the oxidation reactions relevant for this study. Considering the deviation of real exhaust condition from ideal plug flow, the simplified calculation of residence time can also be used for estimation of chemical composition of the exhaust gas in the real applications.

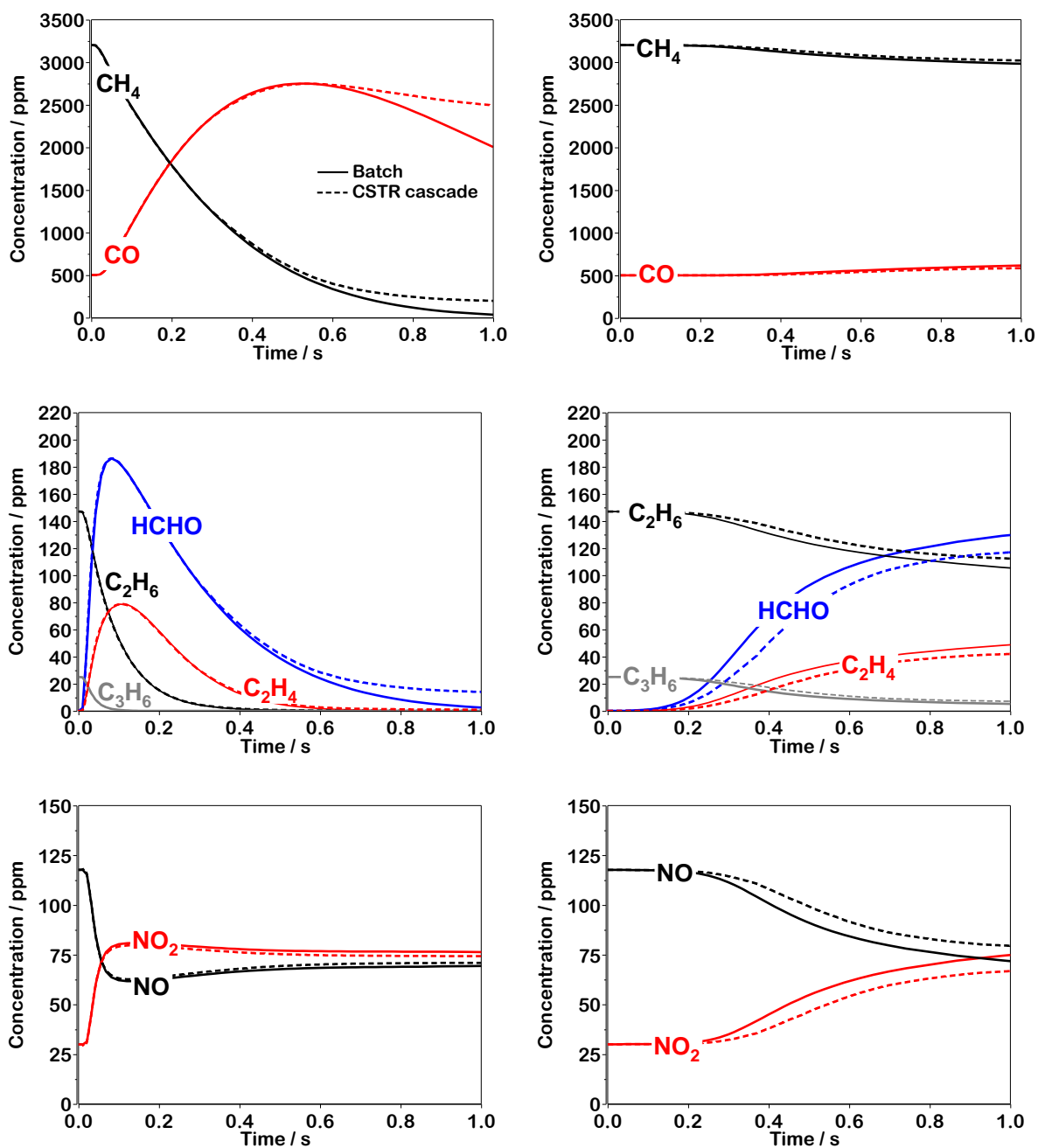
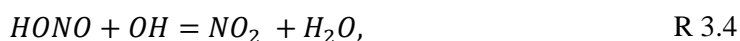


Figure 20: Concentration profile of gas components vs. reaction time simulated with the mechanism of Konnov with a batch (solid lines) and a CSTR-cascade (dashed lines) model. *Left:* 650°C. *Right:* 550°C. Inlet gas composition GM1: 3200 ppm CH<sub>4</sub>, 500 ppm CO, 150 ppm C<sub>2</sub>H<sub>6</sub>, 25 ppm C<sub>3</sub>H<sub>6</sub>, 120 ppm NO, 30 ppm NO<sub>2</sub>, 10 vol. % O<sub>2</sub> and 12 vol. % H<sub>2</sub>O in N<sub>2</sub>.

### 3.6 Effect of NO<sub>x</sub> Concentration

The mechanism discussed in the section above confirms a remarkable influence of NO<sub>x</sub> on the reaction pathway of methane conversion. Moreover, apart from temperature and pressure, hydrocarbon conversion in the exhaust also depends on the composition of the radical pool and the concentration of nitrogen-containing byproducts, which vary based on the NO/NO<sub>2</sub> ratio and NO<sub>x</sub> concentration level. Therefore, various experiments with different gas mixtures at different pressures and temperatures were performed to clarify the role of nitrogen oxides. Figure 21 shows the concentration profiles of the dosed gas species as function of the inlet NO<sub>x</sub> concentration. The inlet NO<sub>x</sub> amount consists of either pure NO or a mixture of NO/NO<sub>2</sub> with a ratio of 4:1. At 1 bar and 650 °C (Figure 21, *top*), no methane conversion could be observed in absence of NO<sub>x</sub>, whereas methane conversion to CO increases with increasing NO<sub>x</sub> concentration, reaching a plateau at 500 ppm NO<sub>x</sub>. Further rise of NO<sub>x</sub> dosage cannot further improve the conversion. Many studies discussed the inhibition due to an excessive amount of NO [80,96,125] by consumption of OH radicals according to R 3.3 and



as present in the flow analysis (Figure 16). The conversion of the other hydrocarbons C<sub>2</sub>H<sub>6</sub> and C<sub>3</sub>H<sub>6</sub> is also positively influenced by the presence of NO, even achieving full conversion if 500 ppm NO<sub>x</sub> or more are dosed. The partial oxidation product formaldehyde as well as the side product C<sub>2</sub>H<sub>4</sub> pass a maximum when 100 ppm NO<sub>x</sub> are dosed at the inlet and stabilize on a plateau at 500 ppm NO<sub>x</sub> inlet concentration, where the NO<sub>2</sub> concentration is also plateaued. Increasing the pressure to 5 bar (Figure 21, *middle*) has a beneficial effect on the conversion of all hydrocarbons, resulting in full conversion of CH<sub>4</sub>, C<sub>2</sub>H<sub>6</sub> and C<sub>3</sub>H<sub>6</sub> and even of HCHO and C<sub>2</sub>H<sub>4</sub> if 500 ppm NO<sub>x</sub> or more are present. Only CO with 1000 ppm is not fully oxidized and therefore still present in a significant amount. This observation is in accordance with a study of *Glarborg et al.* [125], who report that a large amount of NO<sub>x</sub>, particularly NO<sub>2</sub>, inhibits the CO oxidation. This inhibition is attributed to radical removal.

Decreasing the temperature to 550 °C (Figure 21, *bottom*) leads to a lower conversion of all species. However, the beneficial role of NO<sub>x</sub> can clearly be seen as the hydrocarbon conversion continuously increases with increasing NO<sub>x</sub> inlet concentration. At this condition, the outlet NO<sub>x</sub> consists mainly of NO<sub>2</sub> and the outlet NO<sub>x</sub> concentration is less than the inlet one. This difference can be referred to formation of nitrogen-containing species such as nitromethane and nitrous acid at sufficiently low temperature.

Taking all tested conditions into account, high temperature (650 °C) and high pressure (5 bar), as they are common in pre-turbo applications, seem to be sufficient to convert not only ethane and propylene,

but also the most stable hydrocarbon methane. Addition of  $\text{NO}_x$  heavily influences the hydrocarbon conversion in a positive way and even leads to full conversion of methane if 500 ppm are added at 650 °C and 5 bar. Further increase of  $\text{NO}_x$  inlet concentration only has a neglectable effect on the CO conversion, indicating the optimal  $\text{NO}_x$  inlet concentration being ~ 500 ppm under the chosen conditions.

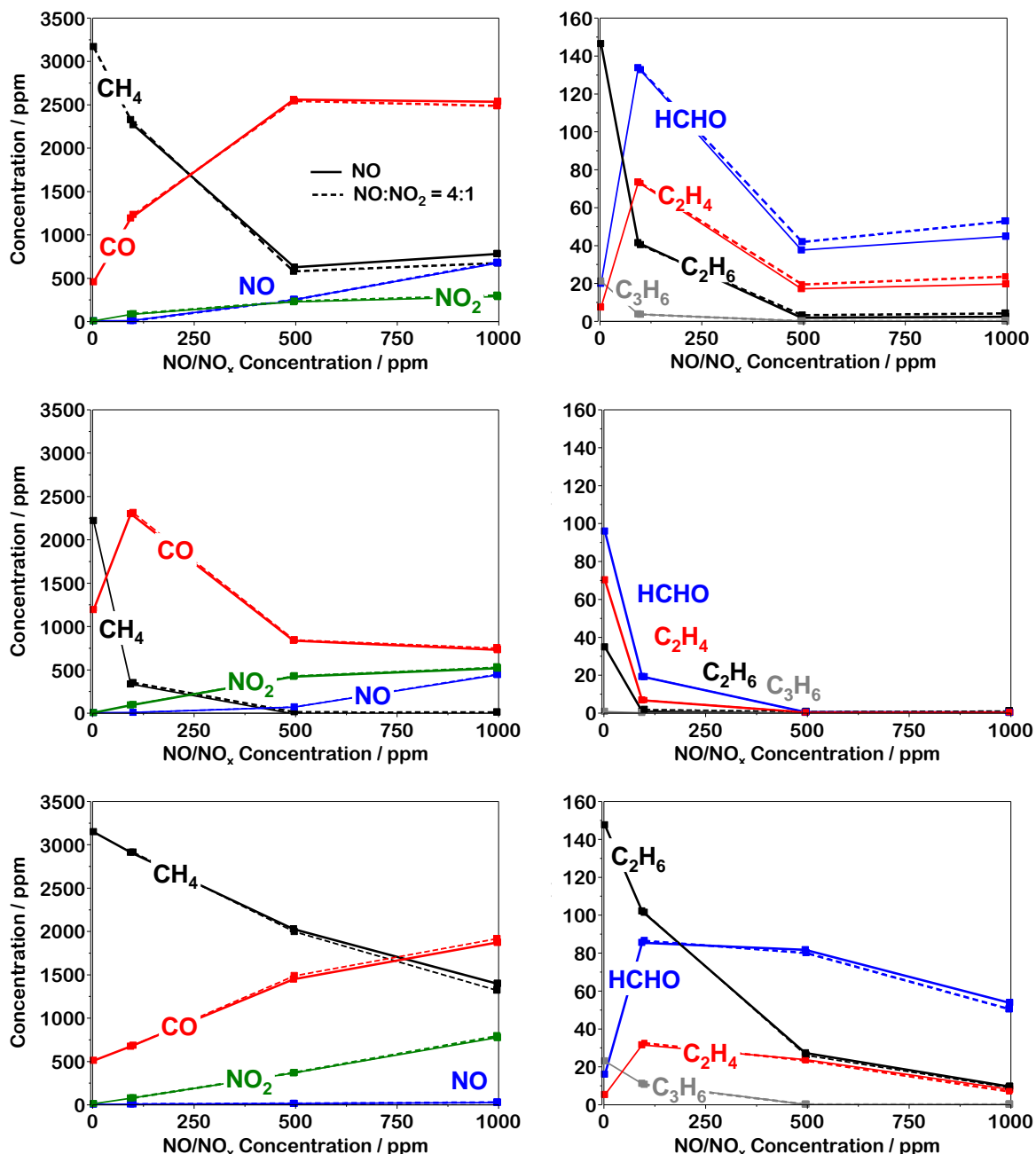


Figure 21: Result of experiments with variation in  $\text{NO}_x$  inlet concentration. *Top*: at 1 bar and 650 °C. *Middle*: at 5 bar and 650 °C. *Bottom*: at 5 bar and 550 °C. The concentration of other gas components were kept the same as GM1: 3200 ppm  $\text{CH}_4$ , 500 ppm  $\text{CO}$ , 150 ppm  $\text{C}_2\text{H}_6$ , 25 ppm  $\text{C}_3\text{H}_6$ , 10 vol. %  $\text{O}_2$  and 12 vol. %  $\text{H}_2\text{O}$  in  $\text{N}_2$ .

### 3.7 Effect of SO<sub>2</sub>

As Figure 22 clearly demonstrates, SO<sub>2</sub>, which is a strong catalyst poison and therefore a major challenge in heterogeneous catalysis [40,43,131], only has a minor effect on the gas phase reaction of methane at 650 °C. At ambient pressure, the presence of SO<sub>2</sub> changes neither the methane nor the carbon monoxide conversion. Addition of NO, on the other hand, increases the methane conversion significantly, likely following the mechanism already discussed above. The presence of 5 ppm SO<sub>2</sub> does not influence the NO<sub>x</sub> sensitized methane oxidation. At elevated pressure (5 bar), methane conversion is slightly higher compared to 1 bar, which is attributed mostly to higher residence time. Furthermore, the addition of SO<sub>2</sub> leads to a slight decrease of methane concentration going along with an increase of CO concentration, indicating an even promotional effect of sulfur dioxide on the conversion in the absence of NO<sub>x</sub>. Possibly SO<sub>2</sub> may act as an oxygen source for the partial oxidation of methane. This promoting effect could not be observed when NO was added to the gas mixture. To conclude, few ppm of SO<sub>2</sub> present in exhaust gas mixtures obviously do not affect the mechanism at all in the presence of NO<sub>x</sub> and therefore do not participate in the reaction. If no NO is dosed, it even plays a beneficial role. In contrast, a pronounced deactivation of methane oxidation catalysts is reported in the presence of SO<sub>2</sub> with time on stream [40]. The Pd-based catalysts suffer from formation of surface and bulk sulfites and sulfates on both, the noble metal and the support [132]. Hence, gas phase oxidation of methane at elevated temperatures and pressures, which are typically relevant in pre-turbo applications, could be a possible route to avoid the negative effects of sulfur compounds as no catalyst might be needed.

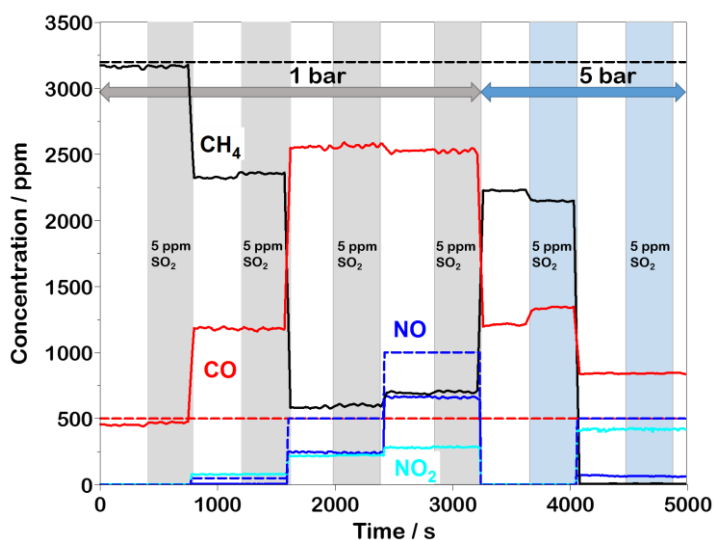


Figure 22: Experimental result of methane oxidation in presence of 5 ppm SO<sub>2</sub>. Inlet (dashed lines) and outlet (solid lines) concentration of CH<sub>4</sub>, CO and NO<sub>x</sub> as function of time at 650 °C for two different pressure (1 and 5 bar). Changes in inlet gas composition according to figure.

### 3.8 Summary

Hydrocarbon emissions of lean-burn NG engines can be controlled by adjusting the pressure and  $\text{NO}_x$  concentration to accelerate the gas-phase reactions responsible for hydrocarbon oxidation. The prolonged residence time only has positive bearing on the desired oxidation in the exhaust of lean-burn NG engines. Oxidation of hydrocarbons can be initiated at temperatures as low as 550 °C resulting from sensitizing effect of  $\text{NO}_x$ . Formation of nitrogen-containing intermediates such as  $\text{CH}_3\text{NO}_2$  or  $\text{HONO}$ , through chain-terminating reaction, and removal of OH radicals is enhanced with a higher amount of  $\text{NO}_x$ , particularly at lower temperatures. Therefore, higher  $\text{NO}_x$  concentration does not necessarily increase the hydrocarbon consumption and also has a drawback on undesirable intermediates.

The partial oxidation of hydrocarbons in the exhaust is a major source of formaldehyde emission. Formaldehyde formation starts at rather low temperature and has a bell-shaped profile vs. temperature. After reaching the maximum concentration, further increase of the exhaust temperature decreases the concentration of formaldehyde.

Results of this study suggest that, at proper reaction conditions, either a smaller amount or even no oxidation catalyst might be required for abatement of methane slip, which could decrease costs and efforts related to catalyst poisoning and deactivation significantly. The amount of formed formaldehyde as product of partial methane oxidation can also be controlled to some extent. The presence of 5 ppm  $\text{SO}_2$  in the gas mixture did not affect the oxidation rate of hydrocarbons in the gas phase, which indicates that the gas phase reaction is not sensitive to the presence of sulfur dioxide under the tested conditions.

The well-predicted concentration profiles, simulated with aid of original mechanisms from literature, indicate that the homogenous reactions can be modeled with reasonable accuracy to find proper exhaust conditions needed for minimized hydrocarbon emissions. The modeling study based on simplified calculation of residence time is shown to be applicable for estimation of the exhaust composition at different conditions.

## 4 Catalytic Oxidation of Methane under Pre-Turbo Conditions<sup>1</sup>

Although Pd-based catalysts provide a high activity for total oxidation of methane [32,33] but they require a high operation temperature ( $>450\text{ }^{\circ}\text{C}$ ) to avoid inhibitions caused by water and sulfur poisoning [34,37–39,134].

For lean-burn turbocharged engines, a solution to this problem is positioning the catalyst upstream of the turbine to take advantage of higher temperatures closer to the engine, resulting in faster kinetics over the catalyst. Pre-turbine placement of the catalyst will also result in higher pressures, depending on engine design and operation point.

Pressure has an effect on residence time and the external mass transfer. An increase in pressure leads to a longer residence time of the exhaust gas stream inside the catalyst (Eq 3.1-3.3), whereas the diffusion coefficient varies inversely with pressure (Eq. 2.56), hence mass transport slows down at higher pressures [135]. Consequently, a pre-turbine catalyst placement can lead to higher conversion levels if the catalytic reaction is rather controlled by kinetics than mass transfer [75–77]. Additionally partial pressure of reactants and consequently the surface concentrations vary with pressure.

In this contribution, the effect of the increased pressure on catalytic oxidation of methane is experimentally investigated for a Pd-Pt-based catalyst at 2 and 4 bar and compared with conventional post-turbine catalyst condition at 1 bar. Based on the experimental results, a mathematical model is developed using a global reaction mechanism to simulate catalytic oxidation of methane over a wide range of temperature and different pressures.

### 4.1 Experimental<sup>2</sup>

#### 4.1.1 Catalyst

For this study, a Pd-Pt model catalyst provided by Heraeus, a technology group headquartered in Hanau, Germany, was used as described in [34]. The washcoat with  $100\text{ g.ft}^{-3}$  ( $3.53\text{ Kg.m}^{-3}$ ) noble metal loading, consisting of Pd and Pt in a weight ratio of 5 to 1 on  $\gamma\text{-Al}_2\text{O}_3$ , was deposited on a cordierite honeycomb

---

<sup>1</sup> Parts of this chapter are taken from [133].

<sup>2</sup> The experimental work was performed by A. Gremminger.

with 400 cpsi (62 cpscm). For activity measurements, cylindrical cores of the honeycomb structure of 3 cm length and a diameter of 2.5 cm were used.

#### **4.1.2 Flow Reactor Experiments**

An in-house made plug-flow reactor setup, explained in section 3.1, was used to measure the catalyst activity as well as reactions in the gas phase. The stainless-steel reactor is coated with a corrosion resistant and inert layer (Silco Tek). Heating was realized by an electrical furnace and temperature was controlled by a Eurotherm 2208 controller with two radially-centered K-type thermocouples placed 3 mm in front and behind the catalyst. Gases were dosed by mass flow controllers (Bronkhorst) via heated lines and water vapor was dosed using a controlled evaporation mixer (CEM, Bronkhorst). Reaction products were analyzed by an FT-IR analyzer (MKS Multigas 2030) [76].

##### **Gas-phase reactions**

Gas-phase experiments were performed to check if pronounced gas phase reactions could occur and interfere with the catalytic reactions. This analysis was carried out using an inert cordierite monolith in place of the coated one. For this test, a gas mixture consisting of 800 ppm CH<sub>4</sub>, 10 % O<sub>2</sub> and 12 % H<sub>2</sub>O diluted with N<sub>2</sub> at 10 slpm ( $1.67 \times 10^{-4} \text{ Nm}^3 \cdot \text{s}^{-1}$ ) was fed into the reactor. Temperature was ramped up with 5 K/min at 1 bar up to 700 °C at which the pressure was increased to 2 and 4 bar, consecutively. Cooling was realized under the same conditions at 4 bar pressure.

##### **Catalytic activity**

##### **Light-off Experiments**

Light-off experiments were performed with two different gas compositions (Table 3) maintaining a constant mass flow and a gas hourly space velocity (GHSV) of 60.000 h<sup>-1</sup>. To investigate the effect of pressure, two consecutive heating and cooling cycles ranging from 200 to 450 °C (up to 600 °C in the case 12 % water are present) with 3 K/min were conducted at 1, 2 and 4 bar representing the pressure at post (1 bar) and pre-turbine (2 and 4 bar) catalyst positioning. Prior to each run of light-offs at certain pressure, the sample was pretreated to preserve a defined state of the catalyst and prevent wrong results due to deactivation effects. The pretreatment consisted of reduction with 2 % H<sub>2</sub> in N<sub>2</sub> at 600 °C, reoxidation in 10 % O<sub>2</sub> in N<sub>2</sub> at 600 °C and consecutive cooling to 200 °C in 10 % O<sub>2</sub> in N<sub>2</sub>. This pretreatment was found to provide reproducible light-off curves.

Table 3: Composition of wet and dry gas mixture for light-off tests

Gas Mixture	CH <sub>4</sub> ppm	O <sub>2</sub> %	H <sub>2</sub> O %	Balance
1	1000	10	-	N <sub>2</sub>
2	1000	10	12	N <sub>2</sub>

### Effect of water

The inhibition of water present in the feed at high concentration (> 1%) has been extensively analyzed at ambient pressure in literature [41,136,137]. On the other hand, in literature, the possibility of inhibition due exclusively to the water produced by the reaction is only assumed without any test aimed at verifying and having an insight into this inhibiting phenomenon. For this reason, in the present work, some tests were carried out specifically to corroborate the results already collected and to strengthen the theory of inhibition caused by water produced by methane oxidation. To simulate the effect of water produced by reaction, water was added to the reaction mixture consisting of 1000 ppm CH<sub>4</sub>, 10 % O<sub>2</sub> in N<sub>2</sub>, in steps of 500 ppm ranging from 0 to 2000 ppm H<sub>2</sub>O while balancing the flow rate with N<sub>2</sub>. These tests were performed at 300 °C and 400 °C at 1 bar with a GHSV of 30.000 h<sup>-1</sup>.

## 4.2 Modeling Approach

### 4.2.1 Reactor Model

The numerical simulations are executed by DETCHEM<sup>CHANNEL</sup> [120]. The single catalytically coated channel is assumed to be an axis symmetric cylinder which results in axial and radial spatial coordinates as independent variables. DETCHEM<sup>CHANNEL</sup> calculates the 2-D steady state concentration and temperature profiles of chemically reacting gas flow through a cylindrical channel using the boundary layer approximation. The boundary-layer method produces accurate results with much lower computational cost than the Navier-Stokes. This assumption is applicable for systems, in which the velocity in flow direction is sufficiently high or the channel diameter is small enough that the diffusive transport along the axial direction is negligible compared to the convective flow [56,68]. These conditions are met for the case studies in this thesis. The boundary-layer approach leads to the following governing equations for a single channel simulation.

Continuity equation:

$$\frac{\partial(\rho u)}{\partial z} + \frac{1}{r} \frac{\partial(r\rho v)}{\partial r} = 0. \quad 4.1$$

Axial momentum:

$$\rho u \frac{\partial u}{\partial z} + \rho v \frac{\partial u}{\partial r} = -\frac{\partial p}{\partial z} + \frac{1}{r} \frac{\partial}{\partial r} \left( \mu r \frac{\partial u}{\partial r} \right). \quad 4.2$$

Radial momentum:

$$\frac{\partial p}{\partial r} = 0. \quad 4.3$$

Species continuity:

$$\rho u \frac{\partial Y_i}{\partial z} + \rho v \frac{\partial Y_i}{\partial r} = -\frac{1}{r} \frac{\partial (r j_{i,r})}{\partial r}. \quad 4.4$$

Where  $j_{i,r}$  is the radial diffusion flux of species  $i$ .

Energy continuity:

$$\rho u \frac{\partial h}{\partial z} + \rho v \frac{\partial h}{\partial r} = u \frac{\partial p}{\partial z} - \frac{1}{r} \frac{\partial (r q_r)}{\partial r}. \quad 4.5$$

#### 4.2.2 Washcoat Model

The detailed washcoat model solves the reaction-diffusion equations in radial direction for every species  $i$  within the washcoat. The species gradients in the washcoat affect the local surface reaction rates  $\dot{s}_i$ . Assuming that the axial concentration gradients are considerably lower compared to the radial gradients leads to the one-dimensional discretization of the washcoat model. Therefore, the reaction-diffusion equation can be calculated with the following expression [56]:

$$\frac{\partial j}{\partial r} - \gamma \dot{s}_i = 0, \quad 4.6$$

where the radial diffusion flux of species  $i$  is calculated by

$$j_i = -D_{i,\text{eff}} \frac{\partial c_i}{\partial r}. \quad 4.7$$

### 4.3 Kinetic Model

The complexity of the kinetics of the catalytic oxidation of methane over bimetallic Pd-Pt catalyst is well-known through several studies [138–140]. Since the catalyst activity is a function of various parameters viz. operation conditions, composition of gas mixture, support material of washcoat, preparation method of catalyst, particle size of the noble metals and even oxidation state of palladium [34–36,141], finding a detailed reaction mechanism including all mentioned parameters is not

straightforward. Thus many authors tried to describe the kinetic of methane oxidation over Pd-Pt catalysts with a global power law reaction rate expression [41,142–144].

The order of the reaction rate with respect to methane is mainly obtained to be one. The impact of oxygen, water and carbon dioxide concentrations present in the gas mixture on the kinetic of methane oxidation are commonly known. In lean burn operation and excess of oxygen, the order of reaction rate with respect to oxygen is zero. The catalyst activity is affected by adsorbed water on the catalyst surface at low to moderate temperatures. Water inhibition is often explained by formation of hydroxyl species at low to moderate temperatures and even at high temperature, depending on the support type [142], which covers the catalyst surface and forms palladium hydroxide from palladium oxide which is the main active site for methane oxidation. This process causes a reversible deactivation during long-term usage [39,145]. It has been shown that only the palladium oxides present in the catalysts are responsible for the lowering of conversion since no water inhibition originates from the interaction with platinum sites [146]. No self-inhibition by addition of water is given by the Pt sites present in the bimetallic catalyst, also at a high concentration of water in the feed. Assuming a negative influence of water, the order of reaction with respect to water is often suggested to be -1 or slightly higher. The inhibition effect of carbon dioxide in comparison with those of water is negligible [142].

For modeling of the chemical reactions, kinetic parameters are required to define the reaction rate of the corresponding reaction. Although kinetic parameters are usually evaluated through Arrhenius analysis using data obtained at differential conditions, light-off curves can provide all the necessary kinetic information such as order of reaction, activation energy, and pre-exponential factor with reasonable accuracy [147].

The activation energy of methane oxidation over Pd reported in literature is usually a function of temperature and water concentration [142–144]. In a dry gas feed as temperature is rising, a reduction in activation energy is observed; adding water to the gas mixture leads to a higher apparent activation energy. In this study, an attempt was made to find an activation energy and rate constant which is valid for dry and wet conditions as well as low and high temperatures.

## **4.4 Results and Discussion**

### **4.4.1 Gas-Phase Reactions**

The result of the gas phase experiment is presented in Figure 23. Temperature, methane conversion, CO concentration and HCHO concentration are represented by red, black, blue and orange lines, respectively. Products of partial oxidation of methane, namely CO and formaldehyde, were observed

starting above 650 °C at 1 bar. However, due to a low extent of total and partial oxidation only approximately 1 % of methane is converted at 700 °C and 1 bar. Raising pressure from 1 to 2 and 4 bar leads to an increase in CH<sub>4</sub> conversion and in the concentrations of CO and HCHO. Highest methane conversion (5 %) is found at highest elevated temperature and pressure. This can be explained by a higher residence time within the reactor due to an increase in pressure while keeping a constant mass flow. The cooling curve at 4 bar shows that the products of partial oxidation can already be observed above 600 °C compared to 650 °C at 1 bar. In Figure 23, one can see that gas phase reactions have a bearing on total methane oxidation only at T > 600 °C. As the catalytic tests were conducted up to a temperature of 600 °C, the outcome does not suffer from any interference caused by reactions in the gas phase. Hence, the methane conversion detected in catalytic tests can be attributed only to the catalyst activity.

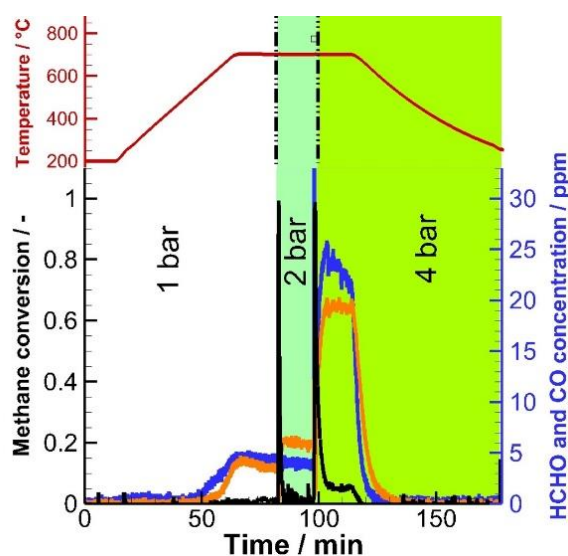


Figure 23: Reactor temperature (red line), CH<sub>4</sub> (black line) conversion, CO (blue line) and HCHO (orange line) concentration of gas phase reaction at 1, 2 and 4 bar. Gas mixture: 800 ppm CH<sub>4</sub>, 10 % O<sub>2</sub> and 12 % H<sub>2</sub>O diluted with N<sub>2</sub> at 10 slpm.

#### 4.4.2 Effect of Pressure

The experimental results of a second run of light-off tests with gas mixture 1 and 2 are depicted in Figure 24. In these cases, the experiments were conducted at three different pressures between 200- 600 °C. The conversion-temperature profile shows the typical S-shape of light-off curves for methane oxidation for both dry and wet feeds. The results show a dramatic drop in catalyst activity in wet conditions (Figure 24, *right*) which leads to a shift of the light-off curve towards a higher temperature in comparison to the light-off curves obtained in a dry feed. In the case of wet feed, methane starts to react at 370 °C, where the conversion in the dry feed has already achieved its maximum and has plateaued for all pressure

levels. The considerable loss of activity due to the presence of additional water in the feed is thoroughly in line with former, previously discussed, studies [34,37–39,134].

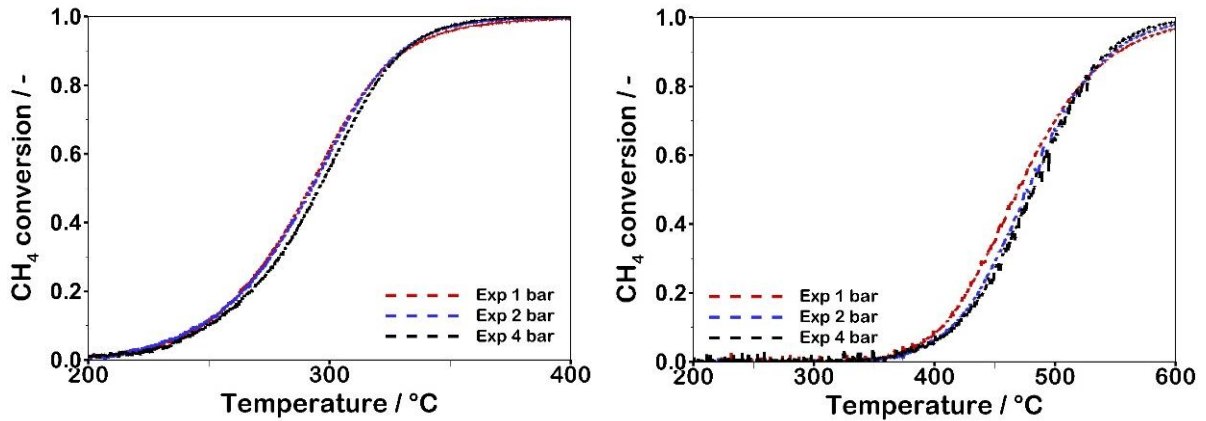


Figure 24: Figure 2: Methane conversion during 2nd heating as a function of temperature at 1, 2 and 4 bar, *left*: with gas mixture 1 and *right*: wit gas mixture 2.

Considering the effect of pressure on the catalyst activity for dry feed, there is no significant change in the conversion of methane during light-off, which is in contrast to the beneficial effect of longer residence time on catalyst activity caused by higher pressure.

Assuming a first order reaction in a plug-flow reactor, an increase in residence time shifts the conversion curve to lower temperatures. For example, at 260 °C, the doubling of the residence time increases the conversion from 17 % to 31 % (see Figure 30). Taking the effect of pressure on mass transport and the diffusion coefficient of species into account, the obtained results might be an evidence of transport-controlled kinetic caused by the limitation in radial diffusion of species into the catalytic surface. Another possible explanation for the performed catalyst activity at higher pressures can also be the inverse reaction rate dependency to the water concentration as pointed out in the literature. Concerning this matter, simulations were done for better analysis of the experimental results.

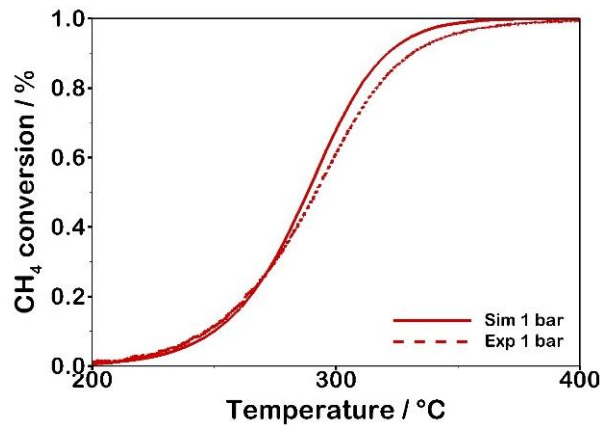


Figure 25: Comparison of experimental (dashed line) and simulated results (solid line) at 1 bar with gas mixture 1. For the 2-D model, the first order reaction rate with respect to methane without inhibition factor (Eq. 14) is applied

Figure 25 shows the experimental and simulated results of the light-off curve for dry feed at 1 bar using the reaction rate expression in Eq. 4.8. The Arrhenius parameters required for the reaction constant were calculated from experimental results of tests under the same condition. An activation energy of 114 kJ.mol<sup>-1</sup> and a pre-exponential factor of 3.01×10<sup>8</sup> m.s<sup>-1</sup> are obtained under a kinetically controlled regime (from 200 to 220 °C).

$$-r_{CH_4} = k_1 C_{CH_4} \quad 4.8$$

In Figure 25, one can see that simulated light-off curves match the experimental one perfectly for a temperature below 300 °C, where the light-off point is not yet reached. For temperatures higher than 300 °C, the model shows higher methane conversion. Applying the same reaction rate expression for 2 and 4 bar results in an overestimation of catalyst activity. In these cases, the simulated results are the same as expected with longer residence time (Figure 26). The higher performance obtained from Eq. 4.8 is not reproducing the real catalyst performance. Nevertheless, it is an indication of a kinetically controlled reaction since higher pressure leads to higher simulated conversion over the whole temperature ranges.

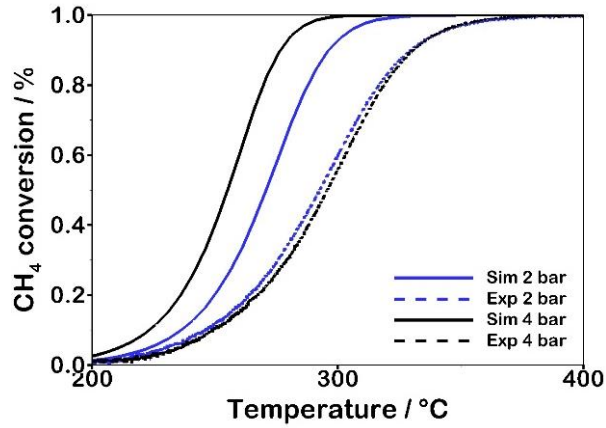


Figure 26: Comparison of experimental (dashed line) and simulated results (solid line) at 1 bar with gas mixture 1. For the 2-D model, the first order reaction rate with respect to methane without inhibition factor (Eq.4.8) is applied

To explain the conversion-pressure trend for the case of dry feed, it is necessary to consider the possibility of an inhibiting effect of the water produced by total oxidation of methane. Thus, an inhibition term (Eq. 4.9) was added to the reaction rate expression and the corresponding parameters have been tuned. The activation energy and the pre-exponential factor were not changed.

$$I = \frac{1}{\left(1 + k_{H_2O,0} \text{Exp}\left(\frac{-\Delta H_{ads}}{RT}\right) C_{H_2O}^\beta\right)} \quad 4.9$$

The order of the inhibition term with respect to the water was set to 1.15, which is higher than the order suggested in the literature [13,22,26]. However, this assumption is consistent with the experimental results. After modifying (Eq. 4.10), the rate constant is decreased for all temperatures depending on the water concentration presence in the gas mixture, as expected.

$$-r_{CH_4} = \frac{k_1 CH_4}{1 + k_2 C_{H_2O}^{1.15}} \quad 4.10$$

The related simulation results are depicted in Figure 27. As shown here, the obtained curves with the implemented model match the experimental data. The inhibition factor added to the reaction rate reduces the catalyst activity at higher temperatures while water concentration produced by methane oxidation increases, especially after reaching the light-off temperature.

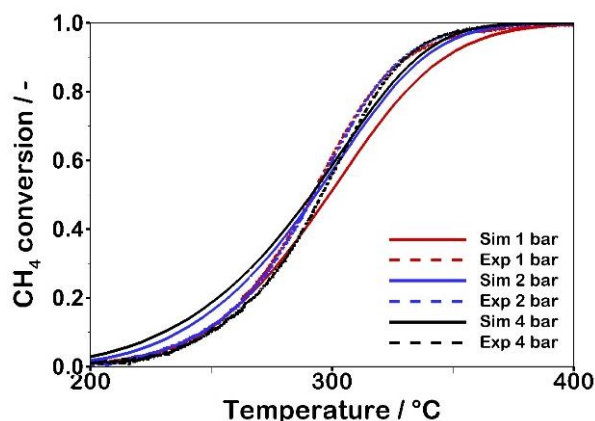


Figure 27: Comparison of experimental (dashed line) and simulated results (solid line) at 1 bar (red lines), 2 bar (blue lines) and 4 bar (black lines) with gas mixture 1. For the 2-D model, the first order reaction rate with respect to methane including an inhibition factor (Eq. 4.10) is applied.

In case of the wet feed, the activity-pressure relation changes in comparison to the dry feed. Figure 24, right exhibits an inversion in the conversion-pressure trend around 525 °C. At lower temperatures than 525 °C, higher pressure leads to lower activity and at temperatures higher than this, an increase in pressure causes an increase in catalyst activity. As mentioned previously, higher pressure determines higher water inhibition, lowering in turn the level of conversion at the same temperature. It must be highlighted that this water inhibition effect is not constant with temperature: At higher temperature, the potentially less active palladium hydroxyl sites are less stable [22,26,27]. Hence, the conversion-pressure trend in the light-off curve could be explained by considering this contribution and weighing the main effects determined by pressure changes. At lower temperatures, the water inhibition prevails over the increasing residence time when pressure increases. Thus, activity becomes lower with the pressure. At higher temperatures, the water inhibition becomes minor and the residence time has the main contribution, bringing about an increase of activity with pressure. To sum up, this change in trend over the temperature range analyzed can be attributed directly to the water effect, getting weaker with temperature increase.

Applying a modified reaction rate Eq. 4.10 in the case of wet feed gives the simulation results depicted in Figure 28. The model is able to simulate the catalyst performance with a reasonable accuracy up to light-off temperature for each investigated pressure. The lower catalyst activity after this point in the experimental results can be attributed to deactivation of the catalyst in the presence of water, which becomes faster with a higher concentration of water. This suggestion is in line with literature [6,28]. It should be pointed out that using one as order of water concentration in the inhibition term, leads to an over estimation of catalyst activity since the negative effect of water can be totally compensated by the effect of longer residence time. Hence, the value of 1.15 enables us to have a better prediction of pressure effects on methane conversion over temperature in both cases of with and without additional water.

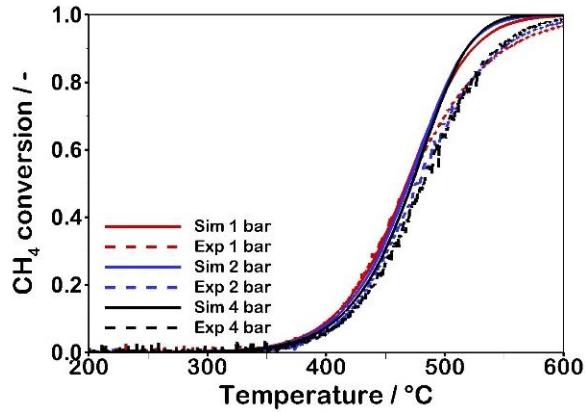


Figure 28: Comparison of experimental (dashed line) and simulated results (solid line) at 1 bar (red lines), 2 bar (blue lines) and 4 bar (black lines) with gas mixture 2. For the 2-D model, the first order reaction rate with respect to methane including inhibition factor (Eq. 15) is applied.

#### 4.4.3 Effect of Water

The light-off tests carried out with dry feed at different pressures showed interesting results that can be explained by taking the inhibition effect caused by the water produced by the reaction into account, of which concentration ranges at very low values.

Many studies have already brought well-established results in the higher percentage water content range [9,14,15], but the effect of only water produced by the oxidation of methane has not been deeply investigated. Therefore, further tests were performed to elucidate this effect.

Figure 29 shows that the addition of water acts as a deterrent to the catalyst activity at 300 °C. In absence of additional water, 70 percent of methane is converted. The conversion level is affected by additional water and is reduced drastically to 45 percent in presence of 2000 ppm water in the inlet feed. Even 500 ppm water in reactor feed causes considerable reduction in catalyst activity. It is worth mentioning that 500 ppm water will be produced by oxidation of methane at 270 °C where 25 % of methane is converted.

Moreover, while at 300 °C the conversion drops as the water concentration is increased, at 400 °C, where there is full conversion, the activity does not decrease. Simulated conversion of methane using a modified rate expression displays the same trend as experiments at 300 °C and matching well with the experimental results at 400 °C.

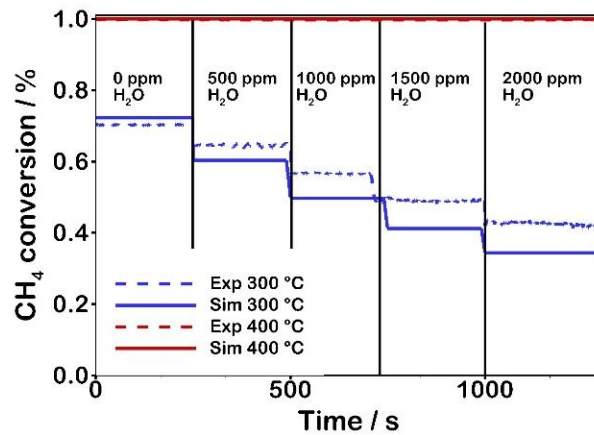


Figure 29: Effect of added water (experimental and simulation) (0 -2000 ppm) to dry feed (1000 ppm CH<sub>4</sub>, 10 % O<sub>2</sub> in N<sub>2</sub>) on methane conversion at 300 °C (blue lines) and 400 °C (red lines) at 1 bar.

## 4.5 Summary

According to the obtained results presented in this study, elevated pressure as a result of pre-turbine placement of the catalyst has two major effects on the catalytic oxidation of methane using the Pd-Pt model catalyst [34]:

- 1) In case of dry feed, no particular change in catalyst activity with pressure is measured. Complete conversion can be reached at low temperature ranges where the inhibiting effect of water produced by methane oxidation is present and hinders the catalyst activity. Thus, the positive effect of longer residence time caused by higher pressure is balanced by inhibition due to water. This observation could be simulated with the proposed model.
- 2) In case of wet feed, besides the shift of the light-off curve to higher temperature compared with dry feed, an inversion in the conversion-pressure trend over temperature is observed. From this inversion point, the positive effect of longer residence time can outweigh the inhibitory effect of water, which gets weaker at higher temperatures. The model was able to reproduce the experimental results with acceptable accuracy.

## 5 Kinetics of Catalytic Oxidation of Formaldehyde<sup>1</sup>

This chapter is dedicated to development of a thermodynamically consistent multi-step detailed surface reaction mechanism for the catalytic oxidation of formaldehyde on platinum-based catalyst. For this purpose, kinetic experiments were performed over Pt-based catalyst under exhaust conditions of lean-burn NG engines. Furthermore, the applicability of the newly proposed reaction kinetics at low temperature was tested on the experimental data of Peng et al. [149], who performed a comprehensive study on the total oxidation of formaldehyde on Pt-TiO<sub>2</sub> catalyst at different operation and preparation conditions.

### 5.1 Experimental<sup>2</sup>

#### 5.1.1 Exhaust Relevant Conditions

The development of the microkinetic model has been supported by two sets of experiments in the temperature range from 120 to 500°C (393-773 K). In the first set, the formaldehyde conversion is measured for powdered Pt-TiO<sub>2</sub> catalyst in a packed-bed reactor, while in the second set of measurements a catalytic coated honeycomb monolith is used as sample in a flow reactor equipped with an in-situ probe technique.

#### Powder catalyst

The model catalyst is prepared by Incipient Wetness Impregnation (IWI). A commercial titania (anatase) carrier containing 10 wt. % silica for higher thermal stability (TiO<sub>2</sub>-SiO<sub>2</sub>, Cristal Global) and as a precursor tetraamminplatin (II)-nitrate (Pt(NH<sub>3</sub>)<sub>4</sub>(NO<sub>3</sub>)<sub>2</sub>, Alfa Aesar) were used. The impregnated catalyst was dried for 8 h at 70° C and then calcined at 700° C for 5 h in the air. The Characteristic of the sample is given in Table 4.

The reactor used for activity measurements of powder catalyst consists of quartz tube filled with 500 mg powdered catalyst. The reactor diameter and packing length were 8 and 10 mm respectively. The detail of the fixed bed reactor, were already described in [109]. The experiments operated with a gas flux of 1.0 standard liter per minute (slpm) at 1 bar. Temperature is ramped up with 5 K/min from 120 °C up to 500 °C (393 - 773 K). The dosage of the gas components (10 vol. %O<sub>2</sub>, 6 vol. %CO<sub>2</sub>, 12 vol. % H<sub>2</sub>O

---

<sup>1</sup> The materials of this chapter are taken from [148].

<sup>2</sup> The experimental works presented in this chapter were performed by T. Schedlbauer and P. Lott.

and N<sub>2</sub>) is controlled by mass flow controllers made by Bronkhorst Hi-Tec. Water is provided by a liquid flow controller from a water reservoir and 80 ppm HCHO is dosed over an in-house-developed saturator [150]. Reaction products are analyzed by an FT-IR analyzer (MKS Multigas 2030).

### **Monolithic catalyst**

For the activity measurement of the monolithic sample, a 400-cpsi cordierite honeycomb with dimensions of 12 mm in length and 19 mm in diameter is used. The slurry for the washcoating is prepared by adding 300 wt. % of distilled water to the calcined powder, described above, and ball-milling it for 1 hour at 400 rpm. The amount of water added is due to the optimal fluidity of the final slurry. The washcoating resulted in a noble metal loading of 0.66 kg.m<sup>-3</sup> (18.7 g.ft<sup>-3</sup>). Firstly, the catalyst is dried at 70 °C for 12 h and then is calcined with a temperature ramp rate of 5 K/min till 600 °C in air and kept at this temperature for 5 hours.

The activity measurement is conducted under isothermal condition and the concentration profiles are recorded inside a single channel of the monolith applying spatial resolved measurement technique. Details of the set-up and sampling method can be find elsewhere [151,152]. The experiment is conducted at gas hourly space velocity (GHSV) of 100000 h<sup>-1</sup> with 80 ppm HCHO, 10 vol % O<sub>2</sub>, 6 vol % CO<sub>2</sub>, 12 vol % H<sub>2</sub>O in N<sub>2</sub>. The gases were preheated up to 90 °C (363 K). The reactor is placed inside a furnace with a fixed temperature of 220 °C (493 K).

### **5.1.2 Indoor Formaldehyde Abatement**

Due to the high activity of platinum for the oxidation of formaldehyde, the full conversion could be accomplished at room temperature depending on the support material, preparation procedure and experimental conditions [42–44,149]. Therefore, Pt-based catalysts were widely discussed and investigated in the literature for removal of formaldehyde from indoor air. For better evaluation of the proposed mechanism, experimental data at low temperature are required. Since water is present in the formalin solution, from which formaldehyde is fed to the gas mixture, dosage of formaldehyde at temperatures lower than the dew point of water could lead to technical problems. Hence, experimental data are extracted from study of Peng et al. [149], in which HCHO<sub>(g)</sub> was produced by heating of the solid para-formaldehyde. The tests were conducted on powdered Pt-TiO<sub>2</sub> catalyst for various formaldehyde concentrations in the feed. The catalyst parameters used in the study of Peng et al. are listed in Table 4.

In these experiments, an isothermal fixed-bed reactor consisting of a quartz tube of 6 mm in diameter filled with 0.25 g catalyst was employed. The catalyst was diluted with quartz wool. The catalyst activity was determined at temperatures ranging from room temperature to 120 °C and at a total flow rate of

1200 ml min<sup>-1</sup>. The concentration of formaldehyde ranges from 75 ppm to 300 ppm in the feed, containing 22 % O<sub>2</sub> balanced with N<sub>2</sub>.

Table 4: characteristic of powder samples

Catalyst	Specific Surface area	Pore volume	Average pore diameter	Dispersion	Pt metal size	Reference
	m <sup>2</sup> .g <sup>-1</sup>	cm <sup>3</sup> .g <sup>-1</sup>	nm	%	nm	
1 wt.% Pt/TiO <sub>2</sub>	104	0.36	14	10	1	This work
0.6 wt.%Pt/TiO <sub>2</sub>	63.8	0.24	11.3	68.5	2.6	Peng et al. [149]

## 5.2 Modeling Approach

The numerical simulation of the flow, mass transport and kinetics in the reactors have been executed by the DETCHEM<sup>TM</sup> software package [120]. For validation of the detailed reaction mechanism and comparison with experimental data fixed bed reactor simulations a performed with DETCHEM<sup>PACKEDBED</sup> code.

### 5.2.1 1-D Packed-Bed Model

The DETCHEM<sup>PACKEDBED</sup> code is designed for a nondispersive one-dimensional flow of a chemically reacting ideal gas mixture. All the axial diffusive terms are neglected by assuming that the velocity in flow direction is sufficiently high, that the diffusive transport along the axial direction is negligible compared to the convective flow. All the radial variations are neglected by assuming that diffusive transport (mixing) is fast in the radial direction. The input parameters were taken from experimental tests and catalyst sample. The one-dimensional isothermal fixed-bed reactor model is based on the following set of equations:

Continuity equation

$$\frac{d(\rho u)}{dz} = a_v \sum_{i=1}^{N_g} \dot{s}_i M_i. \quad 5.1$$

Species conservation

$$\rho u \frac{d(Y_i)}{dz} + Y_i a_v \sum_{i=1}^{N_g} \dot{s}_i M_i = M_i (a_v \dot{s}_i + \dot{\omega}_i \varepsilon). \quad 5.2$$

Conservation of energy

$$\rho u A_c \frac{d(c_p T)}{dz} + \sum_{i=1}^{N_g} \dot{\omega}_i h_i M_i \varepsilon + \sum_{i=1}^{N_g+N_s} \dot{s}_i h_i M_i a_v = \frac{4}{d_h} U (T_w - T). \quad 5.3$$

and equation of state

$$p \cdot M = \rho \cdot R \cdot T. \quad 5.4$$

The area to volume ratio used in the fixed bed model, ( $a_v$ ) is calculated with the following expressions:

$$A_{cat} = D_{Pt} \cdot \frac{m_{Pt}}{M_{Pt}} \cdot \frac{1}{\Gamma}. \quad 5.5$$

$$a_v = \frac{A_{cat}}{V_{bed}}. \quad 5.6$$

For the calculation of catalytic surface ( $A_{cat}$ ), platinum dispersion,  $D_{Pt}$ , of 10 and 69 % were used. The surface-site density value  $\Gamma = 2.72 \cdot 10^{-5} \text{ mol} \cdot \text{m}^{-2}$  is taken from the literature [153]. In Eq. 5.5,  $M_{Pt}$  represents the molar mass of platinum ( $191.7 \text{ g} \cdot \text{mol}^{-1}$ ) and  $m_{Pt}$  is the net weight in % Pt (g). In Eq. 5.6,  $V_{bed}$  is the total volume of the catalytic bed ( $\text{m}^3$ ).

The numerical simulations for modeling study of monolith sample are executed by DETCHEM<sup>CHANNEL</sup>, described in section 4.2.

The simulation parameters required for the numerical calculations with DETCHEM<sup>CHANNEL</sup> code are presented in Table 5.

Table 5: Catalyst parameter of the monolith sample used for modeling

Parameter	Value	Units
Cells per square inch, CPSI	400	inch <sup>-2</sup>
Washcoat thickness	50	μm
Length of monolith	12	Mm
Diameter of monolith	19	Mm
Pt loading	18.7	g.ft <sup>-3</sup>
Catalytic to geometric surface area	9	-
Mean porosity of washcoat	0.5	-
Tortuosity of washcoat	4	-
Mean pore diameter	10	Nm

### 5.3 Surface Reaction Mechanism

The kinetics of adsorption and decomposition of formaldehyde on Pt has already been in the focus of few studies [46–48,154,155]. The surface reaction pathway of formaldehyde oxidation under lean conditions, has been suggested to proceed via direct decomposition of the adsorbed HCHO to formyl (HCO(s)) and further to CO(s) and H(s) followed by oxidation to CO<sub>2</sub>(s) and H<sub>2</sub>O(s) [154,155]. An alternative oxidation pathway is proposed by other studies [44,46,48]; it involves formation of H<sub>2</sub>COO(s) and formate (HCOO(s)) in the presence of oxygen succeeded by either formyl formation or decomposition to CO<sub>2</sub>(s). The second oxidation pathway is however not supported experimentally and is in contrast to studies, which reported high activation energy (~ 70 kJ mol<sup>-1</sup>) for decomposition of formate on Pt [156,157]. So that decomposition of HCOO expected to be the rate-limiting step, which is in contradiction with low activation energy of formaldehyde oxidation on Pt.

Moreover, the detailed surface mechanisms available from literature are not examined for thermodynamic consistency, which aside from misleading prediction of equilibrium state, can also results in incorrect solution of mass and energy conservation equations [158].

The reaction mechanism proposed in this study consists of 6 gas-phase species (HCHO, O<sub>2</sub>, CO, H<sub>2</sub>, CO<sub>2</sub>, H<sub>2</sub>O), 10 surface intermediates (HCHO(s), C(s), CO(s), CO<sub>2</sub>(s), HCO(s), O(s), H(s), OH(s), H<sub>2</sub>O(s), Pt(s)), and a total of 30 elementary-step based reactions. The mechanism is presented in

Table 6. Therein, Pt(s) denotes a free platinum surface site.

Pre-exponential factors are derived from transition state theory and are within the reasonable range for uni- and bimolecular surface reactions steps [106,159]. The activation energies of all elementary steps

as well as the enthalpies of formation of surface intermediates, and reaction enthalpies have been determined using the UBI-QEP (Unity Bond Index-Quadratic Exponential Potential) method [160,161]. For the verifying of a thermodynamic consistency of mechanism, an iterative adjustment procedure was applied [109], which corrects the kinetic source data ( $E_{a,k}$ ,  $A_k$ , and  $\beta_k$ ), to obtain a set of thermodynamic consistent kinetic parameters.

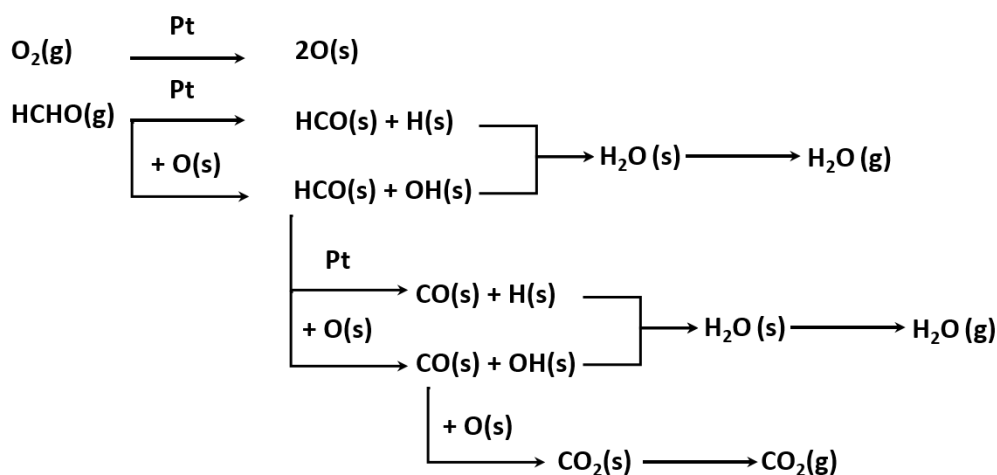


Figure 30: Reaction scheme of formaldehyde oxidation on Pt

The adsorption reactions (R1–R6) of the gas-phase species have been modeled with sticking coefficients. The sticking coefficient of formaldehyde, that adsorbs molecular on Pt, was initially taken as unity [154,155] and afterward corrected to fit the model predictions with experimental results keeping the mechanism thermodynamically consistent. Eisert and Rosén [162] determined the coverage and temperature dependent sticking probabilities of hydrogen and oxygen on Pt(111). STM and HREELS results from Germer and Ho [163] as well as Völkening et al. [164] indicate that hydrogen and oxygen adsorb dissociative on platinum. The sticking coefficients of hydrogen range between 0.001 and 0.5 in literature [162,165–168]. In many publications, the sticking coefficient is 0.046 [169,170]. Hydrogen shows a high mobility on the platinum surface. Therefore, the reaction order can be changed. The sticking coefficients for oxygen are reported between 0.003 and 0.08 [162,169,171–173]. CO adsorbs molecular on platinum. Sticking probabilities, published in literature, are between 0.5 and 0.8 [171,174,175]. The  $CO_2$  adsorption has been studied much less in literature. Gavril et al. [176] observed a small activation energy of  $6 \text{ kJ}\cdot\text{mol}^{-1}$  during  $CO_2$  adsorption via gas chromatography. Zerkle et al. [177] supposed a sticking coefficient of 0.005 during their investigations of ethane oxidation. A sticking probability for the adsorption of  $H_2O$  was identified between 0.5 and 1 from Fisher and Gland [178]. In this work the sticking coefficients required for description of adsorption reactions of  $O_2$ ,  $CO$ ,  $H_2$ ,  $CO_2$  and  $H_2O$  have been taken from [179] and are well comparable with values from literature.

Adsorbed hydrogen and oxygen desorb associatively (R7, R8). The activation energy corresponds approximately to the adsorption heat of the adsorbat bond. At low H(s) coverage, hydrogen desorbs with an activation energy of 63 to 83 kJ.mol<sup>-1</sup> [166,180–182]. The value of 75 kJ.mol<sup>-1</sup> is used in the present study for the activation energy of hydrogen desorption as determined from UBI-QEP method. Due to strong Pt-O-bond, the adsorption heat of oxygen on platinum is relatively high and lies between 209 and 240 kJ.mol<sup>-1</sup> [169,171,183,184]. With increasing oxygen coverage on the catalyst surface, the activation energy decreases significantly [169,171]. The initial value of 213 kJ.mol<sup>-1</sup> used in this work is in good agreement with previous studies.

Desorption of CO occurs molecular with an energy of 134 kJ.mol<sup>-1</sup> (R12). In literature, desorption energy of 100-120 kJ.mol<sup>-1</sup> [185,186] is proposed. However, these publications do not consider coverage dependencies of desorption. CO<sub>2</sub> desorbs relatively easy due to its weak bond energy. The value of 14.9 kJ.mol<sup>-1</sup> lies between activation energies from 5 to 27 kJ.mol<sup>-1</sup> reported by other researches [177,187,188].

The desorption barrier of water observed to be 40 – 65 kJ.mol<sup>-1</sup> and independent of the surface coverage [178,187]. The calculated value of 39.6 kJ.mol<sup>-1</sup> is very close to energy barriers from literature.

The reaction pathways for the oxidation of formaldehyde on Pt is schematically illustrated in Figure 30.

The Langmuir-Hinshelwood reaction scheme assumes two different activation paths of adsorbed formaldehyde. The first pyrolytic path involves the stepwise abstraction of hydrogen from CH<sub>x</sub>O(s) (x = 1 – 2) species on the free platinum sites down to surface carbon monoxide. In absence of O(s) and on the clean Pt(s) decomposition of formaldehyde to CO and H<sub>2</sub> has been reported to be the dominant pathway [47,48,155]. A barrier of 45.6 kJ.mol<sup>-1</sup> for first H abstraction from HCHO (R27) is calculated here and is close to temperature and coverage dependent barrier applied by Mhadeshwar et al. [154].

The second path considers oxygen-assisted formaldehyde activation through pre-adsorbed O(s) accompanied by the production of surface OH(s) species. This reaction path was shown by sensitivity analysis to be especially important in fuel lean mixtures with high oxygen excess. The produced formyl through HCHO + O(s) → HCO(s) + OH(s) is rapidly oxidizes to CO(s) and OH(s) (R25).

Adsorbed CO reacts with adsorbed oxygen atoms on the platinum surface Langmuir-Hinshelwood-like to CO<sub>2</sub> (R21). Activation energies between 80 kJ.mol<sup>-1</sup> and 126 kJ.mol<sup>-1</sup> are observed for this surface oxidation reaction [154,174,189] that decrease with enhancing CO and O coverage on the surface [171]. The reverse reaction CO<sub>2</sub>(s) → CO(s) + O(s) has hardly been studied in literature. Zerkle et al. [177] used an activation energy of 173 kJ.mol<sup>-1</sup> that decreases to 94 kJ.mol<sup>-1</sup> at total oxygen coverage on the platinum surface. In our study, the activation energy for reverse reaction (R22) was calculated from the UBI-QEP method, yielding a barrier of 137 kJ.mol<sup>-1</sup>.

CO(s) may decompose to C(s) and O(s) on the surface (R20) at high temperatures due its high energy barrier, as it was observed during the oxidation of methane [173,179].

Water is formed by the reaction of adsorbed hydroxyl species with H(s). However, Anton and Cardogan [154,190] show two parallel pathways (R15 and R17) for formation of water on Pt. The barrier of formation of water over  $\text{OH(s)} + \text{H(s)} \rightarrow \text{H}_2\text{O(s)}$  varies between 0 and 66  $\text{kJ}\cdot\text{mol}^{-1}$  [153,154,190,191], while the activation of the second path  $2\text{OH(s)} \rightarrow \text{H}_2\text{O(s)}$  is higher and lies between 48 and 100  $\text{kJ}\cdot\text{mol}^{-1}$  [153,178,190], indicating that the first pathway is the dominant path for formation of water in presence of adsorbed hydrogen. The activation energy calculated for R15 and R17 in proposed mechanism are 9 and 100  $\text{kJ}\cdot\text{mol}^{-1}$  respectively.

Table 6: Surface reaction mechanism for HCHO oxidation over platinum (thermodynamic consistent).

Reaction				A (mol, cm, s)	$\beta$ (-)	$E_a$ ( $\text{kJ}\cdot\text{mol}^{-1}$ )
Adsorption/ Desorption						
R1	$\text{H}_2$	+	$2 \text{Pt(s)} \rightarrow 2\text{H(s)}$	$6.45 \times 10^{-02}$	-0.046	0
R2	$\text{O}_2$	+	$2 \text{Pt(s)} \rightarrow 2\text{O(s)}$	$3.54 \times 10^{-02}$	0.001	0
R3	$\text{H}_2\text{O}$	+	$\text{Pt(s)} \rightarrow \text{H}_2\text{O(s)}$	$3.92 \times 10^{-01}$	0.026	0.12
R4	$\text{CO}_2$	+	$\text{Pt(s)} \rightarrow \text{CO}_2\text{(s)}$	$4.05 \times 10^{-03}$	-0.027	0.04
R5	HCHO	+	$\text{Pt(s)} \rightarrow \text{HCHO(s)}$	$9.73 \times 10^{-01}$	0.005	0.03
R6	CO	+	$\text{Pt(s)} \rightarrow \text{CO(s)}$	$7.60 \times 10^{-01}$	0.008	0
R7	$2\text{H(s)}$	$\rightarrow$	$2\text{Pt(s)} + \text{H}_2$	$1.30 \times 10^{+21}$	0.185	75.44
R8	$2\text{O(s)}$	$\rightarrow$	$2\text{Pt(s)} + \text{O}_2$	$2.32 \times 10^{+21}$	-0.002	$213.61 - 90.00 \cdot \theta_{\text{O(s)}}$
R9	$\text{H}_2\text{O(s)}$	$\rightarrow$	$\text{Pt(s)} + \text{H}_2\text{O}$	$8.06 \times 10^{+14}$	-0.106	39.69
R10	$\text{CO}_2\text{(s)}$	$\rightarrow$	$\text{Pt(s)} + \text{CO}_2$	$2.33 \times 10^{+08}$	0.11	14.90
R11	$\text{HCHO(s)}$	$\rightarrow$	$\text{Pt(s)} + \text{HCHO}$	$1.44 \times 10^{+15}$	-0.079	7.16
R12	$\text{CO(s)}$	$\rightarrow$	$\text{Pt(s)} + \text{CO}$	$4.47 \times 10^{+12}$	-0.03	$134.63 - 40.00 \cdot \theta_{\text{CO(s)}}$
Surface Reactions						
R13	$\text{H(s)}$	+	$\text{O(s)} \rightarrow \text{OH(s)} + \text{Pt(s)}$	$2.42 \times 10^{+21}$	-0.095	$85.24 - 45.00 \cdot \theta_{\text{O(s)}}$
R14	$\text{OH(s)}$	+	$\text{Pt(s)} \rightarrow \text{H(s)} + \text{O(s)}$	$6.20 \times 10^{+20}$	0.095	63.70
R15	$\text{H(s)}$	+	$\text{OH(s)} \rightarrow \text{H}_2\text{O(s)} + \text{Pt(s)}$	$5.55 \times 10^{+21}$	-0.1	9.49

R16	H <sub>2</sub> O(s)	+	Pt(s)	→	H(s)	+	OH(s)	$2.70 \times 10^{+21}$	0.1	127.65
R17	2OH(s)			→	H <sub>2</sub> O(s)	+	O(s)	$2.18 \times 10^{+21}$	-0.005	99.99
R18	H <sub>2</sub> O(s)	+	O(s)	→	2OH(s)			$4.14 \times 10^{+21}$	0.005	239.70-45.00·θ <sub>O(s)</sub>
R19	C(s)	+	O(s)	→	CO(s)	+	Pt(s)	$5.20 \times 10^{+21}$	0	0.4
R20	CO(s)	+	Pt(s)	→	C(s)	+	O(s)	$2.50 \times 10^{+21}$	0	226.3-40.00·θ <sub>CO(s)</sub>
R21	CO(s)	+	O(s)	→	CO <sub>2</sub> (s)	+	Pt(s)	$2.33 \times 10^{+20}$	0.11	79.90-45.00·θ <sub>O(s)</sub> - 40.00·θ <sub>CO(s)</sub>
R22	CO <sub>2</sub> (s)	+	Pt(s)	→	CO(s)	+	O(s)	$1.29 \times 10^{+23}$	-0.11	137.178
R23	CO(s)	+	H(s)	→	HCO(s)	+	Pt(s)	$1.11 \times 10^{+20}$	-0.087	150.36-40.00·θ <sub>CO(s)</sub>
R24	HCO(s)	+	Pt(s)	→	CO(s)	+	H(s)	$1.67 \times 10^{+21}$	0.087	0.63
R25	HCO(s)	+	O(s)	→	CO(s)	+	OH(s)	$2.84 \times 10^{+22}$	-0.008	0
R26	CO(s)	+	OH(s)	→	HCO(s)	+	O(s)	$4.82 \times 10^{+20}$	0.008	128.09-40.00·θ <sub>CO(s)</sub>
R27	HCHO(s)	+	Pt(s)	→	HCO(s)	+	H(s)	$4.91 \times 10^{+21}$	0.087	45.63
R28	HCO(s)	+	H(s)	→	HCHO(s)	+	Pt(s)	$2.79 \times 10^{+21}$	-0.087	55.16
R29	HCHO(s)	+	O(s)	→	HCO(s)	+	OH(s)	$9.69 \times 10^{+21}$	-0.008	26.90-45.00·θ <sub>O(s)</sub>
R30	HCO(s)	+	OH(s)	→	HCHO(s)	+	O(s)	$1.41 \times 10^{+21}$	0.008	14.89

## 5.4 Results and Discussions

### 5.4.1 Exhaust Relevant Conditions

The operating conditions and gas compositions in the first set of the experiments have been chosen based on the typical condition in the exhaust of lean-burn NG engines and the results represent the conditions and constraints in the practical applications.

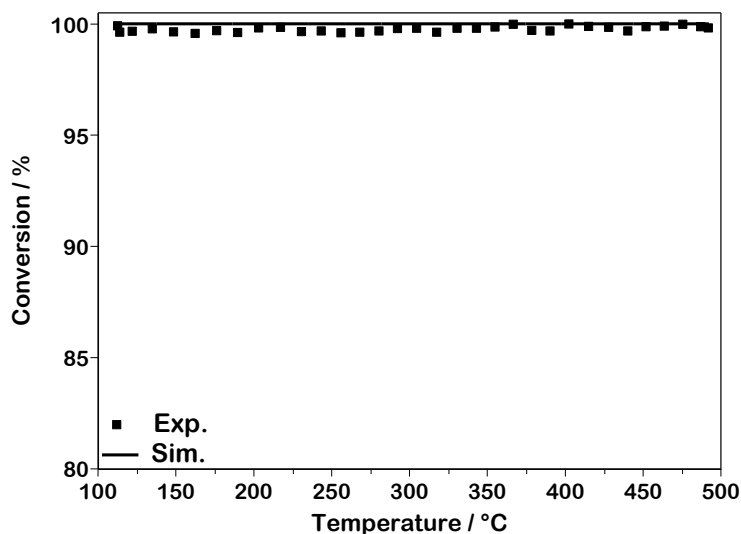


Figure 31: Comparison of experimentally measured (symbols) and computationally predicted (solid line) conversion of formaldehyde as a function of temperature in a fixed-bed reactor; inlet gas composition of 80 ppm HCHO, 10 vol.% O<sub>2</sub>, 12 vol.% H<sub>2</sub>O and 6 vol.% CO<sub>2</sub> in N<sub>2</sub> with the total flow rate of 1 slpm.

The experimentally determined conversion of formaldehyde over powdered Pt sample, shown in Figure 31, confirms the high activity of Pt yielding full conversion of formaldehyde over entire temperature range. The numerically predicted conversion agrees very well with the experimentally derived data. Here the oxygen-rich surface at the operation temperature contributes to the formyl formation and the subsequent formation of CO(s) and H(s) is followed by oxidation to CO<sub>2</sub> and H<sub>2</sub>O as the final products at a very short contact time.

In the case of monolith sample, a central channel was chosen for recording the concentration profiles. In Figure 32 the axial position  $z=0$  mm represents the start of the monolith sample with 12 mm length. Despite the very high intrinsic oxidation rate of HCHO at 220 °C, the catalyst is not able to completely convert all formaldehyde (Figure 32) and the effluent gas mixture contains 8 ppm formaldehyde accounts for 90 % conversion. From Figure 32, it can be seen that the consumption of HCHO is initially fast and 50 % conversion is reached after 2 mm length from the channel inlet. However, the consumption rate is getting gradual from this position on and plateaus over the last 2 mm of the channel length, so that just another 40 % reduction in formaldehyde concentration is achieved over the rest of the channel length (10 mm). From previous studies as well as results of conversion measurements over powdered catalyst, it is known that very low Pt loading is sufficient to accomplish 100 % oxidation of formaldehyde at 220 °C, hence the unexpected low catalyst activity here cannot be related to Pt-loading. Nevertheless, this behavior can be attributed to mass transport limitation since the operation temperature is much higher than the light-off temperature point. Thus, the decline in reactant concentration along the channel length causes a reduction in radial diffusion rate of molecules from channel center to the catalytic surface, which concurrently reduces the overall apparent reaction rate. The transport-limited

kinetics here, prevents full conversion of formaldehyde. This experimental observation is perfectly predicted by the simulation results. The simulation data presented in Figure 32 exhibit the cross-sectional average concentrations for each axial point.

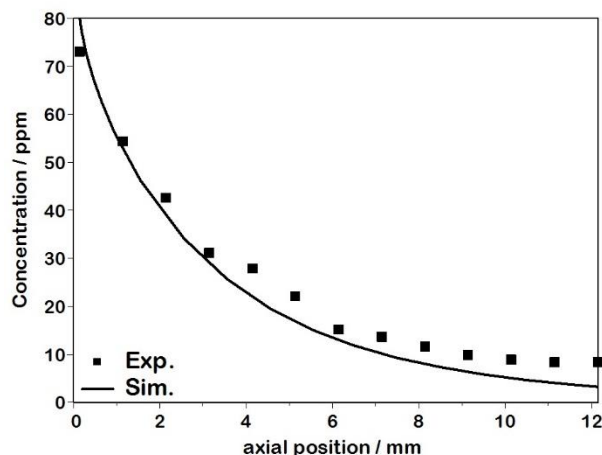


Figure 32: Comparison of spatial concentration profile of formaldehyde determined experimentally (symbols) and computationally predicted cross-sectional average concentration (solid line) as a function of axial position in a channel of 400 cpsi monolith sample at 220 °C. Inlet gas composition: 80 ppm HCHO, 10 vol % O<sub>2</sub>, 12 vol % H<sub>2</sub>O and 6 vol % CO<sub>2</sub> in N<sub>2</sub> and the GHSV of 100.000 h<sup>-1</sup>.

The 2-D concentration profile, depicted in Figure 33, indicates a substantial concentration gradient between channel wall and channel center verifying the assumption of the dominating transport-limitations. Due to the very high reaction rate at the operation temperature, the formaldehyde concentration is nearly zero on the catalytic surface and rather large channel diameter as well as low reactant concentration in the bulk weaken the radial diffusion, which is the only responsible transport phenomena for the mass transfer since the flow inside the channel is laminar. This phenomenon will be discussed in more details in chapter 6.

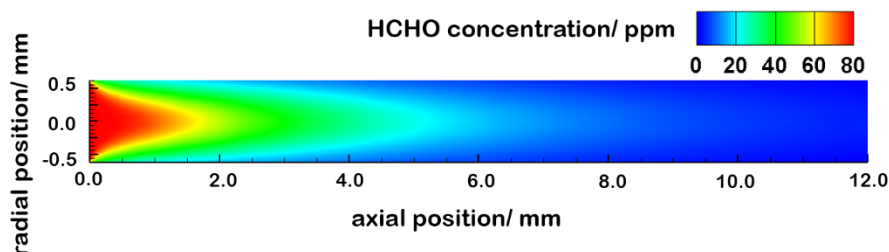


Figure 33: 2-D concentration profile of formaldehyde in a channel of 400 cpsi monolith sample at 220 °C. Inlet GM: 80 ppm HCHO, 10 vol. % O<sub>2</sub>, 12 vol. % H<sub>2</sub>O and 6 vol. % CO<sub>2</sub> in N<sub>2</sub> and the GHSV of 100.000 h<sup>-1</sup>.

### 5.4.2 Indoor Formaldehyde Abatement

Figure 34 shows the comparison of experimentally derived results of formaldehyde conversion with the numerically predicted one as a function of temperature in a fixed bed reactor. The formaldehyde concentration appears to have significant impact on formaldehyde oxidation indicating the higher the concentration the less is the conversion over tested temperature range. Experimental results indicate that, 41% of formaldehyde is oxidized already at room temperature at an inlet formaldehyde concentration of 75 ppm. Accordingly, the conversion declines at higher formaldehyde feed concentrations. In Figure 35, one can see that the shortage of adsorbed oxygen competes with adsorbed OH species. This is the main reason why less formaldehyde is converted at higher inlet concentrations. The mechanism is able to predict the catalyst performance and the decrease in conversion for higher formaldehyde concentrations with reasonable accuracy. The numerically predicted light-off temperature is well comparable with the experimental one for all three concentration levels but from light-off point on, the simulated conversion is higher than the measured one. This deviation can be attributed to mass transport limitations caused by dilution of catalyst with quartz wool. This finding is in agreement with the experimental results presented in the literature [42,44], which show complete conversion of formaldehyde at room temperature and GHSV = 50000 h<sup>-1</sup> on pure (not diluted catalyst) Pt-TiO<sub>2</sub> catalyst. A longer residence time and a homogenous catalyst bed prevent external transport limitations. As expected, a raise in the temperature enhances the formaldehyde oxidation and the complete conversion of formaldehyde obtained experimentally is accomplished for all three concentrations at 90°C. Simulated conversions are completed for all cases at 60°C in absence of transport limitations.

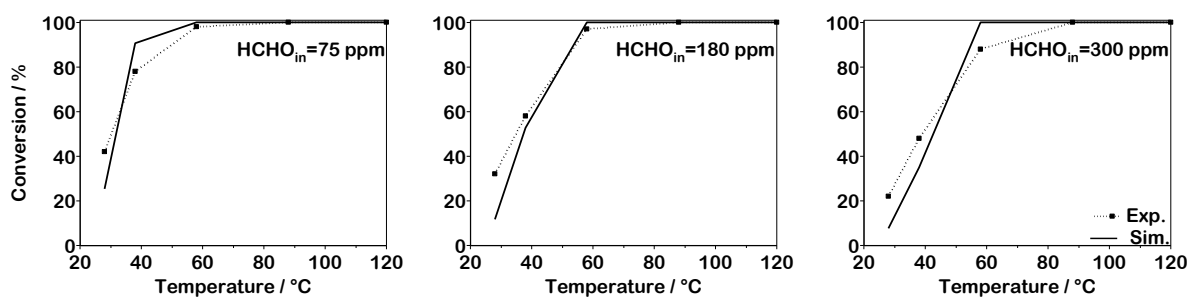


Figure 34: experimental (dashed lines with squares) and simulated (solid lines with squares) conversion of formaldehyde as a function of temperature for 75 ppm (left), 180 ppm (middle) and 300 ppm (right) formaldehyde in the feed.

For better understanding of formaldehyde oxidation on platinum, Figure 35 shows the coverage profiles of surface species at catalyst bed exit over temperature in case of a feed concentration of 180 ppm formaldehyde. Most abundant surface species are O(s), OH(s), CO(s) and Pt(s). In excess of oxygen, adsorbed HCHO species dissociate mostly into HCO(s) and OH(s) followed by oxidation of HCO(s) to CO(s) and OH(s) according to R29 and R25. Thus, below the ignition temperature the surface is mainly

blocked with OH(s) species. With increasing in temperatures, OH(s) and H(s) species react to form water and with the reduction of OH(s) species, adsorbed oxygen becomes the most abundant surface species. Simultaneously, free Pt(s) sites are reduced up to 90°C, where the maximum amount of oxygen is adsorbed on the surface. As increasing temperatures favor higher desorption rates of oxygen, more Pt(s) sites become available.

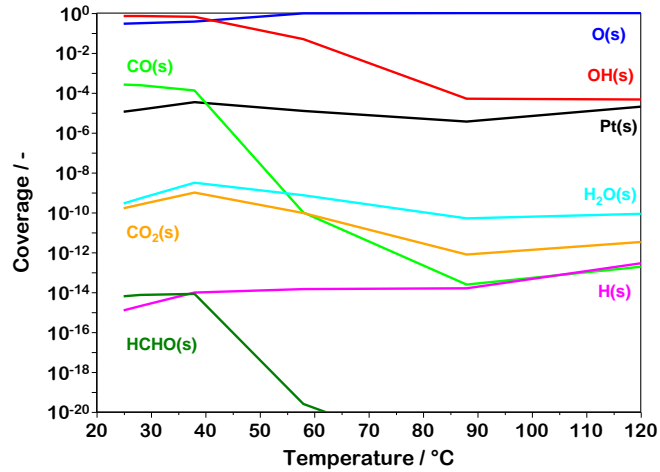


Figure 35: Computed temperature dependent surface coverages (logarithmic scale) on platinum, values taken at the outlet of catalyst bed for formaldehyde concentration of 180 ppm

The comparison of concentration and surface coverage profiles, Figure 36, confirms the inhibiting role of adsorbed OH species on the surface. The initial OH(s) blockage is obvious within first mm of the catalyst bed, where no substantial conversion of formaldehyde takes place. Once dissociation of instable HCO(s) species progresses, the surface is provided with more H(s) species leading to consumption of OH(s) and formation of H<sub>2</sub>O(s). The continuously increasing H<sub>2</sub>O(s) species along the catalyst bed experience a sharp reduction which coincides with diminishing of OH(s) species, while O(s) species become the dominating surface species. Concurrently to the ignition of formaldehyde caused by oxygen-rich surface, the amount of intermediate surface species decrease as no formaldehyde is present anymore in the stream.

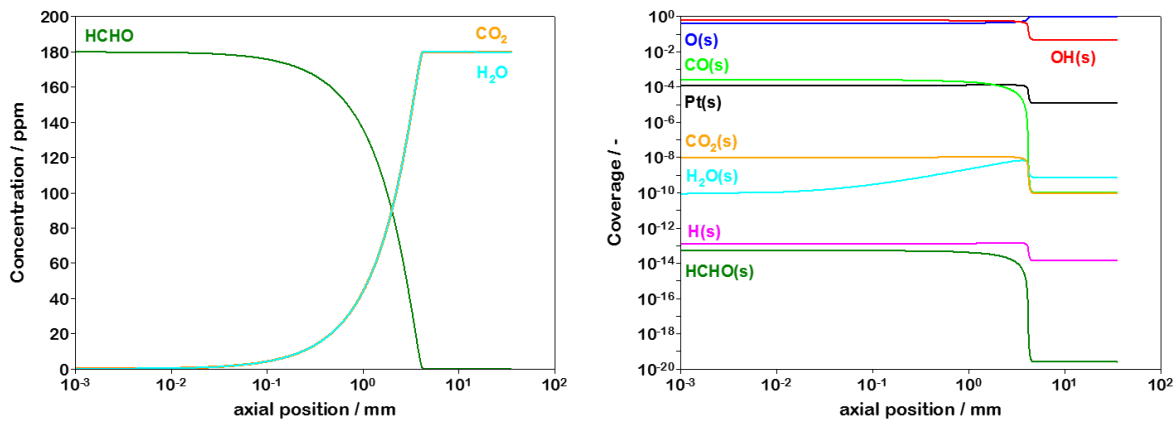


Figure 36: Concentration profile of HCHO, CO<sub>2</sub> and H<sub>2</sub>O (left) and computed surface coverage profiles (right), along the catalytic bed length (logarithmic scale) at 60°C for formaldehyde concentration of 180 ppm.

## 5.5 Summary

A detailed reaction mechanism on the oxidation of formaldehyde over Pt was proposed and validated with experimental results. The Pt-catalyzed oxidation of formaldehyde has shown to have a very low light-off temperature, therefore low Pt-loading is sufficient for complete oxidation of formaldehyde in a packed-bed reactor under typical conditions of exhaust of lean-burn NG engines. The experimental results from literature denoted that the increase in the formaldehyde concentration lowers the oxidation rate up to a certain temperature. This observation could be modeled with the aid of the proposed mechanism here, revealing that the lower reaction rate is a result of blockage of surface with OH(s) and shortage of O(s) up to ignition temperature, at which O(s) becomes the most abundant surface species. In spite of very high intrinsic reaction rate of the formaldehyde oxidation on Pt, complete consumption of formaldehyde was not attained experimentally and the spatially measured concentration profile plateaued over the last 2 mm of the channel length suggesting a transport-limited kinetics more pronounced for lower reactant concentration. The 2-D simulation results revealed that external mass transfer is the rate-limiting step under tested conditions in monolithic sample.

## 6 Formaldehyde Oxidation in Catalytic Sinusoidal-Shaped Channels<sup>1</sup>

The first objective of this chapter is the evaluation of role of the external and internal mass transport in a sinusoidal channel by means of 3-D simulation for catalytic oxidation of formaldehyde. The second objective focuses on the technical feasibility of ultra-low emission limits in the current monolith-like after-treatment technology.

The calculation domain of the 3-D model consists of a channel of real corrugated metallic monolith optimized for formaldehyde oxidation of exhaust gas of the lean-burn NG engines. The influence of the washcoat distribution on the reactor performance is discussed in detail and the catalyst activity and conversion obtained numerically are compared to experimental data. For the modeling of the chemical reactions, the proposed mechanism in Chapter 5 is applied.

### 6.1 Experimental<sup>2</sup>

#### 6.1.1 Monolith Sample

For this study, a Pt model catalyst provided by Heraeus, Hanau, Germany, is used. The washcoat, consisting of 40 g.ft<sup>-3</sup> (1.41 kg.m<sup>-3</sup>) Pt was deposited on a metallic honeycomb with 200 cpsi (31 cpscm). The large channel cross-sections are beneficial for a low pressure-drop. For activity measurements, a cylindrical core of the honeycomb structure with 5 cm length and a diameter of 2.5 cm was used.

#### 6.1.2 Experimental Setup

The catalytic activity for formaldehyde oxidation was measured on an in-house developed test bench. The catalyst samples were placed in a cylindrical quartz glass sample holder inside a quartz tube reactor. The reactor was heated by a 1.4 m long electrical oven (HTM Reetz GmbH) which provided a homogeneous temperature profile along the catalyst bed. Temperature was controlled by a Eurotherm 2208 device with two N-type thermocouples placed 3 mm in front of and behind the monolithic sample. The measurements were conducted at three gas hourly space velocity (GHSV) of 25.000, 50.000 and

---

<sup>1</sup> The methods and results presented in this chapter are taken from [192].

<sup>2</sup> The experimental part is done by T. Schedlbauer.

100.000 h<sup>-1</sup>, corresponding to flow of 11, 22 and 44 slpm ( $1.83 \times 10^{-04}$ ,  $3.67 \times 10^{-04}$  and  $7.33 \times 10^{-04}$  Nm<sup>3</sup>.s<sup>-1</sup>). The tested gas mixtures consist of 100 ppm HCHO, 10 vol. % O<sub>2</sub>, 12 vol. % H<sub>2</sub>O and 6 vol. % CO<sub>2</sub> balanced in N<sub>2</sub>. Temperature was ramped up with 5 K/min from 200 to 500 °C (473-773 K). Reaction products were analyzed by an FT-IR analyzer (MKS Multigas 2030). More details about experimental procedure and set-up description can be found in the study of Schedlbauer et al. [150].

## 6.2 Modeling Approach

The catalytic activity of the sinusoidal-shape channel was investigated using a three-dimensional model. For modeling of the flow field in the monolith channel, calculation of complete Navier-Stocks equations is conducted. The channel and washcoat boundaries were defined from a microscopic picture of the monolith. The calculation domain of the flow field includes the entering flow prior to the channel inlet and the flow passing through the channel. The washcoat was defined as a homogenous isotropic porous medium. Simulations were performed under steady-state isothermal conditions. The CFD code ANSYS-FLUENT [193] was applied for the numerical simulation of the three-dimensional flow field and chemical reactions in the sinusoidal channel. The second-order upwind method was applied for the discretizing of the convective terms.

### 6.2.1 Computational Domain and Boundary Conditions

The computational domain and boundaries were defined based on microscopic pictures taken from the monolith studied (Figure 37). One single channel was selected randomly. It is worth mentioning that, due to manufacturing issues for metallic monoliths, the cross-sectional shape of the channels and washcoat distribution are not essentially the same and the study here attempts to identify the main influencing parameter on the performance of sinusoidal catalytic channels. From Figure 37, it is obvious that, the washcoat materials are mostly gathered at the corners and there is no particular existence of washcoat material on the rest of the perimeter for the modeled channel. The geometrical structure obtained from microscopic picture was then used for making the grid in ANSYS-ICEM [193].

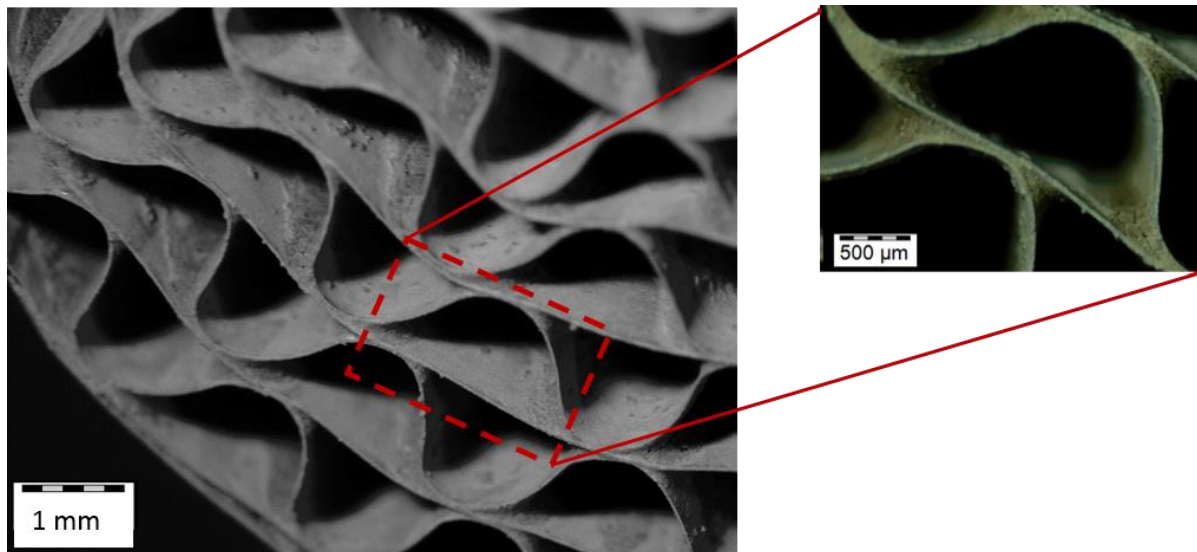


Figure 37: Light microscopic picture of selected channel from tested metallic monolith with 200 cps. The foil thickness is 0.05 mm.

Three different washcoat distribution assumptions were investigated in this study (Figure 38), while the channel geometry was kept the same for all three cases.

The first model assumes a non-uniform distribution of the washcoat accumulated on the channel corners (“corner” model). In this case, the heterogeneous reactions take place in the washcoat volume as indicated by the red area in Figure 38.

The second model implies a uniformly distributed washcoat over the entire channel perimeter (“uniform” model). This model completely neglects the physical thickness of the washcoat. Hence, the catalytic reactions occur only at the interface between wall and channel (red marked area in the figure). In order to consider the effect of washcoat on catalytic surface area, the ratio of catalytic surface area to geometrical surface ( $A_{cat}/A_{geo}$ ) was used. Details concerning this ratio are explained further below.

The last model (“close-to-real”) combines the approaches taken in the “corner” and “uniform” models. The corners are treated identical to first case. Additionally, the channel wall is assumed to be catalytically active, similar to the second model. However, only 10% of the channel wall area is catalytically active in this model considering irregular deposition of washcoat material on metallic substrate. The ( $A_{cat}/A_{geo}$ ) ratio of the catalytic wall defined to be unity. This model resembles the actual washcoat distribution most realistically. This can be seen in Figure 37, which shows the washcoat deposits within the channel. While the majority of the washcoat material is accumulated in the corners in all of the channels, some of the channels also contain spots of washcoat material on the walls.

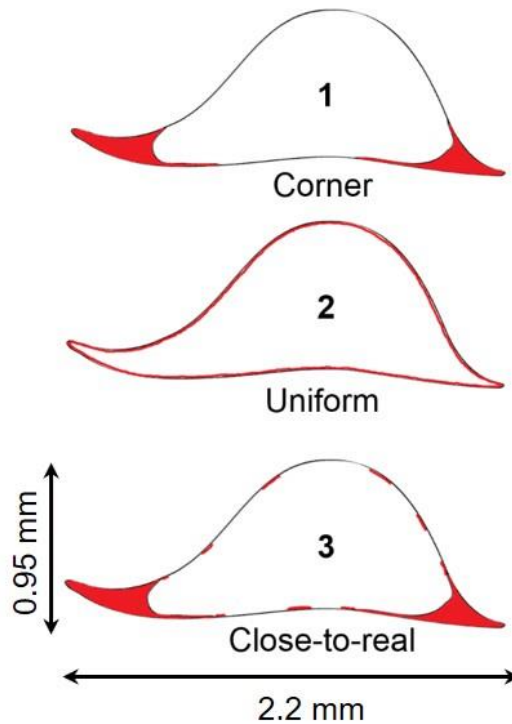


Figure 38: Illustration of washcoat distribution in the modeled sinusoidal channels for 1) first case: non-uniform porous washcoat volume in the corners, “corner”, 2) second case: uniform and infinitely thin washcoat layer over channel perimeter, “uniform” and 3) third case: combination of non-uniform porous washcoat volume and partly catalytic active channel wall, “close-to-real”. The red colored areas represent the washcoat boundaries for each case.

The employed computational models further included 1.0 cm of the entering flow upstream the channel inlet. The size of the grid is 680.000 tetrahedral cells in all cases, which are concentrated near channel inlet with increasing length along axial direction of the channel (Figure 39).

The initial conditions and parameters of the simulations are derived from the experiments. Temperature is set to 400 °C (673 K) for all cases with the gas volume flow of 22 slpm ( $3.67 \times 10^{-4} \text{ Nm}^3 \cdot \text{s}^{-1}$ ) corresponding to GHSV= 50.000  $\text{h}^{-1}$  and uniform inlet velocity of  $2 \text{ m s}^{-1}$  at 400 °C. The gas properties are calculated using mass weighted mixing law [117]. The washcoat porosity, tortuosity and dispersion here are estimated to be 0.5, 3 and 0.1, respectively. These assumptions are in agreement with the values in the literature given for automotive catalytic converters [56,194]. The mixture and effective diffusion coefficient of formaldehyde in bulk and porous medium are calculated to be  $6.8 \times 10^{-5}$  and  $1.3 \times 10^{-5} \text{ m}^2 \cdot \text{s}^{-1}$  at 400 °C. The ratio of the catalytic surface area to geometrical area in second case is derived from Eq.2.48 and 5.5. The calculation leads to  $A_{\text{cat}}/A_{\text{geo}}$  of 16 in the second case.

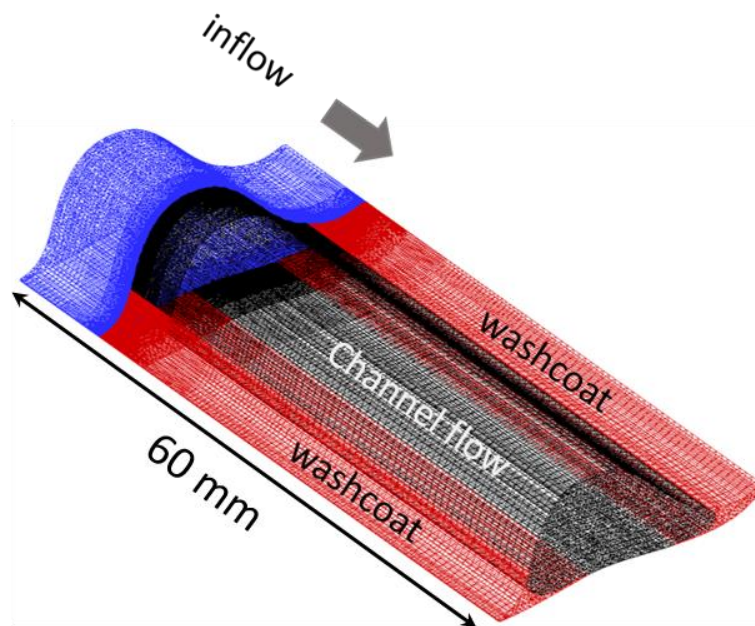


Figure 39: Calculation grid (first case)

## 6.3 Results and Discussion

### 6.3.1 Experimental Investigation of the Metallic Monolith

The experimental results of monolith activity tests are depicted in Figure 40. The high Pt-loading and operation temperature above formaldehyde light-off temperature lead to high conversion over entire temperature range. At lowest space velocity of  $25.000 \text{ h}^{-1}$  complete conversion of formaldehyde is reached already at  $200 \text{ }^{\circ}\text{C}$ . In the present study the complete conversion points to formaldehyde concentration  $<1.0 \text{ ppm}$  at catalyst outlet. In spite of good activity at lowest temperature, the complete conversion of HCHO could not be reached even at temperature as high as  $500 \text{ }^{\circ}\text{C}$  at higher space velocity of  $50.000 \text{ h}^{-1}$ . Increase of volume flow to obtain GHSV of  $100.000 \text{ h}^{-1}$  leads to a substantial reduction of formaldehyde conversion over entire tested temperature range. However, a minor increase in conversion from 83% at  $200 \text{ }^{\circ}\text{C}$  to 90% at  $500 \text{ }^{\circ}\text{C}$  can be seen. The experimental errors that could lead to deviation from 100% conversion, such as bypassed flow and precision of FT-IR device, were checked. The attainable complete conversion with lowest volume flow indicates that bypassed flow is excluded. Moreover, the lowest formaldehyde detectable with used FT-IR analyzer in this study is 36 ppb measuring over 5 minutes time increment and 0.6 ppm measuring every second. The FT-IR

measurement time here is set to 5 seconds to ensure the detection of the formaldehyde concentrations below 1.0 ppm. Each run of light-off tests is repeated three times and the reproducibility and validity of obtained results was confirmed.

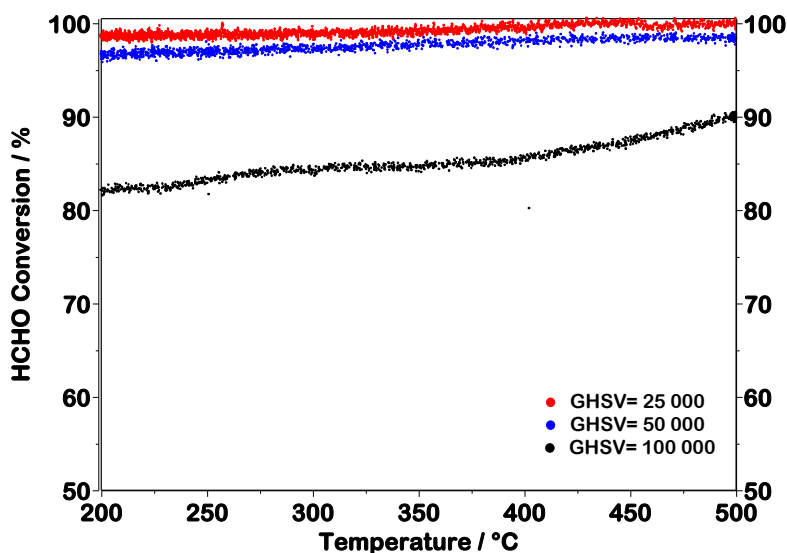


Figure 40: Experimental conversion of HCHO as a function of temperature for tested Pt-catalyst. Gas mixture: 100 ppm HCHO, 10 vol. % O<sub>2</sub>, 12 vol. % H<sub>2</sub>O and 6 vol. % CO<sub>2</sub> balanced in N<sub>2</sub>, GHSV = 25.000 h<sup>-1</sup> (red points) 50.000 h<sup>-1</sup> (blue points) and 100.000 h<sup>-1</sup> (black points)

### 6.3.2 Computational Investigation of Metallic Monolith

The modeling study in the following attempts to enlighten the issues and constraints preventing the complete conversion of formaldehyde in the tested metallic monolith.

#### Porous and Non-Uniform Washcoat Distribution

Based on Figure 41 the z-velocity profile at channel outlet indicates a significant impact of channel and washcoat shape on convective flow and consequently on local residence time of species. Very low permeability of washcoat volume prevents any convective flow inside the washcoat so that the z-velocity at washcoat-channel-interface is equal to zero alike to channel wall. The deeper concavity of washcoat zone on the left side results in faster convective flow on the left edge of channel compared to the right side. The z-velocity profile is fully developed after 5 mm from channel inlet. Convective flow in x and y directions can also be observed over entrance length and particularly at channel inlet. Except for the flow at aforementioned zones, x- and y-velocity components are found to be zero over the entire calculation domain as expected (not shown here).

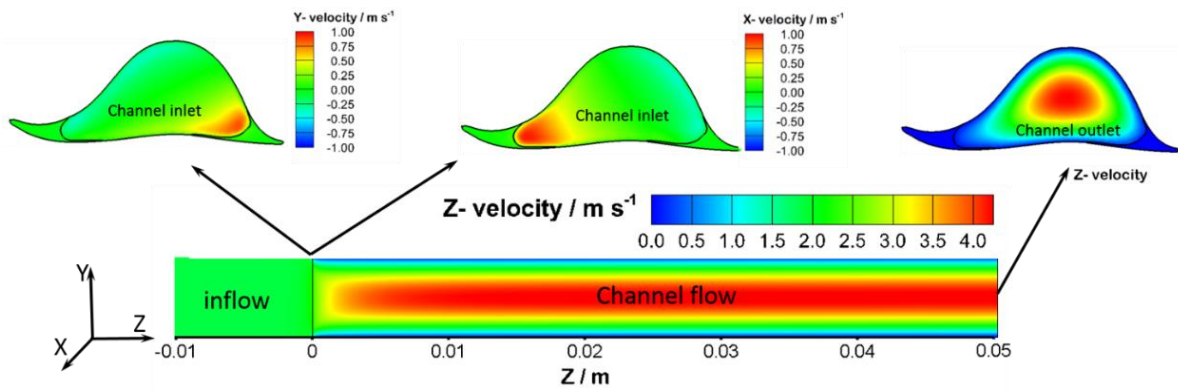


Figure 41: x-, y-velocity profiles at channel inlet in xy-plane and z-velocity in the zy-plane along calculation domain and at the channel outlet in xy-plane (first case).

The 3-D concentration distribution of formaldehyde over the entire domain and at inlet, middle and end of the channel in xy-plane are shown in Figure 42. Here a significant concentration gradient perpendicular to the direction of gas flow can be seen. On one hand, the high reaction rate in the washcoat leads to nearly zero concentration of formaldehyde at the washcoat-flow interface and on the other hand, rather large hydraulic diameter of the channel and respective long diffusion distance cause the concentration gradient. Additionally, an inappropriate accumulation of washcoat material at the edges lengthens the diffusion distance between bulk and catalytic layer. Similar to the velocity profile, the asymmetric cross-sectional shape of the channel and different washcoat geometries on the left and right side affect the concentration distribution. The deeper concavity on the left side causes longer diffusion length in addition to faster convective flow, so that an uneven concentration distribution is formed on the right and left sides.

From Figure 43, which shows the concentration distribution with higher resolution from zero to 25 ppm at channel outlet; can be seen that density of formaldehyde differs around the channel perimeter. The maximum concentration is located between upper channel rim and channel center due to longest diffusion length to the washcoat and higher axial convective flow respectively. Generally, no formaldehyde is detected inside the washcoat as a result of the very high reaction rate.

The calculated formaldehyde concentration exhibits a dominating external mass transport limitation. Since the concentration gradient as driving force for diffusion of formaldehyde molecules becomes smaller along the channel, the inhibited mass transport plays a more pronounced role on formaldehyde consumption with reduction of formaldehyde concentration over the channel length.

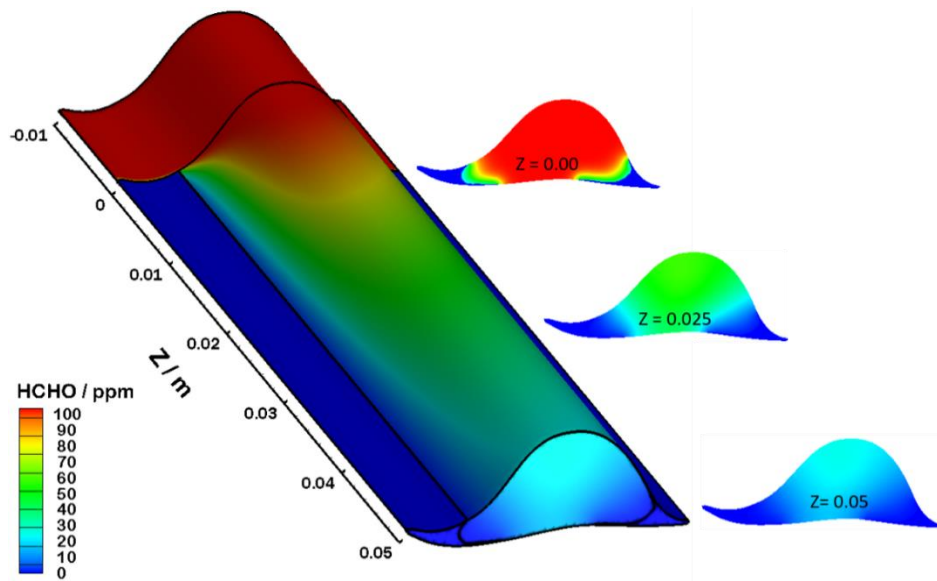


Figure 42: 3-D concentration distribution of formaldehyde along calculation domain and in xy-plane at inlet, middle and outlet of simulated channel (first case).

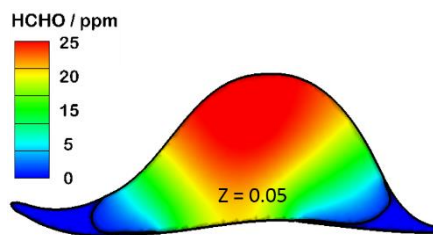


Figure 43: Concentration distribution of formaldehyde in xy-plane at channel outlet in the range of 0 to 25 ppm (first case).

This observation is plotted in Figure 44, which demonstrates the cross-sectional average concentration of formaldehyde for each axial point over channel length. Almost 50% of inlet formaldehyde is converted after 1.1 cm distance from channel inlet but from this position on the initial steep concentration curve becomes more gradual over the rest of the channel length. The concentration at channel outlet is 15 ppm and accounts for 85% conversion, which considerably differs from the conversion level (99%) measured experimentally. The variation of HCHO concentration in Figure 44 reveals that a longer catalytic converter can compensate the low diffusion rate in spite of the fact that higher pressure-drop and loss of precious catalyst material are inevitable.

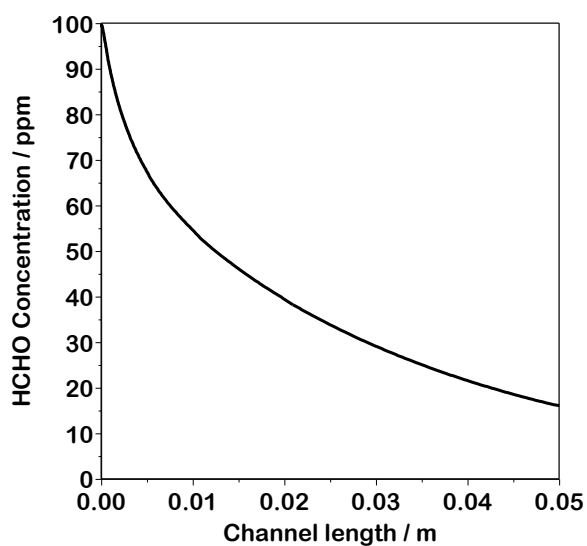


Figure 44: Cross-sectional averaged formaldehyde concentration vs. channel length (first case).

Figure 45 illustrates the influence of local geometric shape of the washcoat on adsorption rate of HCHO along channel length. The highest adsorption rate for both right and left side washcoat volume occurred on the red colored zones. These areas profit from short penetration depth due to thin coating and large contact surface with the channel flow. Except for within the first 2 mm length of the washcoat, no substantial adsorption takes place in the rest of the washcoat volume and the most catalytic material here appears to be left unused. The contribution of dark blue colored region over the first 2 mm can be attributed to not yet developed velocity profile and conceivably convective mass transfer from bulk to washcoat surface immediately at channel entrance in x and y directions. Since the Pt distribution in the washcoat is assumed to be uniform, thicker washcoat with enhanced intraporous diffusion resistance, causes internal mass transport limitation, inadequate for diffusion into the washcoat and further reaction steps.

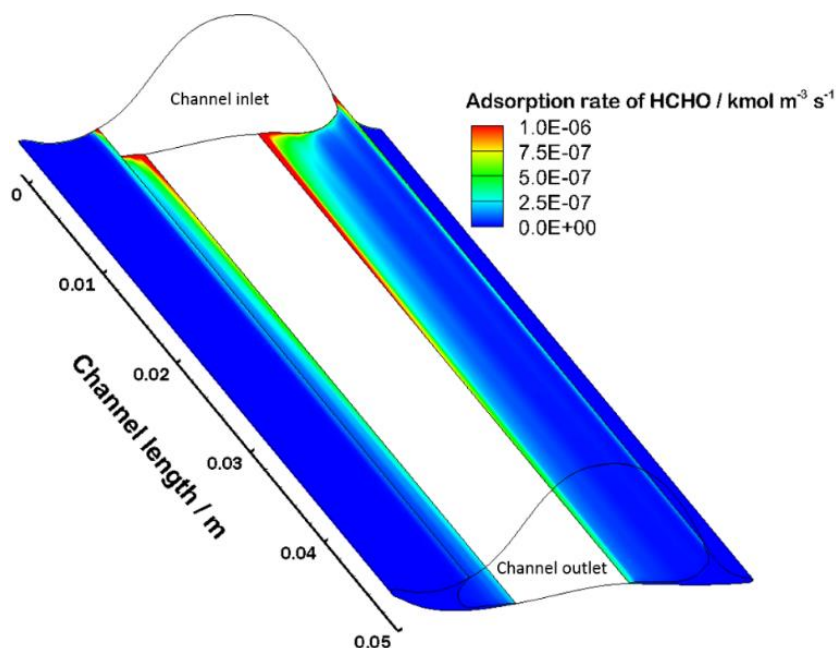


Figure 45: Adsorption rate of HCHO in porous washcoat volume (first case).

### Uniform Infinitely Thin Washcoat Distribution

Figure 46 presents concentration distribution of HCHO for an even and infinitely thin washcoat layer, neglecting the impact of internal mass transport. Due to high reaction rate at 400 °C and uniform washcoat coating, the complete conversion is gained after 3 cm distance from the channel inlet. The concentration profile over reacting channel length shows highest concentration in the channel center and nearly zero at wall, following the velocity distribution, which inherently corresponds to the residence time distribution of the reactant. The high reaction rate on the catalyst surface causes the concentration gradient between bulk and channel wall so that the reaction becomes transport limited over reacting length. Nevertheless, the sufficiently long residence time compared with diffusion time facilitates the complete conversion of HCHO prior to channel outlet.

The simulation results with different value of  $A_{\text{cat}}/A_{\text{geo}}$  (Figure 47) exhibit similar concentration profile, without any noticeable variation, highlighting that at high intrinsic reaction rate, the catalyst activity is solely a function of mass transfer. Furthermore, it can be observed that the catalyst with very low noble metal loading of 2.5 g.ft<sup>-3</sup> can compete fairly with catalysts having considerably higher Pt-loading to perform the similar overall activity. The predicted concentration profile changes only slightly with eight times higher Pt-loading and there is no visible difference between profiles simulated with 20 g.ft<sup>-3</sup> and 40 g.ft<sup>-3</sup> Pt-loading. According to unchanged diffusion length and initial concentration, no improvement in catalyst activity with higher Pt-loading is attainable.

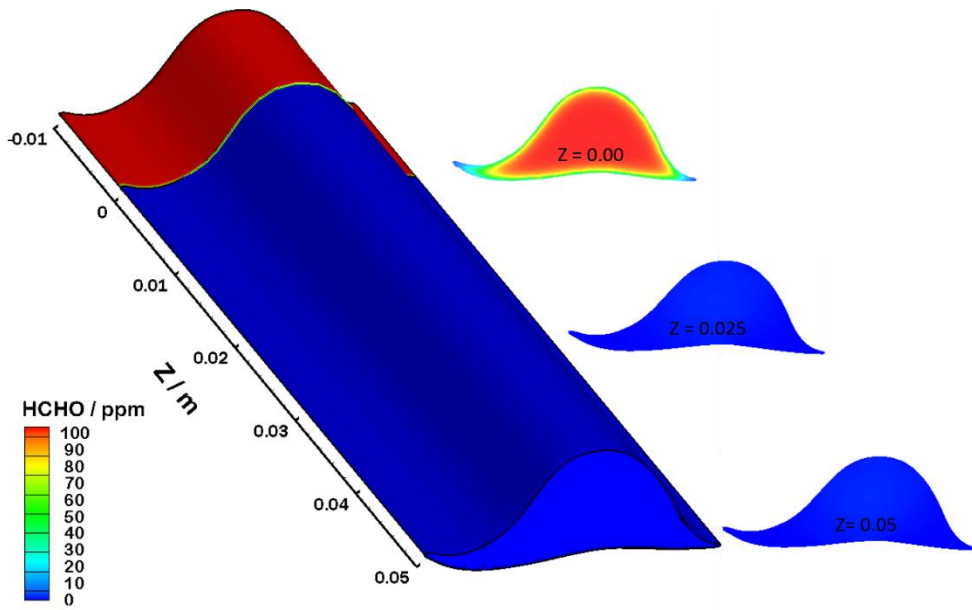


Figure 46: 3-D concentration distribution of formaldehyde along calculation domain and in xy-plan at inlet, middle and outlet of simulated channel (second case)

The averaged formaldehyde concentration along the channel (Figure 47) confirms the enhanced catalyst activity particularly over first 0.5 cm of the channel length, where the diffusion rate is higher than the rest of the channel due to higher concentration of formaldehyde in the bulk. The predicted total conversion shows that the uniformly distributed washcoat can outweigh the transport limitations under tested conditions without changes in catalyst cell density, which essentially increases the pressure-drop over monolithic converter.

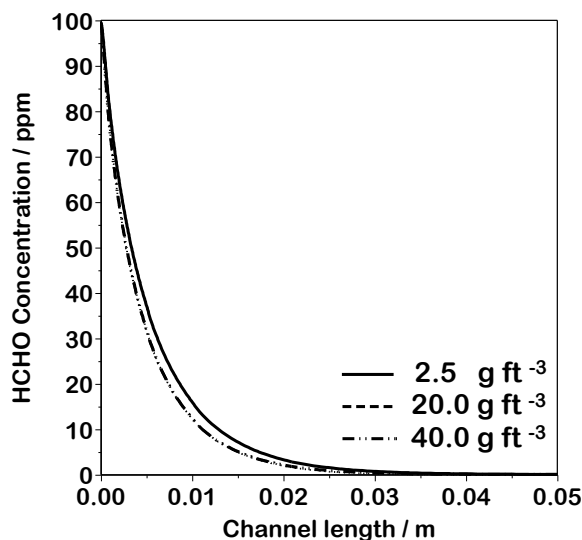


Figure 47: Cross-sectional averaged concentration vs. channel length (second case). Simulated with different platinum loading of 2.5 (solid line), 20 (dashed-line) and 40 (dashed-dotted-line) g ft<sup>-3</sup>.

### Porous and Non-Uniform Washcoat Distribution with Partially Coated Channel Wall

Applying the preceding operation conditions, the third case is a combination of the previous cases consisting of porous washcoat volume at channel edges together with some coating over channel top and bottom rim. This case represents the channels with visually detected washcoat spots on the channel walls in Figure 37, i.e. the most realistic case.

Comparison of the 3-D and 2-D concentration profile in Figure 48 and Figure 49 with the profiles of the first case indicates that partly catalytic activated channel wall substantially enhanced the catalyst performance.

The xy-plane slices in the middle and outlet of the channel in Figure 48 illustrate a more even concentration distribution followed by acceleration of formaldehyde consumption, which indeed can be attributed to shortened diffusion distance as the amount of catalytic material was kept constant. The catalytic active parts on the channel wall induce concentration gradients, intensifying the mass transport from the channel center to the catalytic surfaces. The adsorption rate is accordingly higher on catalytic coated sections of the channel wall in absence of internal diffusion limitation than that in porous washcoat. In this case, 50 % conversion is gained after 0.8 cm distance from the channel inlet and the effluent gas mixture contains 1 ppm HCHO. The computationally predicted outlet concentration is now well comparable with experimental data.

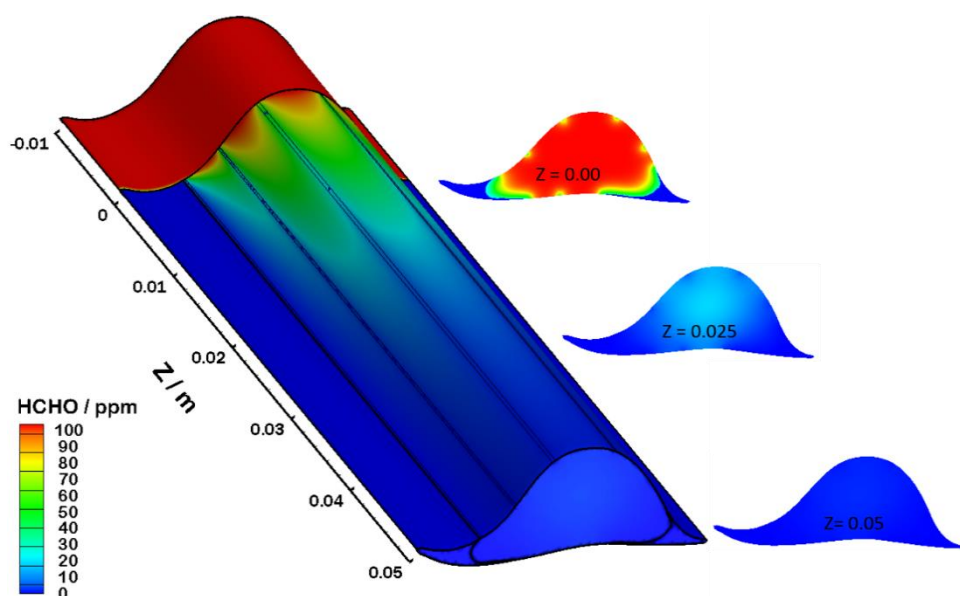


Figure 48: 3-D concentration distribution of formaldehyde along calculation domain and in xy-plan at inlet, middle and outlet of simulated channel (third case, porous WC with partially coated channel wall)

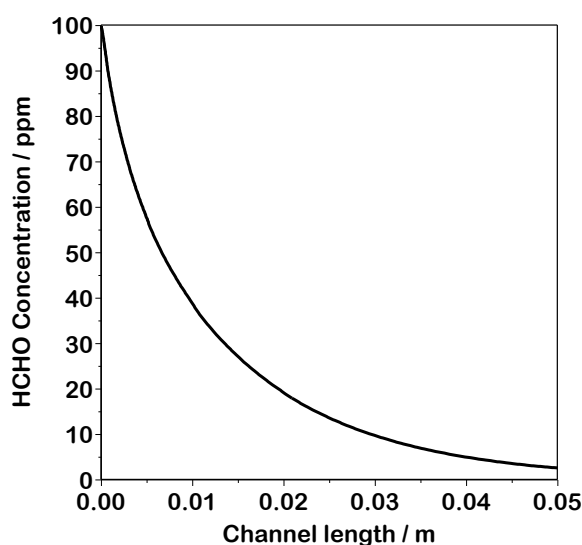


Figure 49: Cross-sectional averaged concentration vs. channel length (third case).

All three models confirmed that the catalytic oxidation of formaldehyde in the tested monolith is limited by external mass transport, which is a function of concentration gradient and diffusion distance between bulk and catalytic surface. The rather large channel diameter and decreasing reactant concentration along reacting length weaken mass transfer leading to a reduced apparent reaction rate. Nevertheless, the simulation result of second case “uniform” has shown that modeled channel is able to convert formaldehyde completely after 3 cm from channel inlet. At this axial point, the accomplished conversion levels are 73 % and 90 % for first case “corner” and third case “close-to-real” respectively.

After all, the experimentally measured conversion level was a result of performance of diverse channels and washcoat geometry, which were assuredly operated under mass transport inhibited regime over entire tested temperature range. The slightly less conversion obtained experimentally at lower temperature can be related to lower diffusion coefficient of formaldehyde with decreasing temperature and minor reduction of mass transport rate. Note that the simulations shown in this study were conducted with GHSV = 50.000 h<sup>-1</sup>. In the real application, this value can be as high as 200.000 h<sup>-1</sup> or higher, which worsens the problem. The high volume flow causes shorter residence time, not long enough to overcome the diffusion limitation so that for low concentration level of formaldehyde a long catalyst, providing longer residence time, is needed to reach a formaldehyde-free exhaust gas.

## 6.4 Summary

Metallic honeycombs, used as formaldehyde oxidation catalyst in this study, are popular in after-treatment applications due to higher stability, better thermal conductivity and lower back-pressure comparing with the ceramic one.

This chapter reported on mathematical modeling of a sinusoidal channel of a washcoated metallic honeycomb for abatement of formaldehyde emissions from lean-burn engines. It is shown experimentally that at a typical space velocity of  $50.000\text{ h}^{-1}$  or higher the complete conversion of formaldehyde cannot be reached. A CFD isothermal model fully accounting for 3-D distribution of variables including internal distribution in the washcoat layer is adopted to investigate the oxidation of formaldehyde at very high conversion levels. To assure that the study accounts for all distribution possibilities, three different WC distribution were modeled. Specifically, the effect of washcoat distribution is investigated by comparing two limiting cases, i.e. washcoat only present in the channel corners and perfectly uniform washcoat thickness along the channel perimeter, with a more "realistic" one which assumes washcoat accumulation in the corners and partial coating of the channel perimeter.

While the experimental results demonstrate a very high activity over the entire temperature range, the simulation results point that all three washcoat distribution models operate under mass transport limited regime. This study reveals constraints and limitation of monolithic substrate in term of ultra-low emission level. It also emphasizes that in case of ultra-low emission level the apparent reaction rate is independent of amount of catalytic material and washcoat distribution.

Moreover, it is found out that due to irregular washcoat deposition fully detailed multi-channel models are required for correct prediction of the performances, particularly when very high conversion levels are required.

## 7 Summary and Outlook

Natural-gas-fueled engines are becoming an attractive technology in the energy sector and the decentralized power generation owing to their principally lower environmental impact compared to other engines powered by fossil fuels. In this field, the lean combustion concept has shown to improve thermal efficiency and to lower the emission of nitrogen oxides, simultaneously. The application of a turbo charger contributes to further improvement of efficiency due to the higher air to fuel ratio, but has its drawback on formaldehyde emission as an intermediate species of methane oxidation. Formaldehyde contributes to photochemical smog and has carcinogenic properties, and is hence categorized as a hazardous air pollutant. Furthermore, the strong contribution of methane to the greenhouse effect, the continuously tightening emission legislation and the growing popularity of gas engines have led to the development of measures and strategies for abatement of unburnt hydrocarbons and intermediates from gas engines.

The origin of hydrocarbon emissions is the incomplete fuel combustion. The unburnt hydrocarbons at exhaust port further reacts to form other hydrocarbons or exit the tailpipe as hydrocarbon slip. The initiation temperature of hydrocarbon oxidation is generally higher than exhaust temperature. However, presence of a few ppm  $\text{NO}_x$  significantly reduces the onset temperature of the hydrocarbon oxidation. Application of turbocharge in lean-burn NG engines results in an elevated pressure prior to the turbine. The pressure in the exhaust can reach up to 5.0 bar prior to the turbo charger, which consequently prolongs the gas residence time upstream the turbine position. It is shown both experimentally and numerically that the extended residence time in combination with the catalytic effect of  $\text{NO}_x$  on the oxidation of hydrocarbons results in substantial conversion of hydrocarbons depending on operating conditions. Under lean conditions, the promoting effect of  $\text{NO}_x$  depends on temperature, pressure,  $\text{NO}/\text{NO}_2$  ratio, net concentration of  $\text{NO}_x$ , and composition of the radical pool. The main oxidation product under exhaust condition is CO accompanied by few ppm (up to 150 ppm) formaldehyde and ethylene. At high temperature and sufficiently long residence time, the products of partial oxidation react further to form water and  $\text{CO}_2$ . It is shown experimentally that high  $\text{NO}_x$  concentration  $> 500$  ppm particularly at low temperatures leads to the formation of undesired nitrogen containing species like HONO and  $\text{CH}_3\text{NO}_2$ . Once these species are formed, they remain in the mixture and act as sink in  $\text{NO}_x$  concentration. The presence of 5 ppm  $\text{SO}_2$  in the gas mixture does not affect the oxidation rate of hydrocarbons in the gas phase. The experimental observations and results are modeled applying detailed reaction mechanisms from literature. The concentration of intermediate and ultimate concentration of hydrocarbons under various conditions could be predicted with reasonable accuracy. The used reactor model is evaluated based on results derived from a CSTR-cascade approach, which accounts for

nonideal conditions in practical applications. It can be concluded from the results presented in this study that under proper exhaust conditions significant oxidation of hydrocarbons can be gained in the gas-phase. However, further studies are needed to investigate operational issues and challenges, as the gas-phase reaction times are not as short as catalytic ones. For stationary and large-bore gas engine applications operated without fast load changes, the method introduced in this thesis might be of great interest.

Beside primary measures to reduce pollutant emission, catalytic systems have been widely used as a key part of the emission control system over the last decades. Several studies discussed the application of Pd- and Pt-based catalysts for lean-burn gas engines as they showed superior catalytic performance for the total oxidation of methane, and formaldehyde respectively, under lean-burn conditions [33,37,38,46–48,137]. However, the inevitable exhaust gas component, water, inhibits the total oxidation of methane on Pd-based catalysts, which leads to a continuous deactivation with time on stream. Thus, the light-off temperature of methane oxidation shifts to the elevated temperature range (450 - 550 °C) [34,39,41], which might not be reached in the exhaust of lean-burn engines.

One option for increasing the operation temperature for catalytic oxidation of methane is the positioning of the converter close to the engine; prior to the turbocharger, where the exhaust gas possesses higher temperature and pressure. Assuming constant temperature and inlet concentration of species, for a first order reaction, the apparent reaction rate depends solely on intrinsic reaction rate for kinetically controlled reaction, whereas it is a function of diffusion rate for a mass transfer controlled one. In this regard, the importance of elevated pressure is less pronounced for catalysts with larger channel diameter and the positive effect of pressure on residence time is compensated by a lower diffusion coefficient. Moreover, the effect of pressure can also depend on the kinetics. The experimental results performed on a 400 cpsi monolithic converters show that the catalytic oxidation reaction of methane is kinetically controlled and thus no mass transport inhibition is caused with higher pressure. It is also shown in this study that although the catalyst can benefit from extended residence time in dry and wet conditions but the overall activity is inhibited by higher partial pressure of present water at higher pressure. Therefore, the positive effect of pressure is compensated through higher concentration of water in the system.

Taking the benefit of higher temperature close to the engine into account, pre-turbo positioning of the catalyst can be still an option to reach a better performance of exhaust catalysts for lean-burn NG engine applications. However, long-term activity tests including more advanced and robust catalyst formulations have to be performed to evaluate the effect of pressure increment on catalyst deactivation due to presence of water over the catalyst lifetime. Furthermore, the reversibility of the deactivation process under pre-turbine conditions and with a real exhaust gas mixture containing various HCs, NO<sub>x</sub> and CO needs to be studied.

Considering the necessity of reduction of formaldehyde slip, catalytic converters in form of oxidation catalyst are the best options. Pt-based catalyst have shown very high activity for oxidation of formaldehyde and the activity measurements with powder Pt-TiO<sub>2</sub> catalyst demonstrate a very low light-off temperature. The proposed reaction mechanism for formaldehyde oxidation under oxygen-rich conditions in this study reveals that at temperatures lower than ignition temperature of formaldehyde the surface is blocked with adsorbed OH species. At ignition temperature adsorbed oxygen (O(s)) species become the most abundant surface species.

High intrinsic reaction rate of formaldehyde oxidation over Pt-based catalysts leads to a mass transport controlled catalytic reaction at the dominated temperature range in the exhaust (100-500 °C). Simulation results have shown that external mass transport of the reactant is the rate-limiting step and the reduction in concentration gradient along channel decreases the diffusion rate. This behavior is inevitable since ultra-low emission level is considered. Application of a monolith with longer channels or smaller channel diameter, in other words a monolith with higher cell density, have a positive bearing on reduction of diffusion limitation. However, these structural changes lead to higher pressure-drop, larger space demand and/or higher manufacturing costs, unattractive both technically and economically. Since molecular diffusion is almost temperature independent and the catalytic reaction is controlled by mass transport, increase of operation temperature in order to gain higher apparent reaction rate is also not an option. Therefore, aside from analytical constraints, the realization of ultra-low emission level (less than 1 ppm) through the application of monolithic converters, is technically hard to achieve.

The simulated results of this study have shown that a uniform washcoat distribution is a prerequisite for high catalyst performance. Hence, the application of monoliths with higher cell density and accordingly higher pressure-drop can be skipped for certain conditions and volume flow. Generally, the knowledge of washcoat distribution along reacting distance is required for a rigorous modeling study. The thin layers of the washcoat, with low diffusion resistance, have the most contribution to the catalytic reactions and the catalyst materials inside thick layers at channel corners are indeed left untapped. Furthermore, the washcoat distribution and shape of channel perimeter has a considerable effect on velocity and consequently diffusion rate as well as concentration profile. The latter point emphasizes that the geometry simplifications to reduce the computational efforts, such as evenly distributed washcoat over channel perimeter or channel length, symmetric channel cross-section and elimination of washcoat thickness, can reduce the accuracy of the simulation results. In other words, one sinusoidal channel of metallic monolith operating under transport limitation conditions is not representative for the entire monolith as it might be for ceramic monolith with symmetric cross-sectional shape and more uniform washcoat distribution [56,194,195]. The numerical results here also suggest that it is worth exploring the catalyst performance applying 3-D modeling studies to obtain an overview of limitations and influencing parameters.

Finally, the results of this thesis lead to the conclusion that there might often be a trade-off between strengths and weaknesses of measures and methods applied for improvement of system efficiency. For instance, while higher pressure and temperature prior to the turbocharger are beneficial for reduction of methane slip through homogenous oxidation reactions, they can simultaneously lead to an increased concentration of formaldehyde slip. The same trend is observed in pre-turbine positioning of the methane catalyst. The higher temperature close to the engine facilitates the faster kinetic, whereas higher pressure intensifies the inhibitory effect of water. Furthermore, it is evident, that material improvement, adjustment of operation conditions or prevention of catalyst aging and poisoning to gain better catalyst activity do not always suffice to ensure emission free exhaust gas as long as monolith-like catalytic converters are applied.

## References

- [1] S. Faramawy, T. Zaki, A.A.-E. Sakr, Natural gas origin, composition, and processing: A review, *Journal of Natural Gas Science and Engineering* 34 (2016) 34–54.
- [2] S. Mokhatab, W.A. Poe, J.G. Speight, G. Zatzman, Handbook of natural gas transmission and processing, Gulf Professional Publ, Burlington, MA, 2006.
- [3] H.P. Mtui PL (Ed.), Ignition Delay and Combustion Duration with Natural Gas Fueling of Diesel Engines, *SAE Technical Paper* 961933, 1996.
- [4] Reuss, G., Disteldorf, W., Gamer, A. O. and Hilt, A, Formadehyde, *Ullmann's Encyclopedia of Industrial Chemistry* 15 (2000) 735–768.
- [5] ECHA, EU Verordnung Nr. 605/2014, Legal Rule or Regulation, 2014.
- [6] E.S. Cramer, M.S. Briggs, N. Liu, B. Mailyan, J.R. Dwyer, H.K. Rassoul, The impact on the ozone layer from NO<sub>x</sub> produced by terrestrial gamma ray flashes, *Geophysical Research Letters* 44 (2017) 5240–5245.
- [7] C.E. Reeves, S.A. Penkett, S. Bauguitte, K.S. Law, M.J. Evans, B.J. Bandy, P.S. Monks, G.D. Edwards, G. Phillips, H. Barjat, J. Kent, K. Dewey, S. Schmitgen, D. Kley, Potential for photochemical ozone formation in the troposphere over the North Atlantic as derived from aircraft observations during ACSOE, *Journal of Geophysical Research: Atmospheres* 107 (2002) ACH 14-1-ACH 14-14.
- [8] National Academies Press (US), Acute Exposure Guideline Levels for Selected Airborne Chemicals: Volume 8, Washington (DC), 2010.
- [9] N. Englert, Fine particles and human health: a review of epidemiological studies, *Toxicology letters* 149 (2004) 235–242.
- [10] R.A. Michaels, M.T. Kleinman, Incidence and Apparent Health Significance of Brief Airborne Particle Excursions, *Aerosol Science and Technology* 32 (2000) 93–105.
- [11] H.M. Cho, B.-Q. He, Spark ignition natural gas engines—A review, *Energy Conversion and Management* 48 (2007) 608–618.
- [12] R.J. Tabaczynski, J.B. Heywood, J.C. Keck, Time-Resolved Measurements of Hydrocarbon Mass Flowrate in the Exhaust of a Spark-Ignition Engine, in: *SAE Technical Paper* 720112.
- [13] E. Riedel, Anorganische Chemie, 3rd ed., Walter de Gruyter, Berlin, New York, 1994.
- [14] Charles E. Mitchell, Daniel B. Olsen, Formaldehyde Formation in Large Bore Natural Gas Engines, *Journal of Engineering for Gas Turbines and Power* 122 (2000) 603–610.
- [15] M. Lemel, A. Hultqvist, A. Vressner, H. Nordgren, H. Persson, B. Johansson, Quantification of the Formaldehyde Emissions from Different HCCI Engines Running on a Range of Fuels, in: *SAE Transactions* 2005-01-3724, pp. 1347–1357.

- [16] F. Owrang, J. Olsson, J. Pedersen, Chemical Analysis of Combustion Products From an Engine Power Plant Fuelled With Natural Gas. *SAE Technical Paper* 2004-01-1928, 2004.
- [17] D.B. Olsen, C.E. Mitchell, Formaldehyde Formation in Large Bore Engines Part 2: Factors Affecting Measured CH<sub>2</sub>O, *Journal of Engineering for Gas Turbines and Power* 122 (2000) 611.
- [18] Per Amnéus, Martin Tunér, Fabian Mauss, Robert Collin, Jenny Nygren, Mattias Richter Marcus Aldén, Formaldehyde and Hydroxyl Radicals in an HCCI Engine – Calculations and LIF-Measurements, *SAE Technical Papers* 2007-01-0049 (2007).
- [19] M.U. Alzueta, P. Glarborg, Formation and Destruction of CH<sub>2</sub>O in the Exhaust System of a Gas Engine, *Environmental Science & Technology* 37 (2003) 4512–4516.
- [20] D.B. Olsen, B.D. Willson, The Effect of Retrofit Technologies on Formaldehyde Emissions from a Large Bore Natural Gas Engine, *Energy and Power Engineering* 03 (2011) 574–579.
- [21] P.G.E.R. Kristensen, B. Karll, A.B. Bendtsen, P. Glarborg, K.I.M. Dam-Johansen, Exhaust Oxidation of Unburned Hydrocarbons from Lean-Burn Natural Gas Engines, *Combustion Science and Technology* 157 (2007) 262–292.
- [22] J.H.E. Arts, H. Muijser, C.F. Kuper, R.A. Woutersen, Setting an indoor air exposure limit for formaldehyde, *Regulatory toxicology and pharmacology* 52 (2008) 189–194.
- [23] I. Lang, T. Bruckner, G. Triebig, Formaldehyde and chemosensory irritation in humans, *Regulatory toxicology and pharmacology RTP* 50 (2008) 23–36.
- [24] Y. Sekine, Removal of formaldehyde from indoor air by passive type air-cleaning materials, *Atmospheric Environment* 35 (2001) 2001–2007.
- [25] K.B. Rumchev, J.T. Spickett, M.K. Bulsara, M.R. Phillips, S.M. Stick, Domestic exposure to formaldehyde significantly increases the risk of asthma in young children, *European Respiratory Journal* 20 (2002) 403–408.
- [26] J.H.E. Arts, M.A.J. Rennen, C. de Heer, Inhaled formaldehyde, *Regulatory toxicology and pharmacology* 44 (2006) 144–160.
- [27] T. Korakianitis, A.M. Namasivayam, R.J. Crookes, Natural-gas fueled spark-ignition (SI) and compression-ignition (CI) engine performance and emissions, *Progress in Energy and Combustion Science* 37 (2011) 89–112.
- [28] CIMAC Position Paper, *International council on combustion engines* 2017.
- [29] G. Pirker, A. Wimmer, Sustainable power generation with large gas engines, *Energy Conversion and Management* 149 (2017) 1048–1065.
- [30] J. Laurikko, On exhaust emissions from petrol-fuelled passenger cars at low ambient temperatures. Zugl.: Espoo, Univ., Diss., 1998, Technical Research Centre of Finland, Espoo, 1998.

- [31] Dieselnet, Light-Duty Vehicles: GHG Emissions & Fuel Economy, [https://www.dieselnet.com/standards/us/fe\\_ghg.php](https://www.dieselnet.com/standards/us/fe_ghg.php).
- [32] D. Ciuparu, M.R. Lyubovsky, E. Altman, L.D. Pfefferle, A. Datye, Catalytic Combustion of Methane over Palladium-Based Catalysts, *Catalysis Reviews* 44 (2002) 593–649.
- [33] P. Gélin, M. Primet, Complete oxidation of methane at low temperature over noble metal based catalysts: a review, *Applied Catalysis B: Environmental* 39 (2002) 1–37.
- [34] A.T. Gremminger, H.W. Pereira de Carvalho, R. Popescu, J.-D. Grunwaldt, O. Deutschmann, Influence of gas composition on activity and durability of bimetallic Pd-Pt/Al<sub>2</sub>O<sub>3</sub> catalysts for total oxidation of methane, *Catalysis Today* 258 (2015) 470–480.
- [35] P. Castellazzi, G. Groppi, P. Forzatti, A. Baylet, P. Marécot, D. Duprez, Role of Pd loading and dispersion on redox behaviour and CH<sub>4</sub> combustion activity of Al<sub>2</sub>O<sub>3</sub> supported catalysts, *Catalysis Today* 155 (2010) 18–26.
- [36] C.A. Müller, M. Maciejewski, R.A. Koepfel, A. Baiker, Combustion of methane over palladium/zirconia: effect of Pd-particle size and role of lattice oxygen, *Catalysis Today* 47 (1999) 245–252.
- [37] D. Ciuparu, E. Perkins, L. Pfefferle, In situ DR-FTIR investigation of surface hydroxyls on  $\gamma$ -Al<sub>2</sub>O<sub>3</sub> supported PdO catalysts during methane combustion, *Applied Catalysis A: General* 263 (2004) 145–153.
- [38] W.R. Schwartz, D. Ciuparu, L.D. Pfefferle, Combustion of Methane over Palladium-Based Catalysts: Catalytic Deactivation and Role of the Support, *Journal of Physical Chemistry C* 116 (2012) 8587–8593.
- [39] L.S. Escandón, D. Niño, E. Díaz, S. Ordóñez, F.V. Díez, Effect of hydrothermal ageing on the performance of Ce-promoted PdO/ZrO<sub>2</sub> for methane combustion, *Catalysis Communications* 9 (2008) 2291–2296.
- [40] A. Gremminger, P. Lott, M. Merts, M. Casapu, J.-D. Grunwaldt, O. Deutschmann, Sulfur poisoning and regeneration of bimetallic Pd-Pt methane oxidation catalysts, *Applied Catalysis B: Environmental* 218 (2017) 833–843.
- [41] R. Gholami, M. Alyani, K. Smith, Deactivation of Pd Catalysts by Water during Low Temperature Methane Oxidation Relevant to Natural Gas Vehicle Converters, *Catalysts* 5 (2015) 561–594.
- [42] C. Zhang, H. He, A comparative study of TiO<sub>2</sub> supported noble metal catalysts for the oxidation of formaldehyde at room temperature, *Catalysis Today* 126 (2007) 345–350.
- [43] S. Colussi, M. Boaro, L. de Rogatis, A. Pappacena, C. de Leitenburg, J. Llorca, A. Trovarelli, Room temperature oxidation of formaldehyde on Pt-based catalysts, *Catalysis Today* 253 (2015) 163–171.

- [44] C. Zhang, H. He, K.-i. Tanaka, Catalytic performance and mechanism of a Pt/TiO<sub>2</sub> catalyst for the oxidation of formaldehyde at room temperature, *Applied Catalysis B: Environmental* 65 (2006) 37–43.
- [45] B. Bai, Q. Qiao, J. Li, J. Hao, Progress in research on catalysts for catalytic oxidation of formaldehyde, *Chinese Journal of Catalysis* 37 (2016) 102–122.
- [46] R. W. McCabe, D. F. McCready, Formaldehyde oxidation on Pt, *Chemical Physics Letters* 111 (1984) 89–93.
- [47] G.A. Attard, H.D. Ebert, R. Parsons, Formaldehyde decomposition and oxidation on Pt(110), *Surface Science* 240 (1990) 125–135.
- [48] S. Li, X. Lu, W. Guo, H. Zhu, M. Li, L. Zhao, Y. Li, H. Shan, Formaldehyde oxidation on the Pt/TiO<sub>2</sub>(101) surface, *Journal of Organometallic Chemistry* 704 (2012) 38–48.
- [49] H.-S. Roh, D.K. Lee, K.Y. Koo, U.H. Jung, W.L. Yoon, Natural gas steam reforming for hydrogen production over metal monolith catalyst with efficient heat-transfer, *International Journal of Hydrogen Energy* 35 (2010) 1613–1619.
- [50] H. Mei, C. Li, S. Ji, H. Liu, Modeling of a metal monolith catalytic reactor for methane steam reforming–combustion coupling, *Chemical Engineering Science* 62 (2007) 4294–4303.
- [51] J. Chen, H. Yang, N. Wang, Z. Ring, T. Dabros, Mathematical modeling of monolith catalysts and reactors for gas phase reactions, *Applied Catalysis A: General* 345 (2008) 1–11.
- [52] G. Groppi, E. Tronconi, Honeycomb supports with high thermal conductivity for gas/solid chemical processes, *Catalysis Today* 105 (2005) 297–304.
- [53] O. Deutschmann (ed.), *Modeling and Simulation of Heterogeneous Catalytic Reactions*, Wiley-VCH Verlag GmbH & Co. KGaA, Weinheim, Germany, 2011.
- [54] S.Y. Joshi, M.P. Harold, V. Balakotaiah, Overall mass transfer coefficients and controlling regimes in catalytic monoliths, *Chemical Engineering Science* 65 (2010) 1729–1747.
- [55] M.L. Rodríguez, L.E. Cadús, Mass transfer limitations in a monolithic reactor for the catalytic oxidation of ethanol, *Chemical Engineering Science* 143 (2016) 305–313.
- [56] N. Mladenov, J. Koop, S. Tischer, O. Deutschmann, Modeling of transport and chemistry in channel flows of automotive catalytic converters, *Chemical Engineering Science* 65 (2010) 812–826.
- [57] H. More, R.E. Hayes, B. Liu, M. Votsmeier, M.D. Checkel, The Effect of Catalytic Washcoat Geometry on Light-off in Monolith Reactors, *Topics in Catalysis* 37 (2006) 155–159.
- [58] A. Tilland, J.-F. Portha, L. Falk, C. Tardivat, Impact of reducing the channel diameter on heterogeneous gas reactions in an isothermal monolith, *Chemical Engineering and Processing: Process Intensification* 95 (2015) 317–326.

- [59] R.E. Hayes, B. Liu, R. Moxom, M. Votsmeier, The effect of washcoat geometry on mass transfer in monolith reactors, *Chemical Engineering Science* 59 (2004) 3169–3181.
- [60] S.Y. Joshi, M.P. Harold, V. Balakotaiah, On the use of internal mass transfer coefficients in modeling of diffusion and reaction in catalytic monoliths, *Chemical Engineering Science* 64 (2009) 4976–4991.
- [61] R.E. Hayes, S.T. Kolaczkowski, Mass and heat transfer effects in catalytic monolith reactors, *Chemical Engineering Science* 49 (1994) 3587–3599.
- [62] E.G.W. Day, S.F. Benjamin, C.A. Roberts, Simulating Heat Transfer in Catalyst Substrates with Triangular and Sinusoidal Channels and the Effect of Oblique Inlet Flow, *SAE Technical Papers 2000-01-0206* (2000).
- [63] M. Iwaniszyn, J. Kryca, P.J. Jodłowski, M. Piątek, A. Gancarczyk, J. Łojewska, A. Kołodziej, Novel intense metallic monolith for automotive applications, *Comptes Rendus Chimie* 18 (2015) 1030–1035.
- [64] S.T. Kolaczkowski, Measurement of effective diffusivity in catalyst-coated monoliths, *Catalysis Today* 83 (2003) 85–95.
- [65] S.-A. Seyed-Reihani, G.S. Jackson, Effectiveness in catalytic washcoats with multi-step mechanisms for catalytic combustion of hydrogen, *Chemical Engineering Science* 59 (2004) 5937–5948.
- [66] G. Groppi, E. Tronconi, Theoretical analysis of mass and heat transfer in monolith catalysts with triangular channels, *Chemical Engineering Science* 52 (1997) 3521–3526.
- [67] S. Tischer, O. Deutschmann, Recent advances in numerical modeling of catalytic monolith reactors, *Catalysis Today* 105 (2005) 407–413.
- [68] L.L. Raja, R.J. Kee, O. Deutschmann, J. Warnatz, L. D. Schmidt, A critical evaluation of Navier–Stokes, boundary-layer, and plug-flow models of the flow and chemistry in a catalytic-combustion monolith, *Catalysis Today* 59 (2000) 47–60.
- [69] R.E. Hayes, B. Liu, M. Votsmeier, Calculating effectiveness factors in non-uniform washcoat shapes, *Chemical Engineering Science* 60 (2005) 2037–2050.
- [70] D. Papadias, L. Edsberg, P. BjoKrnbohm, Simplified method for effectiveness factor calculations in irregular geometries of washcoats, *Chemical Engineering Science* 55 (2000) 1447–1459.
- [71] H. Santos, J. Pires, M. Costa, Influence of the Washcoat Structure in the Performance of Automotive Three Way Catalysts, *SAE International Journal of Engines* 6 (2013) 1846–1854.
- [72] M.J. Stutz, D. Poulikakos, Optimum washcoat thickness of a monolith reactor for syngas production by partial oxidation of methane, *Chemical Engineering Science* 63 (2008) 1761–1770.

- [73] T. Rammelt, B. Torkashvand, C. Hauck, J. Böhm, R. Gläser, O. Deutschmann, Nitric Oxide Reduction of Heavy-Duty Diesel Off-Gas by NH<sub>3</sub>-SCR in Front of the Turbocharger, *Emission Control Science and Technology* 3 (2017) 275–288.
- [74] T.J. Schildhauer, M. Elsener, J. Moser, I. Begsteiger, D. Chatterjee, K. Rusch, O. Kröcher, Measurement of Vanadium Emissions from SCR Catalysts by ICP-OES: Method Development and First Results, *Emission Control Science and Technology* 1 (2015) 292–297.
- [75] M.N. Subramaniam, C. Hayes, D. Tomazic, M. Downey, C. Bruestle, Pre-Turbo Aftertreatment Position for Large Bore Diesel Engines - Compact & Cost-Effective Aftertreatment with a Fuel Consumption Advantage, *SAE International Journal of Engines* 4 (2011) 106–116.
- [76] T. Günter, J. Pesek, K. Schäfer, A. Bertóiné Abai, M. Casapu, O. Deutschmann, J.-D. Grunwaldt, Cu-SSZ-13 as pre-turbine NO<sub>x</sub>-removal-catalyst: Impact of pressure and catalyst poisons, *Applied Catalysis B: Environmental* 198 (2016) 548–557.
- [77] O. Kröcher, M. Elsener, M.-R. Bothien, W. Dölling, Pre-Turbo Scr - Influence of Pressure on NO<sub>x</sub> Reduction, *MTZ Worldwide* 75 (2014) 46–51.
- [78] H. Harndorf (Ed.), Die Zukunft der Großmotoren II: Im Spannungsfeld von Emissionen, Kraftstoffen und Kosten, expert-Verl., Renningen, 2012.
- [79] V. Bermúdez, J.R. Serrano, P. Piqueras, Ó. García-Afonso, Analysis of heavy-duty turbocharged diesel engine response under cold transient operation with a pre-turbo aftertreatment exhaust manifold configuration, *International Journal of Engine Research* 14 (2013) 341–353.
- [80] A.B. Bendtsen, P. Glarborg, K.I.M. Dam-Johansen, Low temperature oxidation of methane: the influence of nitrogen oxides, *Combustion Science and Technology* 151 (2000) 31–71.
- [81] W.K. Cheng, D. Hamrin, J.B. Heywood, S. Hochgreb, K. Min, M. Norris, An Overview of Hydrocarbon Emissions Mechanisms in Spark-Ignition Engines, *SAE Technical Papers* 932708 (1993).
- [82] K. Drobot, W.K. Cheng, F.H. Trinker, E.W. Kaiser, W.O. Siegl, D.F. Cotton, J. Underwood, Hydrocarbon oxidation in the exhaust port and runner of a spark ignition engine, *Combustion and Flame* 99 (1994) 422–430.
- [83] J.H. Bromly, F.J. Barnes, S. Muris, X. You, B.S. Haynes, Kinetic and Thermodynamic Sensitivity Analysis of the NO-Sensitized Oxidation of Methane, *Combustion Science and Technology* 115 (1996) 259–296.
- [84] S. Gersen, A.V. Mokhov, J.H. Darneveil, H.B. Levinsky, P. Glarborg, Ignition-promoting effect of NO<sub>2</sub> on methane, ethane and methane/ethane mixtures in a rapid compression machine, *Proceedings of the Combustion Institute* 33 (2011) 433–440.

- [85] K. Otsuka, R. Takahashi, K. Amakawa, I. Yamanaka, Partial oxidation of light alkanes by NO<sub>x</sub> in the gas phase, *Catalysis Today* 45 (1998) 23–28.
- [86] C.L. Rasmussen, A.E. Rasmussen, P. Glarborg, Sensitizing effects of NO<sub>x</sub> on CH<sub>4</sub> oxidation at high pressure, *Combustion and Flame* 154 (2008) 529–545.
- [87] J.M. Zalc, W.H. Green, E. Iglesia, NO<sub>x</sub>-Mediated Homogeneous Pathways for the Synthesis of Formaldehyde from CH<sub>4</sub>–O<sub>2</sub> Mixtures, *Industrial & Engineering Chemistry Research* 45 (2006) 2677–2688.
- [88] A.A. Konnov, J.N. Zhu, J.H. Bromly, D.-k. Zhang, The effect of NO and NO<sub>2</sub> on the partial oxidation of methane: experiments and modeling, *Proceedings of the Combustion Institute* 30 (2005) 1093–1100.
- [89] Y.L. Chan, F.J. Barnes, J.H. Bromly, A.A. Konnov, D.K. Zhang, The differentiated effect of NO and NO<sub>2</sub> in promoting methane oxidation, *Proceedings of the Combustion Institute* 33 (2011) 441–447.
- [90] W.-T. Chan, S.M. Heck, H.O. Pritchard, Reaction of nitrogen dioxide with hydrocarbons and its influence on spontaneous ignition. A computational study, *Physical Chemistry Chemical Physics* 3 (2001) 56–62.
- [91] P. Glarborg, J.A. Miller, B. Ruscic, S.J. Klippenstein, Modeling nitrogen chemistry in combustion, *Progress in Energy and Combustion Science* 67 (2018) 31–68.
- [92] P. Glarborg, Hidden interactions—Trace species governing combustion and emissions, *Proceedings of the Combustion Institute* 31 (2007) 77–98.
- [93] C.L. Rasmussen, J. Hansen, P. Marshall, P. Glarborg, Experimental measurements and kinetic modeling of CO/H<sub>2</sub>/O<sub>2</sub>/NO<sub>x</sub> conversion at high pressure, *International Journal of Chemical Kinetics* 40 (2008) 454–480.
- [94] J. Smith, J. Phillips, A. Graham, R. Steele, A. Redondo, J. Coons, Homogeneous Chemistry in Lean-Burn Exhaust Mixtures, *The Journal of Physical Chemistry A* 101 (1997) 9157–9162.
- [95] J. Zhang, V. Burklé-Vitzthum, P.M. Marquaire, An Investigation on the Role of NO<sub>2</sub> in the Oxidation of Methane to Formaldehyde, *Combustion Science and Technology* 187 (2015) 1139–1156.
- [96] T. Faravelli, A. Frassoldati, E. Ranzi, 03/02037 Kinetic modeling of the interactions between NO and hydrocarbons in the oxidation of hydrocarbons at low temperatures, *Combustion and Flame* 44 (2003) 337.
- [97] K. Wegner, Mass Transfer: Heterogeneous and Homogeneous Heterogeneous and Homogeneous Chemical Reactions, Lecture Slides, Zürich, November 29th 2017.
- [98] T. Turányi, A.S. Tomlin, Analysis of kinetic reaction mechanisms, Springer, Heidelberg, 2014.

- [99] J. Warnatz, U. Maas, R.W. Dibble, *Combustion: Physical and chemical fundamentals, modeling and simulation, experiments, pollutant formation*, 4th ed., Springer, Berlin, New York, 2006.
- [100] J. Troe, Theory of Thermal Unimolecular Reactions in the Fall-off Range. I. Strong Collision Rate Constants, *Berichte der Bunsengesellschaft für physikalische Chemie* 87 (1983) 161–169.
- [101] F.A. Lindemann, S. Arrhenius, I. Langmuir, N.R. Dhar, J. Perrin, W.C. McC. Lewis, Discussion on “the radiation theory of chemical action”, *Transactions of the Faraday Society*. 17 (1922) 598–606.
- [102] F. Di Giacomo, A Short Account of RRKM Theory of Unimolecular Reactions and of Marcus Theory of Electron Transfer in a Historical Perspective, *Journal of Chemical Education* 92 (2015) 476–481.
- [103] R.G. Gilbert, K. Luther, J. Troe, Theory of Thermal Unimolecular Reactions in the Fall-off Range. II. Weak Collision Rate Constants, *Berichte der Bunsengesellschaft für physikalische Chemie* 87 (1983) 169–177.
- [104] O. Levenspiel, *Chemical reaction engineering*, 3rd ed., Wiley, Hoboken, NJ, 1999.
- [105] R.J. Kee, M.E. Coltrin, P. Glarborg, *Chemically reacting flow: Theory and practice*, Wiley-Interscience, Hoboken, NJ, 2003.
- [106] J. A. Dumesic, D. F. Rudd, L. M. Aparicio, J. E. Rekoske, and A. A. Treviño, *The microkinetics of heterogeneous catalysis*. ACS Professional Reference Book, *AIChE Journal*. 40, Washington, DC, 1993.
- [107] V.M. Janardhanan, O. Deutschmann, *Computational Fluid Dynamics of Catalytic Reactors*, in: O. Deutschmann (Ed.), *Modeling and Simulation of Heterogeneous Catalytic Reactions*, Wiley-VCH Verlag GmbH & Co. KGaA, Weinheim, Germany, 2011, pp. 251–282.
- [108] L. Maier, B. Schädel, K. Herrera Delgado, S. Tischer, O. Deutschmann, Steam Reforming of Methane Over Nickel: Development of a Multi-Step Surface Reaction Mechanism, *Topics in Catalysis* 54 (2011) 845–858.
- [109] K. Delgado, L. Maier, S. Tischer, A. Zellner, H. Stotz, O. Deutschmann, Surface Reaction Kinetics of Steam- and CO<sub>2</sub>-Reforming as Well as Oxidation of Methane over Nickel-Based Catalysts, *Catalysts* 5 (2015) 871–904.
- [110] B. Noll, *Numerische Strömungsmechanik: Grundlagen*, Springer, Berlin, Heidelberg, 1993.
- [111] S.V. Patankar, *Numerical heat transfer and fluid flow*, Hemisphere Publ. Co, New York, 1980.
- [112] H.K. Versteeg, W. Malalasekera, *An introduction to computational fluid dynamics: The finite volume method*, 2nd ed., Pearson/Prentice Hall, Harlow, 2010.
- [113] Michael Schäfer, *Computational Engineering — Introduction to Numerical Methods*, Springer-Verlag, Berlin/Heidelberg, 2006.

- [114] E.S. Oran, J.P. Boris, Numerical Simulation of Reactive Flow, Cambridge University Press, Cambridge, 2000.
- [115] S. Jayanti, Computational Fluid Dynamics for Engineers and Scientists, Springer Netherlands, Dordrecht, 2018.
- [116] A. Dixon, Modeling and Simulation of Heterogeneous Catalytic Processes, Elsevier Science, Burlington, 2014.
- [117] ANSYS Inc., ANSYS Fluent Theory Guid 15.0, 2013, <http://www.ansys.com>.
- [118] H. Karadeniz, Numerical modeling of stagnation flows over porous catalytic surfaces, KIT Scientific Publishing, Karlsruhe, 2016.
- [119] N. Mladenov, Modellierung von Autoabgaskatalysatoren. Karlsruhe, Univ., Diss., 2009, KIT Scientific Publ, Karlsruhe, 2010.
- [120] O. Deutschmann, S. Tischer, S. Kleditzsch, V. Janardhanan, C. Correa, D. Chatterjee, N. Mladenov, H. D. Minh, H. Karadeniz, M. Hettel, V. Menon, DETCHEM Software package, 2.7 ed., <https://www.detchem.com>, Karlsruhe 2018.
- [121] J.G. Blom, J.G. Verwer, R.A. Trompert, A comparison between direct and iterative methods to solve the linear systems arising from a time-dependent 2d groundwater flow model, *International Journal of Computational Fluid Dynamics* 1 (1993) 95–113.
- [122] F. Moukalled, L. Mangani, M. Darwish, The Finite Volume Method in Computational Fluid Dynamics, Springer International Publishing, Cham, 2016.
- [123] B. Torkashvand, P. Lott, D. Zengel, L. Maier, M. Hettel, J.-D. Grunwaldt, O. Deutschmann, Homogeneous Oxidation of Light Alkanes in the Exhaust of Turbocharged Lean-Burn Gas Engines, *Chemical Engineering Journal* (2018).
- [124] A.A. Konnov, Development and validation of a detailed reaction mechanism for the combustion modeling, *Eurasian Chemico-Technological Journal* 2 (2000) 257–264.
- [125] P. Glarborg, D. Kubel, P.G. Kristensen, J. Hansen, K. Dam-Johansen, Interactions of CO, NO<sub>x</sub> and H<sub>2</sub>O Under Post-Flame Conditions, *Combustion Science and Technology* 110-111 (1995) 461–485.
- [126] H. Hashemi, J.M. Christensen, S. Gersen, H. Levinsky, S.J. Klippenstein, P. Glarborg, High-pressure oxidation of methane, *Combustion and Flame* 172 (2016) 349–364.
- [127] A.A. Konnov, Implementation of the NCN pathway of prompt-NO formation in the detailed reaction mechanism, *Combustion and Flame* 156 (2009) 2093–2105.
- [128] J. Zhang, V. Burklé-Vitzthum, P.M. Marquaire, NO<sub>2</sub>-promoted oxidation of methane to formaldehyde at very short residence time – Part II, *Chemical Engineering Journal* 197 (2012) 123–134.

- [129] T. Takemoto, K. Tabata, Y. Teng, A. Nakayama, E. Suzuki, The effects of reaction pressures on the production of methanol through the selective oxidation of methane in  $\text{CH}_4\text{-O}_2\text{-NO}_x$  ( $x=1$  or  $2$ ), *Applied Catalysis A: General* 205 (2001) 51–59.
- [130] F. Richter, M. Hochlaf, P. Rosmus, F. Gatti, H.-D. Meyer, A study of the mode-selective trans-cis isomerization in HONO using ab initio methodology, *The Journal of chemical physics* 120 (2004) 1306–1317.
- [131] J.K. Lampert, M.S. Kazi, R.J. Farrauto, Palladium catalyst performance for methane emissions abatement from lean burn natural gas vehicles, *Applied Catalysis B: Environmental* 14 (1997) 211–223.
- [132] M.S. Wilburn, W.S. Epling, Sulfur deactivation and regeneration of mono- and bimetallic Pd-Pt methane oxidation catalysts, *Applied Catalysis B: Environmental* 206 (2017) 589–598.
- [133] B. Torkashvand, A. Gremminger, S. Valchera, M. Casapu, J.-D. Grunwaldt, O. Deutschmann, The Impact of Pre-Turbine Catalyst Placement on Methane Oxidation in Lean-Burn Gas Engines: An Experimental and Numerical Study, in: *SAE Technical Paper*, 2017-01-1019, 2017.
- [134] S. Eriksson, M. Boutonnet, S. Jaras, Catalytic combustion of methane in steam and carbon dioxide-diluted reaction mixtures, *Applied Catalysis A: General* 312 (2006) 95–101.
- [135] C. N. Satterfield, Heterogeneous catalysis in practice, McGraw-Hill Company, 1980.
- [136] G. Groppi, W. Ibashi, M. Valentini, P. Forzatti, High-temperature combustion of  $\text{CH}_4$  over  $\text{PdO}/\text{Al}_2\text{O}_3$  kinetic measurements in a structured annular reactor, *Chemical Engineering Science* 56 (2001) 831–839.
- [137] K. Persson, L.D. Pfefferle, W. Schwartz, A. Ersson, S.G. Järås, Stability of palladium-based catalysts during catalytic combustion of methane: The influence of water, *Applied Catalysis B: Environmental* 74 (2007) 242–250.
- [138] K.-i. Fujimoto, F.H. Ribeiro, M. Avalos-Borja, E. Iglesia, Structure and Reactivity of  $\text{PdO}_x/\text{ZrO}_2$  Catalysts for Methane Oxidation at Low Temperatures, *Journal of Catalysis* 179 (1998) 431–442.
- [139] A. Trincherro, A. Hellman, H. Grönbeck, Methane oxidation over Pd and Pt studied by DFT and kinetic modeling, *Surface Science* 616 (2013) 206–213.
- [140] Y. Xin, H. Wang, C.K. Law, Kinetics of catalytic oxidation of methane, ethane and propane over palladium oxide, *Combustion and Flame* 161 (2014) 1048–1054.
- [141] G. Bergeret, P. Gallezot, Particle size and dispersion measurements, in G. Ertl, H. Knözinger, F. Schüth, J. Weitkamp (Eds.), *Handbook of heterogeneous catalysis*, 2nd ed., Wiley-VCH, Weinheim, Chichester, 2008.

- [142] R.E. Hayes, S.T. Kolaczkowski, P.K.C. Li, S. Awdry, The palladium catalysed oxidation of methane: reaction kinetics and the effect of diffusion barriers, *Chemical Engineering Science* 56 (2001) 4815–4835.
- [143] S.T. Kolaczkowski, W.J. Thomas, J. Titiloye, D.J. Worth, Catalytic Combustion of Methane in a Monolith Reactor: Heat and Mass Transfer Under Laminar Flow and Pseudo-Steady-State Reaction Conditions, *Combustion Science and Technology* 118 (1996) 79–100.
- [144] B. Liu, R.E. Hayes, M.D. Checkel, M. Zheng, E. Mirosh, Reversing flow catalytic converter for a natural gas/diesel dual fuel engine, *Chemical Engineering Science* 56 (2001) 2641–2658.
- [145] P. Hurtado, S. Ordonez, H. Sastre, F. Diez, Combustion of methane over palladium catalyst in the presence of inorganic compounds: inhibition and deactivation phenomena, *Applied Catalysis B: Environmental* 47 (2004) 85–93.
- [146] K. Narui, H. Yata, K. Furuta, A. Nishida, Y. Kohtoku, T. Matsuzaki, Effects of addition of Pt to PdO/Al<sub>2</sub>O<sub>3</sub> catalyst on catalytic activity for methane combustion and TEM observations of supported particles, *Applied Catalysis A: General* 179 (1999) 165–173.
- [147] D.H. Coller, B.C. Vicente, S.L. Scott, Rapid extraction of quantitative kinetic information from variable-temperature reaction profiles, *Chemical Engineering Journal* 303 (2016) 182–193.
- [148] B. Torkashvand, L. Maier, P. Lott, T. Schedlbauer, J.-D. Grunwaldt, O. Deutschmann, Formaldehyde Oxidation Over Platinum: On the Kinetics Relevant to Exhaust Conditions of Lean-Burn Natural Gas Engines, *Topics in Catalysis* 114 (2018) 1347.
- [149] J. Peng, S. Wang, Performance and characterization of supported metal catalysts for complete oxidation of formaldehyde at low temperatures, *Applied Catalysis B: Environmental* 73 (2007) 282–291.
- [150] T. Schedlbauer, A. Gremminger, M. Casapu, O. Deutschmann, J.-D. Grunwaldt, Impact of the Gas Mixture and Aging Conditions on Formaldehyde Conversion over a Series of Commercial Pt-Based Catalysts, *SAE Technical Papers 2018-01-5021* (2018).
- [151] M. Hettel, C. Diehm, B. Torkashvand, O. Deutschmann, Critical evaluation of in situ probe techniques for catalytic honeycomb monoliths, *Catalysis Today* 216 (2013) 2–10.
- [152] C. Diehm, O. Deutschmann, Hydrogen production by catalytic partial oxidation of methane over staged Pd/Rh coated monoliths: Spatially resolved concentration and temperature profiles, *International Journal of Hydrogen Energy* 39 (2014) 17998–18004.
- [153] O. Deutschmann, R. Schmidt, F. Behrendt, J. Warnat, Numerical modeling of catalytic ignition, *Symposium (International) on Combustion* 26 (1996) 1747–1754.
- [154] A.B. Mhadeshwar, D.G. Vlachos, A Catalytic Reaction Mechanism for Methane Partial Oxidation at Short Contact Times, Reforming, and Combustion, and for Oxygenate

- Decomposition and Oxidation on Platinum, *Industrial & Engineering Chemistry Research* 46 (2007) 5310–5324.
- [155] H. Sharma, A. Mhadeshwar, A detailed microkinetic model for diesel engine emissions oxidation on platinum based diesel oxidation catalysts (DOC), *Applied Catalysis B: Environmental* 127 (2012) 190–204.
- [156] G.E. Gdowski, J.A. Fair, R.J. Madix, Reactive scattering of small molecules from platinum crystal surfaces: D<sub>2</sub>CO, CH<sub>3</sub>OH, HCOOH, and the nonanomalous kinetics of hydrogen atom recombination, *Surface Science Letters* 127 (1983) A177.
- [157] T.L. Silbaugh, E.M. Karp, C.T. Campbell, Energetics of methanol and formic acid oxidation on Pt(111): Mechanistic insights from adsorption calorimetry, *Surface Science* 650 (2016) 140–143.
- [158] A.B. Mhadeshwar, H. Wang, D.G. Vlachos, Thermodynamic Consistency in Microkinetic Development of Surface Reaction Mechanisms, *The Journal of Physical Chemistry B* 107 (2003) 12721–12733.
- [159] R.D. Cortright, J.A. Dumesic, Kinetics of heterogeneous catalytic reactions: Analysis of reaction schemes, *Advances in Catalysis, Academic Press* (2001) 161–264.
- [160] E. Shustorovich, H. Sellers, The UBI-QEP method, *Surface Science Reports* 31 (1998) 1–119.
- [161] Evgeny Shustorovich, The Bond-Order Conservation Approach to Chemisorption and Heterogeneous Catalysis, *Advances in Catalysis* 37 (1990) 101–163.
- [162] F. Eisert, A.P. Elg, A. Rosn, Adsorption of oxygen and hydrogen on Pt(111) studied with second-harmonic generation, *Applied Physics A: Materials Science & Processing* 60 (1995) 209–215.
- [163] T.A. Germer, W. Ho, Direct characterization of the hydroxyl intermediate during reduction of oxygen on Pt(111) by time-resolved electron energy loss spectroscopy, *Chemical Physics Letters* 163 (1989) 449–454.
- [164] S. Völkening, K. Bedürftig, K. Jacobi, J. Wintterlin, G. Ertl, Dual-Path Mechanism for Catalytic Oxidation of Hydrogen on Platinum Surfaces, *Physical Review Letters* 83 (1999) 2672–2675.
- [165] Y.K. Park, P. Aghalayam, D.G. Vlachos, A Generalized Approach for Predicting Coverage-Dependent Reaction Parameters of Complex Surface Reactions: Application to H<sub>2</sub> Oxidation over Platinum, *The Journal of Physical Chemistry A* 103 (1999) 8101–8107.
- [166] V.P. Zhdanov, B. Kasemo, Kinetic phase transitions in simple reactions on solid surfaces, *Surface Science Reports* 20 (1994) 113–189.
- [167] K. Christmann, G. Ertl, T. Pignet, Adsorption of hydrogen on a Pt(111) surface, *Surface Science* 54 (1976) 365–392.

- [168] E.G. Seebauer, A.C.F. Kong, L.D. Schmidt, Adsorption and desorption of NO, CO and H<sub>2</sub> on Pt(111): Laser-induced thermal desorption studies, *Surface Science* 176 (1986) 134–156.
- [169] M. Rinnemo, O. Deutschmann, F. Behrendt, B. Kasemo, Experimental and numerical investigation of the catalytic ignition of mixtures of hydrogen and oxygen on platinum, *Combustion and Flame* 111 (1997) 312–326.
- [170] O. Deutschmann, Schmidt R., Berendt F., Interaction of transport and chemical kinetics in catalytic combustion of H<sub>2</sub>/O<sub>2</sub> mixtures on Pt, *Transport Phenomena in Combustion, Proceedings of the International Symposium on Transport Phenomena in Combustion 8th 1996* 166–175.
- [171] C.T. Campbell, G. Ertl, H. Kuipers, J. Segner, A Molecular Beam Investigation of the Interactions of CO with a Pt(111) Surface, *Surface Science* 107 (1981) 207–219.
- [172] L. Olsson, B. Westerberg, H. Persson, E. Fridell, M. Skoglundh, B. Andersson, A Kinetic Study of Oxygen Adsorption/Desorption and NO Oxidation over Pt/Al<sub>2</sub>O<sub>3</sub> Catalysts, *The Journal of Physical Chemistry B* 103 (1999) 10433–10439.
- [173] D.A. Hickman, L.D. Schmidt, Steps in CH<sub>4</sub> oxidation on Pt and Rh surfaces: High-temperature reactor simulations, *AIChE Journal* 39 (1993) 1164–1177.
- [174] G.S. Zafiris, R.J. Gorte, CO Oxidation on Pt/ $\alpha$ -Al<sub>2</sub>O<sub>3</sub>(0001): Evidence for Structure Sensitivity, *Journal of Catalysis* 140 (1993) 418–423.
- [175] M.M. Schubert, M.J. Kahlich, H.A. Gasteiger, R.J. Behm, Correlation between CO surface coverage and selectivity/kinetics for the preferential CO oxidation over Pt/ $\gamma$ -Al<sub>2</sub>O<sub>3</sub> and Au/ $\alpha$ -Fe<sub>2</sub>O<sub>3</sub>: an in-situ DRIFTS study, *Journal of Power Sources* 84 (1999) 175–182.
- [176] D. Gavril, G. Karaiskakis, Study of the sorption of carbon monoxide, oxygen and carbon dioxide on platinum–rhodium alloy catalysts by a new gas chromatographic methodology, *Journal of Chromatography A* 845 (1999) 67–83.
- [177] D.K. Zerkle, M.D. Allendorf, M. Wolf, O. Deutschmann, Understanding Homogeneous and Heterogeneous Contributions to the Platinum-Catalyzed Partial Oxidation of Ethane in a Short-Contact-Time Reactor, *Journal of Catalysis* 196 (2000) 18–39.
- [178] G.B. Fisher, J.L. Gland, The interaction of water with the Pt(111) surface, *Surface Science* 94 (1980) 446–455.
- [179] O. Deutschmann, L.I. Maier, U. Riedel, A.H. Stroemman, R.W. Dibble, Hydrogen assisted catalytic combustion of methane on platinum, *Catalysis Today* 59 (2000) 141–150.
- [180] S. Ljungström, B. Kasemo, A. Rosen, T. Wahnström, E. Fridell, An experimental study of the kinetics of OH and H<sub>2</sub>O formation on Pt in the H<sub>2</sub> + O<sub>2</sub> reaction, *Surface Science* 216 (1989) 63–92.

- [181] B. Hellsing, B. Kasemo, S. Ljungström, A. Rosén, T. Wahnström, Kinetic model and experimental results for H<sub>2</sub>O and OH production rates on Pt, *Surface Science* 189-190 (1987) 851–860.
- [182] B. Poelsema, G. Mechttersheimer, G. Comsa, The interaction of hydrogen with platinum(s)-9(111) × (111) studied with helium beam diffraction, *Surface Science* 111 (1981) 519–544.
- [183] D.H. Parker, M.E. Bartram, B.E. Koel, Study of high coverages of atomic oxygen on the Pt(111) surface, *Surface Science* 217 (1989) 489–510.
- [184] A. Holmgren, D. Duprez, B. Andersson, A Model of Oxygen Transport in Pt/Ceria Catalysts from Isotope Exchange, *Journal of Catalysis* 182 (1999) 441–448.
- [185] M. Ehsasi, S. Rezaie-Serej, J.H. Block, K. Christmann, Reaction rate oscillation of CO oxidation on Pt(210), *The Journal of chemical physics* 92 (1990) 7596–7609.
- [186] R.W. McCabe, L.D. Schmidt, binding states of CO and H<sub>2</sub> on clean and oxidized (111)Pt, *Surface Science* 65 (1977) 189–209.
- [187] A.V. Zeigarnik, C. Callaghan, R. Datta, I. Fishtik, E. Shustorovich, Prediction of Comparative Catalytic Activity in the Series of Single Crystalline Surfaces in a Water-Gas Shift Reaction, *Kinetics and Catalysis* 46 (2005) 509–515.
- [188] R.H. Nibbelke, M.A.J. Campman, J.H.B.J. Hoebink, G.B. Marin, Kinetic Study of the CO Oxidation over Pt/γ-Al<sub>2</sub>O<sub>3</sub> and Pt/Rh/CeO<sub>2</sub>/γ-Al<sub>2</sub>O<sub>3</sub> in the Presence of H<sub>2</sub>O and CO<sub>2</sub>, *Journal of Catalysis* 171 (1997) 358–373.
- [189] N. PACIA, A. Cassuto, A. Pentenero, B. Weber, Molecular beam study of the mechanism of carbon monoxide oxidation on platinum and isolation of elementary steps, *Journal of Catalysis* 41 (1976) 455–465.
- [190] A.B. Anton, D.C. Cadogan, Kinetics of water formation on Pt(111), *Journal of Vacuum Science & Technology A: Vacuum, Surfaces, and Films* 9 (1991) 1890–1897.
- [191] W.R. Williams, C.M. Marks, L.D. Schmidt, Steps in the Reaction H<sub>2</sub> + O<sub>2</sub> - Reversible - Arrow - H<sub>2</sub>O on Pt - OH Desorption at High-Temperatures, *Journal of Physical Chemistry* 96 (1992) 5922–5931.
- [192] B. Torkashvand, L. Maier, M. Hettel, T. Schedlbauer, J.-D. Grunwaldt, O. Deutschmann, On the challenges and constraints of ultra-low emission limits: Formaldehyde oxidation in catalytic sinusoidal-shaped channels, *Chemical Engineering Science* 195 (2019) 841–850.
- [193] ANSYS® Academic Research: 18.1, ANSYS, Inc., 2017.
- [194] J. Koop, O. Deutschmann, Detailed surface reaction mechanism for Pt-catalyzed abatement of automotive exhaust gases, *Applied Catalysis B: Environmental* 91 (2009) 47–58.

- [195] O. Deutschmann, R. Schwiedernoch, L.I. Maier, D. Chatterjee, Natural Gas Conversion in Monolithic Catalysts: Interaction of Chemical Reactions and Transport Phenomena, *Natural Gas Conversion VI, Studies in Surface Science and Catalysis 136*, E. Iglesia, J.J. Spivey, T.H. 2001.

## List of Symbols

Symbol	Description	Unit
$A_{\text{cat}}$	catalytic surface area	$\text{m}^2$
$A_{\text{geo}}$	geometrical surface area	$\text{m}^2$
$A_k$	pre-exponential factor	cm, mol, s
$A_k^{\text{ads}}$	pre-exponential factor for adsorptions reactions	cm, mol, s
$a'_{ik}$	Reaction order with respect to reactants	-
$a''_{ik}$	Reaction order with respect to products	-
$a_i^{\text{eq}}$	equilibrium activities	-
$c_i$	concentration of species $i$	$\text{mol.m}^{-3}$
$c_p$	Specific enthalpy of the mixture	$\text{J.kg}^{-1}$
$D_i$	diffusion coefficient of species $i$	$\text{m}^2.\text{s}^{-1}$
$D_{ij}$	multi-component diffusion coefficient of species $i$	$\text{m}^2.\text{s}^{-1}$
$D_{i,T}$	thermal diffusion coefficient of $i$	$\text{m}^2.\text{s}^{-1}$
$D_{i,\text{eff}}$	effective diffusion coefficient	$\text{m}^2.\text{s}^{-1}$
$D_{i,\text{Knud}}$	Knudsen diffusion coefficient	$\text{m}^2.\text{s}^{-1}$
$D_{i,M}$	averaged diffusion coefficient in the mixture	$\text{m}^2.\text{s}^{-1}$
$D_{\text{pt}}$	Dispersion of platinum	-
$E_{ak}$	activation energy	$\text{kJ.mol}^{-1}$
$F_{\text{cat}/\text{geo}}$	surface scaling factor	-
$F_{\text{cent}}$	Broadening factor of center of the fall-off range	-
$\Delta_R \overline{G}^0$	Gibbs free energy change at standard conditions	$\text{kJ.mol}^{-1}$
$G_i$	Gibb's free energy of species $i$	$\text{kJ.mol}^{-1}$
$g_i$	gravitational acceleration	$\text{m.s}^{-2}$
$h_i$	specific enthalpy of species $i$	$\text{kJ.mol}^{-1}$

$J_i$	diffusive flux of species $i$	$\text{mol.m}^{-2}.\text{s}^{-1}$
$K_c$	Equilibrium constant	-
$k_{fk}$	reaction rate coefficient of forward reaction	
$k_{rk}$	reaction rate coefficient of reverse reaction	
$k_B$	Boltzmann constant	$1.381 \times 10^{-23} \text{ J.K}^{-1}$
$M_i$	molecular weight of species $i$	$\text{kg.mol}^{-1}$
$M$	molecular weight of the mixture	$\text{kg.mol}^{-1}$
$m_{ij}$	Reduced mass	kg
$m_{yi}$	collision efficiency of species $i$	-
$N_A$	Avogadro's number	$6.02 \times 10^{23} \text{ mol}^{-1}$
$N_g$	number of gas-phase species	-
$N_s$	number of surface species	-
$N_b$	number of bulk species	-
$n_i$	number of moles of species $i$	mol
$n_i$	Component of the unit normal vector on the surface	
$p$	pressure	Pa
$p_r$	Reduced pressure	Pa
$R$	gas constant	$8.314 \text{ J.}(\text{mol.K})^{-1}$
$r$	radius	m
$S_\phi$	Source term	
$\dot{s}_i$	surface reaction rate of species $i$	$\text{mol.m}^{-2}.\text{s}^{-1}$
$s_i^0$	Initial sticking coefficient	-
$T$	temperature	K
$T_{ij}^*$	Reduced Temperature	K
$t$	time	s
$u$	axial velocity	$\text{m.s}^{-1}$

$V$	Volume	$m^3$
$v$	radial velocity	$m.s^{-1}$
$v'_{ik}$	stoichiometric coefficients of reactants	-
$v''_{ik}$	Stoichiometric coefficient of products	-
$X_i$	conversion of species $i$	
$x_i$	mole fraction of species $i$	-
$Y_i$	mass fraction of species $i$	$m.s^{-1}$

### Greek Symbols

$\beta_k$	temperature exponent	-
$\varepsilon_i$	coverage dependent activation energy	$kJ.mol^{-1}$
$\varepsilon$	Porosity of the washcoat layer	-
$\Gamma$	surface site density	$mol.m^2$
$\Gamma_\phi$	Diffusion coefficient of variable $\phi$	$m^2.s^{-1}$
$\phi$	Flow variable	
$\varphi_i$	Thiele module	-
$\sigma_{AB}$	Collisional cross-section	$m^2$
$\theta_{ij}$	Reduced diameter	$m$
$\sigma_i$	Number of catalytic sites occupied by one particle	-
$\tau_{ij}$	stress tensor	$N.m^{-2}$
$\theta_i$	surface coverage of species $i$	-
$\lambda$	thermal conductivity	$W.(m.K)^{-1}$
$\gamma$	ratio of the catalytic surface area to geometrical washcoat volume	-
$\Omega_{ij}$	Reduced collision integral	
$\rho$	density	$Kg.m^{-3}$
$\mu$	viscosity	$kg.(m.s)^{-1}$
$\eta_i$	effectiveness factor	-

$\tau$	Tortuosity of washcoat layer	-
$\dot{\omega}_i$	Molar reaction rate of gas-phase reaction of species $i$	$\text{mol.m}^{-3}.\text{s}^{-1}$

---

## List of Abbreviations

Abbreviation	Description
CEM	Controlled Evaporator Mixer
CI	Compression Ignited
CFD	Computational Fluid Dynamics
cp <sub>cm</sub>	Cell Per square centimeter
cp <sub>si</sub>	Cell Per square inch
CSTR	Continuous stirred tank reactor
FDM	Finite Difference Method
FEM	Finite Element Method
FT-IR	Fourier Transform - InfraRed
FVM	Finite Volume Method
GHSV	Gas Hourly Space Velocity
GM	Gas Mixture
HC	HydroCarbon
NG	Natural Gas
NMHC	Non-Methane HydroCarbon
NO <sub>x</sub>	Nitrogen Oxides
PM	Particulate Matter
RTD	Residence Time Distribution
SI	Spark Ignited
slpm	Standard Liter Per Minute
TDC	Top Dead Center
UHC	Unburnt HydroCarbon
UBI-QEP	Unity Bond Index – Quadratic Exponential Potential



# Appendix

## A) Estimation of temperature profile

Temperature profile inside the pressurized reactor, used for the modeling study in Chapter3.

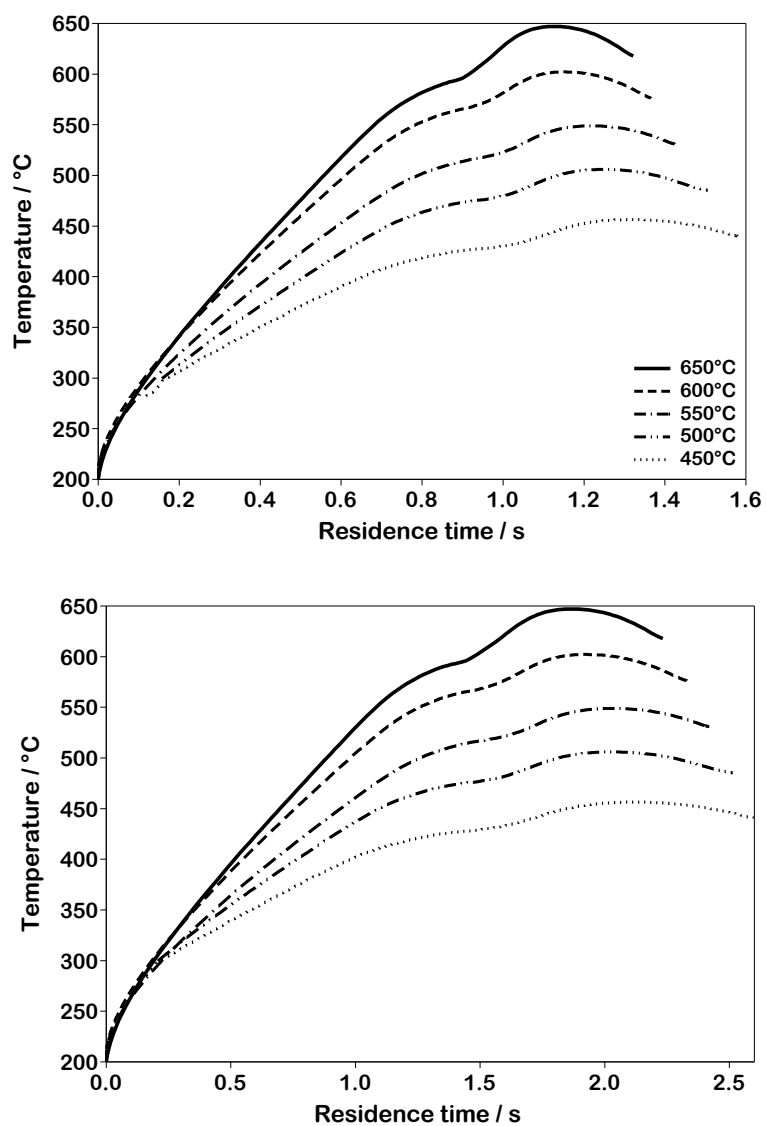


**Figure 1:** Temperature profile vs. residence time for the adjusted reactor temperature at top: 3 bar and bottom: 5 bar.

## B) Evaluation of used reactor model

Comparison of predicted concentration profiles modeled with DETCHEM<sup>BATCH</sup> and DETCHEM<sup>CSTR</sup> code at 5 bar. The present results correspond to the results and discussion of section 3.5.

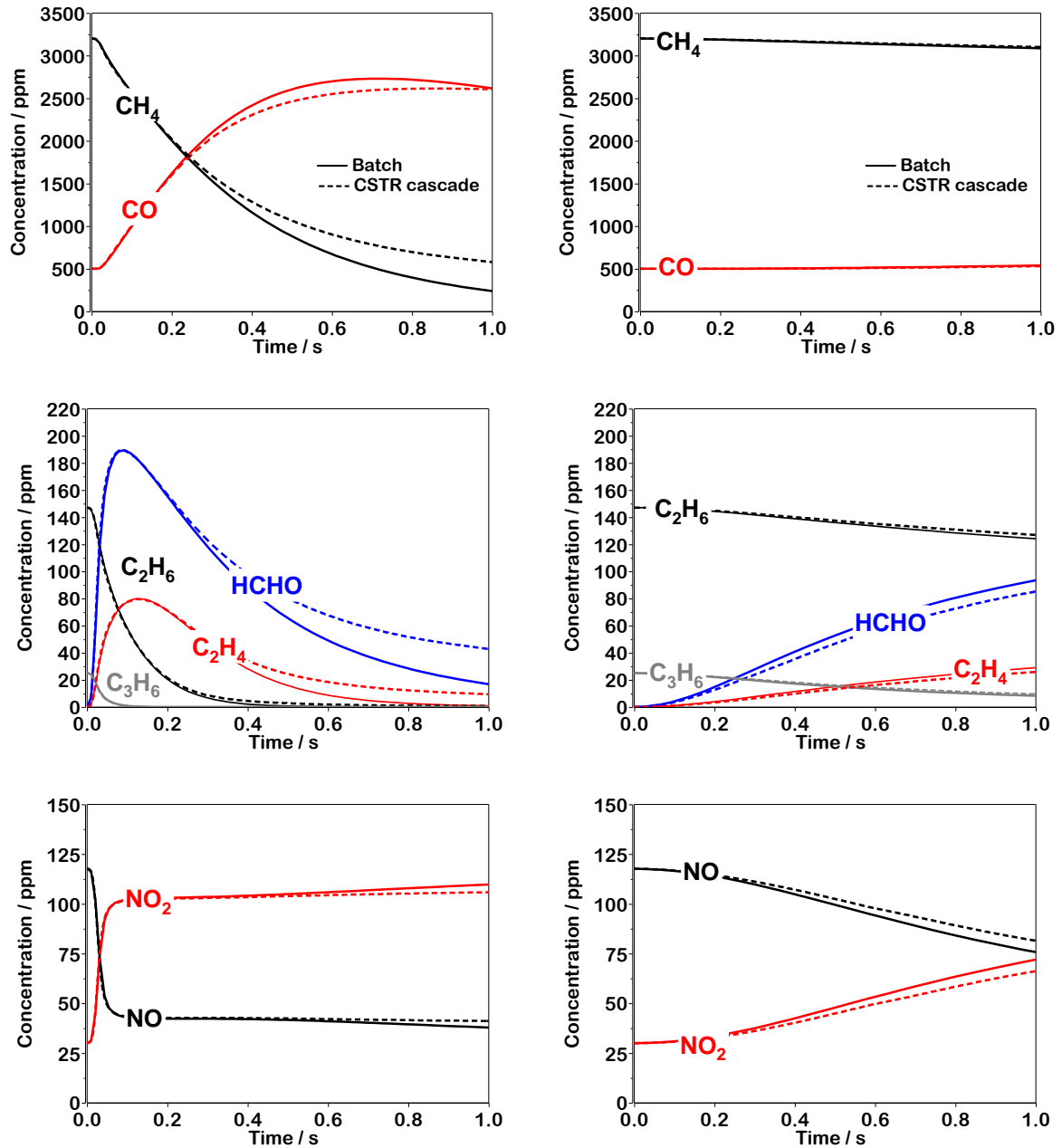


**Figure 2:** Concentration profile of gas components vs. reaction time simulated with the mechanism of *Konnov* with a batch (solid lines) and a CSTR-cascade (dashed lines) model at 5 bar. Left: 650 °C. Right: 550°C. Inlet gas composition GM1: 3200 ppm CH<sub>4</sub>, 500 ppm CO, 150 ppm C<sub>2</sub>H<sub>6</sub>, 25 ppm C<sub>3</sub>H<sub>6</sub>, 120 ppm NO, 30 ppm NO<sub>2</sub>, 10 vol. % O<sub>2</sub> and 12 vol. % H<sub>2</sub>O in N<sub>2</sub>.



## Acknowledgments

First and foremost, I want to thank Prof. Dr. Olaf Deutschmann for accepting me as a Ph.D. student and for giving me the opportunity to work under his supervision in his research group. I am sincerely grateful for continuous intellectual and financial support during my dissertation and the support on industrial and academic collaborations. Moreover, I very much appreciated the freedom I was given to shape my thesis and realize my ideas. I thank Prof. Dr. Achim Dittler for agreeing to be the second referee of this thesis and the rest of the examiners' committee for their time and consideration.

I owe a sincere and earnest thankfulness to Dr. Matthias Hettel, for always being there to help me with scientific problems, for the many great discussions and his continuous guidance and support regarding CFD calculations. I would like to thank him for his friendship and moral support. Furthermore, I would like to express my gratitude to Dr. Lubow Maier for fruitful discussions on kinetics and mechanism development, her encouragement, and her continuous support. I would also like to thank Martin Spoo for his great supports with IT issues. Without his help, the performance of the CFD calculations would not be possible.

I owe a lot of thanks to my friends and colleagues, Dr. Gazal Tofighi, Dr. Hamzeh Alavirad, Dr. Sofia Angeli, Yvonne Dedecek, Henning Stotz, and Patrick Lott for proof reading of this thesis. I also thank Hendrik Goßler for the pleasant time we had together and the daily helps and discussions on scientific/non-scientific topics in office. Many thanks to my colleagues from ITCP, especially the members of the Karlsruhe exhaust-gas center, for the excellent collaboration and the pleasant working environment.